RECORD OF CRUSTAL THICKENING AND SYNCONVERGENT EXTENSION FROM THE DAJIAMANG TSO RIFT, SOUTHERN TIBET

by

William Brian Burke

A thesis submitted in partial fulfillment
of the requirements for the degree

of

Master of Science

in

Earth Sciences - Geology

MONTANA STATE UNIVERSITY
Bozeman, Montana

April 2021

"It's a dangerous business…going out your door.
You step onto the road, and if you don't keep your feet,
There's no knowing where you might be swept off to."

\- Gandalf
The Lord of the Rings

TABLE OF CONTENTS

TABLE OF CONTENTS

LIST OF FIGURES

Figure Page

CHAPTER ONE

INTRODUCTION TO THESIS

Normal faults systems (rifts) are geologic structures that form in response to extensional stresses acting upon Earth's crust. These structures include a downthrown hanging wall and an adjacent exhumed footwall; the two blocks separated by a dominant fault surface or zone along which movement occurs. As the crust accommodates extension via normal faulting, rocks contained in the footwalls of these rift systems are exhumed to the surface from depth, while hanging wall rocks form rift valleys, often buried by sediment eroded and transported from adjacent ridge-forming footwalls. When observed in the field or from satellite imagery, the orientations of these rift systems provide indication of the stress field acting upon the upper crust, with normal fault traces trending orthogonal to the primary extension direction.

Despite the contractional nature of the Himalayan-Tibetan orogen (e.g., Allegre et al., 1984; Yin and Harrison, 2000), north-trending rift systems throughout the Lhasa Terrane of southern Tibet indicate east-west (orogen-parallel) extension. Previous studies of these rift systems have led to several leading dynamic models to explain the onset of east-west extension despite continued convergence between India and Asia. These include (1) lateral collapse of the plateau as a result of gravitational potential energy outweighing collisional forces (e.g., Molnar & Tapponnier (1975, 1978); Dewey, 1988), (2) convective removal of the lower layer of Tibet's over-thickened lithosphere (England & Houseman, 1989), and (3) coeval thickening and collapse driven by underthrusting Indian lithosphere (e.g., Kind et al., 2002; Kapp and Guynn, 2004; Styron et al., 2015).

The manuscript presented in this thesis tests these competing models for synconvergent extension in Tibet by (1) quantifying the timing of extension onset and (2) using geochemical proxies to evaluate the tectonic configuration of the southern Eurasian margin preceding and throughout the proposed period of India-Asia collision. For our test case, we focus on the Dajiamang Tso Rift, a north-trending normal fault system located just north of the India-Asia suture zone. This rift is of particular interest because of its location within the high topography (and high crustal thickness) of the Gangdese range (e.g., Zhao et al., 2001; Kind et al., 2002; Xu et al., 2015), as well as its proximity to other prominent structures acting upon the Himalayan-Tibetan orogen (e.g., the Great Counter Thrust) (Heim and Gassner, 1939; Yin et al., 1999; Murphy and Yin, 2003).

This research presents new geologic mapping and igneous zircon U-Pb geochronology data to constrain rock units and structures present in the Dajiamang Tso Rift field area. We also apply zircon-He thermochronology to samples collected from rift footwalls to constrain the timing of extension initiation. Finally, we apply Lu-Hf isotopic analysis to evaluate crustal contamination processes, and recently updated quantitative crustal thickness equations to calculate time-sensitive crustal thickness estimates for the Dajiamang Tso Rift region of the Gangdese Range (Sundell et al., 2021). These techniques allow us to evaluate existing models for the evolution of the Himalayan-Tibetan orogen through a geochronological, thermochronological, and geochemical lens. By comparing our results to previously published data throughout Tibet, we are able to better understand active deformation in the world’s archetypal contractional orogenic belt and test techniques that can be applied to similar tectonic environments around the world.

Literature Cited

Allegre, C. o., Courtillot, V., Tapponnier, P., Hirn, A., Mattauer, M., Coulon, C., . . . Marcoux, J. (1984). Structure and evolution of the Himalaya–Tibet orogenic belt. *Nature, 307*(5946), 17.

Dewey, J. (1988). Extensional collapse of orogens. *Tectonics, 7*(6), 1123-1139.

England, P., & Houseman, G. (1989). Extension during continental convergence, with application to the Tibetan Plateau. *Journal of Geophysical Research: Solid Earth, 94*(B12), 17561-17579.

Kapp, P., & Guynn, J. H. (2004). Indian punch rifts Tibet. *Geology, 32*(11), 993-996.

Kind, R., Yuan, X., Saul, J., Nelson, D., Sobolev, S., Mechie, J., . . . Achauer, U. (2002). Seismic images of crust and upper mantle beneath Tibet: evidence for Eurasian plate subduction. *science, 298*(5596), 1219-1221.

Molnar, P., & Tapponnier, P. (1975). Cenozoic tectonics of Asia: effects of a continental collision. *science, 189*(4201), 419-426.

Molnar, P., & Tapponnier, P. (1978). Active tectonics of Tibet. *Journal of Geophysical Research: Solid Earth, 83*(B11), 5361-5375.

Murphy, M., & Yin, A. (2003). Structural evolution and sequence of thrusting in the Tethyan fold-thrust belt and Indus-Yalu suture zone, southwest Tibet. *Geological Society of America Bulletin, 115*(1), 21-34.

Heim, A., & Gansser, A. (1975). *Central Himalaya: Geological observations of the Swiss expedition, 1936* (Vol. 73): Hindustan Publishing Corporation (India).

Styron, R., Taylor, M., & Sundell, K. (2015). Accelerated extension of Tibet linked to the northward underthrusting of Indian crust. *Nature Geoscience, 8*(2), 131.

Sundell, K., Laskowski, A. K., Kapp, P. A., & Ducea, M. N. (2021). Jurassic to Neogene quantitative crustal thickness estimates in southern Tibet from recalibrated Sr/Y and La/Yb trace element geochemical proxies. *GSA today*.

Xu, Q., Zhao, J., Yuan, X., Liu, H., & Pei, S. (2015). Mapping crustal structure beneath southern Tibet: Seismic evidence for continental crustal underthrusting. *Gondwana Research, 27*(4), 1487-1493.

Yin, A., Harrison, T. M., Murphy, M., Grove, M., Nie, S., Ryerson, F., . . . Zeng Le, C. (1999). Tertiary deformation history of southeastern and southwestern Tibet during the Indo-Asian collision. *Geological Society of America Bulletin, 111*(11), 1644-1664.

Yin, A., & Harrison, T. M. (2000). Geologic evolution of the Himalayan-Tibetan orogen. *Annual review of earth and planetary sciences, 28*(1), 211-280.

Zhao, W., Mechie, J., Brown, L., Guo, J., Haines, S., Hearn, T., . . . Nelson, K. (2001). Crustal structure of central Tibet as derived from project INDEPTH wide-angle seismic data. *Geophysical Journal International, 145*(2), 486-498.

CHAPTER TWO

RECORD OF CRUSTAL THICKENING AND SYNCONVERGENT EXTENSION FROM THE DAJIAMANG TSO RIFT, SOUTHERN TIBET

Contributions of Authors and Co-Authors

Manuscript in Chapter 2

Author: William B. Burke
Contributions: Conceptualization, Methodology, Formal Analysis, Writing – Original Draft Preparation, Writing – Reviewing and Editing, Visualization, Project Administration.

Co-Author: Andrew K. Laskowski
Contributions: Conceptualization, Methodology, Formal Analysis, Investigation, Writing – Reviewing and Editing, Supervision, Project Administration, Funding Acquisition.

Co-Author: Devon A. Orme
Contributions: Investigation, Writing – Reviewing and Editing.

Co-Author: Kurt E. Sundell
Contributions: Methodology, Investigation, Writing – Reviewing and Editing.

Co-Author: Michael H. Taylor
Contributions: Conceptualization, Writing – Reviewing and Editing.

Co-Author: Xudong Guo
Contributions: Investigation.

Co-Author: Lin Ding
Contributions: Investigation.

Manuscript Information Page

William B. Burke[a], Andrew K. Laskowski[a], Devon A. Orme[a], Kurt E. Sundell[b], Michael H. Taylor[c], Xudong Guo[d], Lin Ding[d]

[a] Department of Earth Sciences, Montana State University, Bozeman, MT, United States
[b] Department of Geosciences, University of Arizona, Tuscon, AZ, United States
[c] Department of Geology, University of Kansas, Lawrence, KS, United States
[d] Institute of Tibetan Plateau Research, Chinese Academy of Sciences, Beijing, China

MDPI Geosciences – Special Volumes

Status of Manuscript:
___ Prepared for submission to a peer-reviewed journal
_X_ Officially submitted to a peer-reviewed journal
___ Accepted by a peer-reviewed journal
___ Published in a peer-reviewed journal

Abstract

Gangdese Rifts such as the Dajiamang Tso Rift of south-central Tibet provide an opportunity to study the dynamics of synconvergent extension in contractional orogenic belts. In this study, we present quantitative crustal thickness estimates calculated from Trace/Rare Earth Element zircon data paired with U-Pb geochronology and zircon-He thermochronology. These data constrain the timing and rates of exhumation in the Dajiamang Tso Rift and provide a basis for evaluating dynamic models of synconvergent extension. Our results also provide a semi-continuous record of Mid-Cretaceous to Miocene evolution of the Himalayan-Tibetan orogenic belt along the India-Asia suture zone. We report igneous zircon U-Pb ages of ~103 Ma and 70-42 Ma for samples collected from the Xigaze forearc basin and Gangdese Batholith/Linzizong Formation, respectively. Zircon-He cooling ages of forearc rocks in the hanging wall of the Great Counter Thrust are ~28 Ma while Gangdese arc samples in the footwalls of the Dajiamang Tso Rift are 16-8 Ma. These data reveal the approximate timing of the switch from contraction to extension along the India-Asia suture zone (minimum 16 Ma). Crustal-thickness trends from zircon geochemistry reveal possible crustal thinning (to ~40 km) immediately prior to India-Asia collision onset (100-70 Ma). Following collision onset, crustal thickness increases to 50 km by 40 Ma with continued thickening until the early Miocene supported by regional data from the Tibetan Magmatism Database. Modern crustal thickness estimates based on geophysical observations show no evidence for crustal thinning following the onset of E-W extension (~16 Ma), suggesting that modern crustal thickness is likely facilitated by underthrusting Indian lithosphere balanced by upper plate extension.

Introduction

Normal fault systems accommodating orogen-parallel extension provide an opportunity to study the dynamics of synconvergent extension in contractional orogenic belts. In the Lhasa terrane of southern Tibet, we calculate quantitative crustal thickness estimates calculated from Trace/Rare Earth Element geochemistry, U-Pb geochronology, and zircon-He (ZHe) thermochronology to examine the relationship between crustal thickness trends and the timing/dynamics of E-W extension in one of the worlds archetypal collisional orogens. Assembled by the sequential accretion of island arc terranes and continental fragments since the Paleozoic, the Tibetan Plateau is the highest and most expansive orogenic plateau on Earth with crustal thickness estimates ranging from ~65 km in the north (Zhao et al., 2001; Kind et al., 2002) to ~85 km beneath the Indus-Yarlung Suture (Xu et al., 2015). While contractional deformation has led to significant shortening and crustal thickening throughout the region (Allegre et al., 1984; Yin and Harrison, 2000; Kapp and DeCelles, 2019; Zuza et al., 2020), the southern and central portions of the Tibetan Plateau have experienced east-west extension since the early Neogene, expressed at the surface as a network of approximately north-striking normal faults and associated strike slip faults (Armijo et al., 1986; 1989; Taylor et al., 2003). A fundamental question in understanding this orogen is how crustal thickness has changed through time and how these changes relate to ongoing east-west extension (e.g., Yin and Taylor, 2011).

Traditionally, estimates of crustal thickness beneath Tibet have relied largely on geophysical observations, with important findings contributed by the INDEPTH

(International Deep Profiling of Tibet and the Himalaya) (e.g., Brown et al., 1996; Alsdorf et al., 1998; Zhao et al., 2001, 2008; Karplus et al., 2011; Mechie et al., 2012, 2013) and Hi-CLIMB (Himalayan-Tibetan Continental Lithosphere during Mountain Building) (ie. Nábělek et al., 2009) projects. While these geophysical initiatives have proven extremely valuable for evaluating modern sub-surface structures, they are less useful when estimating crustal thickness in the geologic past. To quantitatively estimate crustal thickness, recent studies have calibrated trace/rare earth element (T/REE) ratios of intermediate igneous rocks in arc settings where Moho depth is well constrained by seismic observations (Chapman et al., 2015; Chiaradia, 2015; Profetta et al., 2015). Further refinement of partition coefficients for trace and rare earth elements have allowed for more robust estimation of whole rock chemistry from individual zircon minerals (e.g., Chapman et al., 2016), making these calculations applicable to single grain analytical techniques (e.g., LA-ICP-MS). When coupled with geochronologic analysis from the same sample, these proxies provide time-sensitive, quantitative crustal thickness estimates that can be used as a test of competing models for the development of ancient orogenic systems.

To understand how ongoing east-west extension relates to these crustal thickness trends, we focus our attention on north-striking normal faults concentrated in the central and southern portions of the Lhasa terrane of southern Tibet. These normal faults can be divided into two classes, herein referred to as Tibetan and Gangdese rifts (Figure 1). We define Tibetan rifts as terrane-scale rift valleys (>150 km in length) that generally strike between 0° and 030°. We define Gangdese rifts as small scale (<150 km in length) rifts

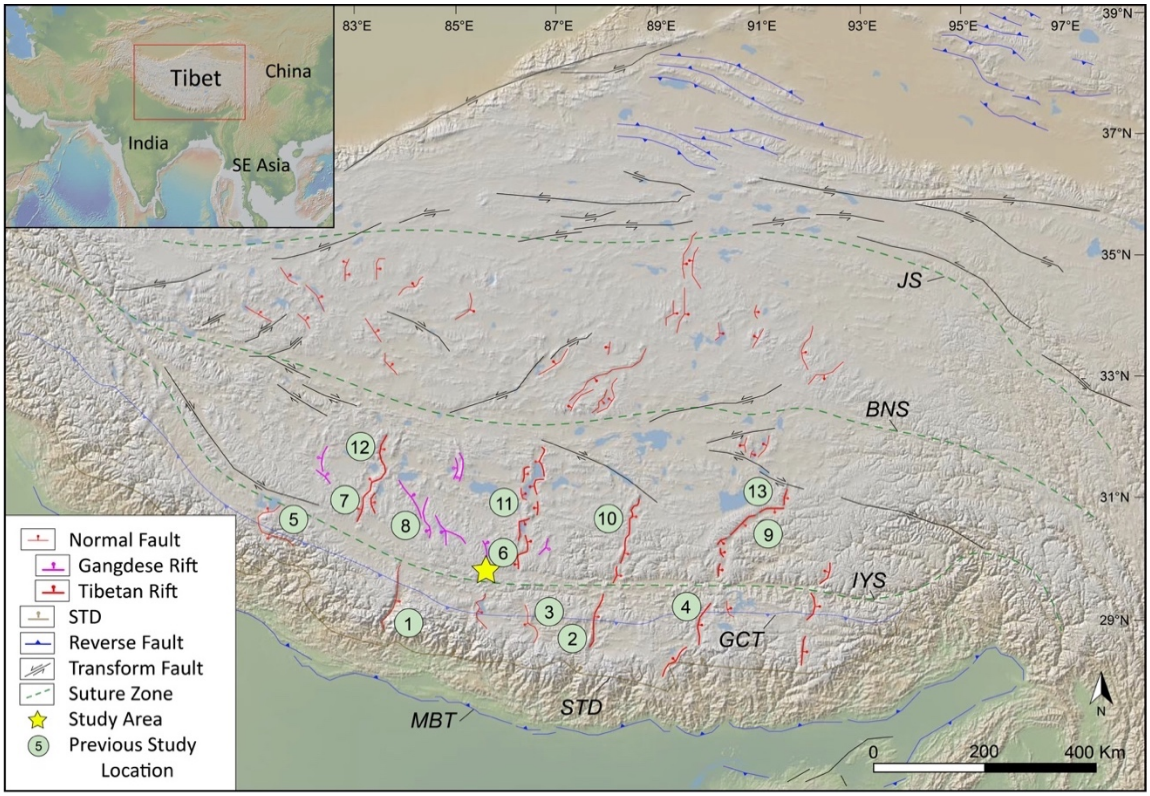

Figure 1. Topographic map of the Tibetan Plateau highlighting major deformational structures and suture zones (adapted from Taylor and Yin, 2009). Basemap is a Global Multi-Resolution Topography (GRMT) synthesis (Ryan et al. 2009) digital elevation model rendered in the GeoMapApp (geomapapp.org). Numbered green dots represent locations of previous studies investigating Miocene extension in central and southern Tibet, adapted from Sundell et al. (2013). Studies are labelled with numbers increasing from SSW to NNE (measured orthogonal to the IYS zone): 1. Thakkhola Graben (Coleman et al., 1995), 2. Ama Drime Massif (Kali et al., 2010), 3. Kung Co Graben (Lee et al., 2011), 4. Ringbung Graben (Ratschbacher et al., 2011), 5. Gurla Mandhata Dome (Murphy et al., 2002; McCalister et al., 2014), 6. Daggyai Tso Graben (Williams et al., 2001; Yin and Harrison, 2000), 7. South Lunggar Rift (Styron et al., 2013), 8. Lopu Kangri Rift (Murphy et al., 2010; Sanchez et al, 2010, 2013; Laskowski et al., 2017), 9. Nyainquentanghala Shan (Harrison et al., 1995; J. Kapp et al., 2005), 10. Pum Qu-Xanza Rift (Hager et al., 2009), 11. Tangra Yumco Graben (Dewane et al., 2006; Wolff et al., 2019), 12. North Lunggar Rift (Kapp et al., 2008; Sundell et al., 2013), 13. Gulu Rift (Stockli et al., 2002). MBT=Main Boundary Thrust; STD=South Tibetan Detachment; GCT=Great Counter Thrust; IYS=Indus-Yarlung Suture; BNS=Bangong-Nujiang Suture; JS=Jinsha Suture. For additional extension timing information, see Figure 9.

localized to high topography in the Gangdese Range located along the southern margin of the Lhasa terrane, generally striking between 330° and 0°. Numerous studies have focused on constraining the plateau's recent phase of east-west extension along Tibetan rifts (e.g., Sundell et al., 2013; Styron et al., 2015; Laskowski et al., 2016; Wolff et al, 2019), however the difference in dynamics between these regional-scale features and Gangdese rifts has only been investigated by few (e.g., Yin, 2000).

Previous studies of east-west extension have led to several leading dynamic models for syncontractional extension along the Himalayan-Tibetan orogen. These include (1) lateral collapse of the plateau as a result of gravitational potential energy outweighing collisional forces (e.g., Molnar & Tapponnier (1975, 1978); Dewey, 1988), (2) convective removal of the lower layer of Tibet's over-thickened lithosphere (England & Houseman, 1989), and (3) coeval thickening and collapse driven by underthrusting Indian lithosphere (e.g., Kind et al., 2002; Kapp and Guynn, 2004; Styron et al., 2015). Each of these models calls for a different driving mechanism to explain the onset of east-west extension in the Lhasa terrane in southern Tibet. To test these competing models, we present new geologic mapping, U-Pb geochronology, ZHe thermochronology, Lu-Hf isotope geochemistry, and T/REE crustal thickness estimates from a Gangdese rift just north of the Indus-Yarlung Suture (IYS), herein referred to as the Dajiamang Tso Rift (DTR) (Figure 1). These data provide further insight into the timing of east-west exhumation events throughout the plateau, as well as time sensitive crustal thickness estimates spanning the proposed period of India-Eurasia collision.

Geologic Setting

Rock Units

The Dajiamang Tso Rift is located in the Gangdese Range (a.k.a. Transhimalaya Range) of southern Tibet (Figure 2a). This region is located within the Lhasa terrane immediately north of the IYS and is comprised of four major lithologic units. The northernmost of these is the Linzizong Formation (Lee et al., 2009), a nonmarine sedimentary unit containing volcanic and volcaniclastic rocks of Late Cretaceous-Early Paleogene age (e.g., Maluski et al., 1982; Coulon et al., 1986; Pan et al., 2004; Lee et al., 2007). The Linzizong volcanic rocks are interpreted to be genetically liked with plutonic igneous rocks of the Gandese Batholith, which mainly crop out to the south in the Dajiamang Tso region (Figure 2b). These calc-alkaline intrusive rocks of the Gangdese Batholith (Schärer et al., 1984) comprise the second major unit in the southern Gandese Range and are roughly age-equivalent to the overlying Linzizong volcanic rocks. Formation histories of both lithologic units are associated with continental arc magmatism as a result of northward subduction of Neo-Tethyan lithosphere during Late Cretaceous-Paleogene time (Lee et al., 2009).

Nonmarine, conglomeratic strata equivalent to the Kailas Formation (Gansser, 1964; Aitchison et al., 2002; DeCelles et al., 2011; Leary et al., 2016, Shen et al., 2019) are well exposed to the south of the Gandese Batholith rocks (Figure 2b). Detrital and igneous U-Pb zircon ages constrain the timing of deposition to the Oligocene-Miocene transition (DeCelles et al., 2011), with work by Leary et al. (2016) identifying a trend of younging deposition from 26-24 Ma in western Tibet (81°E) to 23-22 Ma in the east near

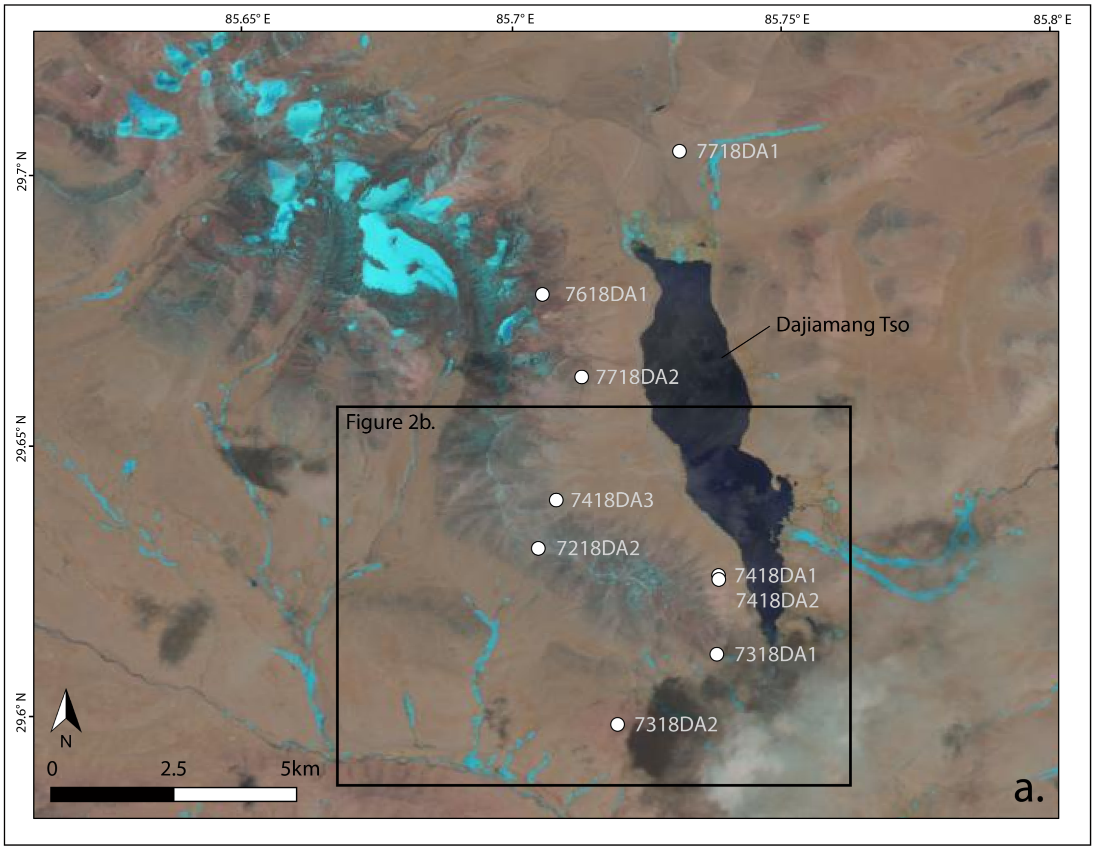

Figure 2a. Satellite image showing the Dajiamang Tso region of southern Tibet. The black box represents the mapping area highlighted in Figure 2b. White circles with labels represent sampling localities and sample names, respectively.

Dazhuka (89.8°E). Farthest south, Cretaceous-Paleogene Xigaze forearc strata (Einsele et al., 1994; Dürr et al., 1996; An et al., 2014; Orme and Laskowski, 2016; Wang et al., 2012, 2017; Orme et al. 2015, 2019) are juxtaposed against Kailas Formation. strata across a steeply south-dipping reverse fault (Figure 2b).

Fault Systems

The Great Counter Thrust. The most pronounced contractional structure in the southern Gandese Range is a system of south-dipping reverse faults referred to as the

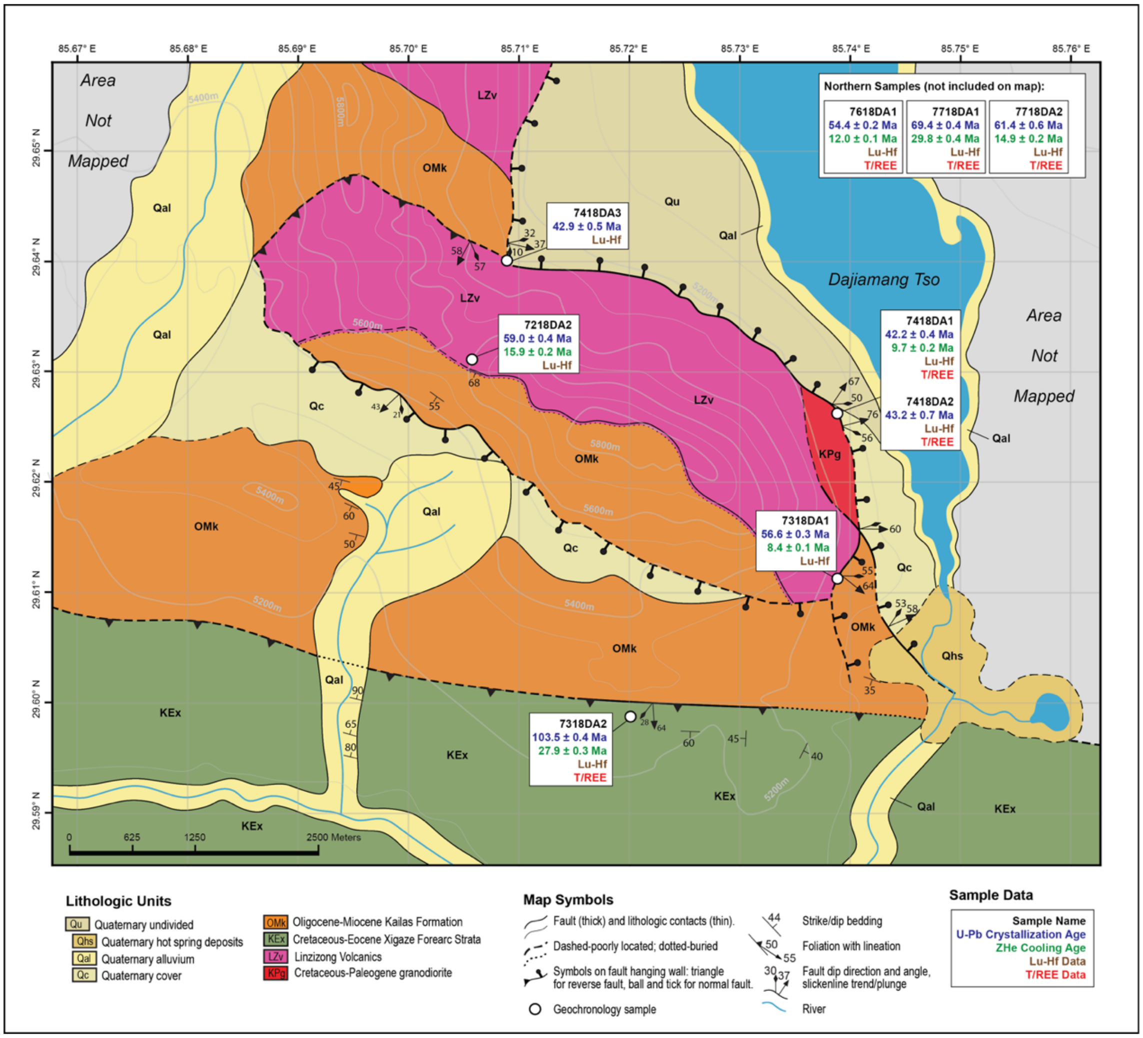

Figure 2b. 1:40,000 scale geologic map of the Dajiamang Tso Rift field area (from figure 2a) highlighting lithologic units, structures, and sample locations. Sample locations are represented by white circles, with sample name, U-Pb geochronology crystallization age, ZHe thermochronology cooling age, and indicators for Hf and T/REE datasets included in adjacent information panels. Data for overlapping structural measurements were averaged for map clarity. Information panels for three samples collected north of the mapping area are also provided in the top right corner of the map.

Great Counter Thrust (GCT) which places Xigaze forearc strata in the hanging wall on top of Kailas Formation strata in the footwall in the region north of the Indus-Yarlung Suture Zone (Heim and Gassner, 1939; Yin et al., 1999; Murphy and Yin, 2003). Initiation of the Great Counter Thrust system is interpreted at c.a. 23 Ma based on provenance changes and clast compositions in the upper Kailas Formation in the Lazi region of southern Tibet (DeCelles et al., 2011), with the younger limit for activity constrained by the transition from north-south contraction to east-west extension in the region, evidenced by Tibetan rifts cross-cutting the GCT in several locations (Laskowski et al. 2016). Earliest estimates for the onset of east-west extension range from c.a. 18 Ma to 14 Ma (e.g., Williams et. al., 2001; Murphy et al., 2010; Sanchez et al., 2013; Styron et al., 2013, Laskowski et al., 2017), requiring that the GCT was inactive by this time. Despite its exposure throughout much of southern Tibet, slip magnitudes along this thrust system remain poorly constrained due to erosion or burial of the hanging wall and footwall cutoffs, respectively.

Gangdese Rifts. The southern and central Tibetan Plateau is in a current constrictional strain state dominated by orogen parallel extension as indicated by the current GPS velocity field (e.g., Zhang et al., 2004). North-striking Tibetan rifts cross-cut the entire Lhasa terrane, are kinematically connected with strike-slip structures along the Bangong-Nuinag suture zone and the Qiangtang terrane, and are consistent with and accommodate the current GPS velocity field (Figure 1) (Taylor et al., 2003; Sundell et al., 2013). Along the southern boundary of the Lhasa terrane, Gangdese rifts constitute a sub-set of Tibetan rifts, characterized by shorter along-strike lengths (<150 km). These extensional structures are localized in the high topography area of the Gangdese drainage divide (Yin, 2000) (Figure 1). Gangdese rifts are commonly expressed as a central horst block bounded by moderate-to-steeply east-and-west dipping normal faults. The horst blocks are high relief ranges with range-bounding normal faults cutting quaternary sediments along their base, and locally, active hot spring and associated tuff deposits observed at lower elevations (Figure 2b).

Methods

Field Methods and Sample Preparation

Geological mapping at 1:40,000 scale was conducted for a ~100 km^2 field area along the southern portion of the Dajiamang Tso Rift (Figure 2b). Field observations were augmented with remote sensing data to make structural observations of fault-related features and observe structural relationships of lithologic units. Nine igneous samples (eight granitoid and one re-worked tuff) were collected from normal fault footwalls for geochronological, thermochronological, and geochemical analysis. Samples were separated at the Institute of Tibetan Plateau Research in Beijing, China using standard disaggregation, density, and magnetic separation techniques.

Zircon U-Pb Geochronology

Igneous zircon grains (n=20 to n=50) for each sample were mounted on 1-inch diameter epoxy pucks alongside crystal standards FC (Paces and Miller, 1993; Schmidtz et al., 2003), R33 (Black et al., 2004), and SL (Gehrles et al., 2008). Mounts were polished to ~20μm to reveal crystal cores and subsequently imaged using backscatter electron and cathodoluminescence techniques for navigation purposes and further grain evaluation. U-Pb geochronology was conducted at the Arizona LaserChron Center (ALC) using Laser Ablation-Inductively Coupled Plasma-Mass Spectrometry (LA-ICP-MS) following techniques in Gehrels et al. (2006, 2008) and Gehrels and Pecha (2014).

Analyses used a Photon Machines G2 laser connected to an Element 2 ICPMS with a jet pump and interface (Pullen et al., 2018). Spot sizes measured 20µm and ablation pits were ~15µm deep, with analyses conducted with an Element 2 ICP-MS. Reported weighted mean ages were calculated using the TuffZirc algorithm (Ludwig and Mundil, 2002) from Berkley Geochronology Center's ISOPLOT program (Ludwig, 2003). Discordant analyses were excluded from the weighted mean age calculation, as well as grains containing inherited cores or those suspected of lead loss.

Lu-Hf Isotope Geochemistry

Single-grain Lu-Hf isotope geochemistry using LA-ICP-MS was conducted at ALC for a subset of zircon (n=4 to n=11) from all nine samples. Ablation used a Photon Machines Analyte G2 excimer laser equipped with a HelEx cell and analysis used a Nu Plasma HR ICP-MS. Grains whose U-Pb analysis were used to calculate the weighted mean age for each sample were targeted for Lu-Hf analysis, while grains with discordant or imprecise ages were not analyzed. Hf analyses used a spot size of 40µm and were conducted on top of U-Pb analysis pits to ensure that Hf isotopic data was determined from the same crystal domain as the U-Pb age (Gehrles and Pecha, 2014).

Zircon Trace/Rare Earth Element Geochemistry

Single-grain trace/rare earth element geochemical analyses of zircon was conducted at ALC using LA-ICP-MS. T/REE analyses were conducted on the same Element 2 ICPMS as U-Pb geochronology. Analyses of each grain involved measurement of 23 trace and rare earth elements, as well as elements used for U-Th-Pb geochronology including ^{27}Al, ^{29}Si, ^{31}P, ^{45}Sc, ^{49}Ti, ^{89}Y, ^{93}Nb, ^{139}La, ^{140}Ce, ^{141}Pr, ^{146}Nd, ^{152}Sm, ^{153}Eu, ^{157}Gd, ^{159}Tb, ^{164}Dy, ^{165}Ho, ^{166}Er, ^{169}Tm, ^{174}Yb, ^{175}Lu, ^{177}Hf, ^{161}Ta, ^{202}Hg, ^{204}(Hg+Pb), ^{206}Pb, ^{207}Pb, ^{208}Pb, ^{232}Th, ^{235}U, and ^{238}U, with dwell times ranging from 0.001 to 0.3 seconds. T/REE analyses used a spot size of 30μm and were conducted on top of U-Pb analysis pits following procedures outlined in Gehrles and Pecha (2014) for Lu-Hf analyses.

ZHe Thermochronology

ZHe thermochronology was performed on the same suite of samples at the Arizona Radiogenic Helium Dating Laboratory at the University of Arizona following procedures outlined in Reiners (2005). Five grains from each sample were hand-selected based on size (diameter > 60μm), morphology (subhedral to euhedral), lack of inclusions, and optical clarity. High resolution photomicrographs were used to measure and record crystal dimensions following procedures outlined in in Hourigan et al. (2005), with euhedral grains with geometric morphologies favored to more accurately estimate alpha-ejection corrections. Measured grains were subsequently packaged in ~1mm Nb foil envelopes to ensure even ablation during analyses. Zircons in Nb foil packets were loaded into a vacuum laser cell and individually heated for 15 minutes using a focused beam from a 1-2 W laser to extract ^{4}He gas. Zircon packets were then reheated at least one time for 15 minutes until ^{4}He yields were less than 2% of the compounded total. ^{4}He/^{3}He ratios were measured using a quadrupole mass spectrometer equipped with a Channeltron electron multiplier. Fish Canyon Tuff (FCT) standards with a (U-Th)/He age of 28.48 ± 0.06 Ma (2σ) (Schmitz and Bowring, 2003) were analyzed between every group of five unknowns (Reiners, 2005). Grains that yielded high effective uranium (eU, U + 0.235 x Th), a proxy for radiation damage (e.g., Guenthner et al., 2013) were further examined within their structural context when interpreting sample cooling ages.

HeFTy Thermal Modeling

Inverse modeling was conducted using the software program HeFTy version 1.9.3 (Ketcham et al., 2005) to test a range of thermal histories that could provide good fits to data generated by ZHe thermochronology. This approach utilizes a Monte-Carlo algorithm that generates thermal histories (n=10,000) based on search constraints in the model's time-temperature space. Characteristics (raw date, ppm U, ppm Th) from euhedral zircon grains with minimal inclusions and radii >35um were used for model runs. HeFTy inverse modeling was executed based on calibrations from Guenthner et al. (2013) and He diffusion characteristics (stopping distances) from Ketcham et al. (2011). The searchable space for time-temperature paths was defined by the following input parameters:

(1) Zircons extracted from extrusive samples were erupted at surface temperatures between 0 and 20°C at the time of crystallization measured by U-Pb geochronology.

(2) Zircons extracted from intrusive samples were exposed to temperatures between 700° and 900°C at the time of crystallization measured by U-Pb geochronology.

(3) ZHe cooling ages require burial of extrusive samples to at least 140°C and potentially to 200°C (within the ZHe partial retention zone) (Guenthner et al., 2013) following crystallization.

(4) Samples were collected at surface temperatures between 0 and 25°C at 0 Ma.

Crustal Thickness Calculations

Ratios of pressure-sensitive trace/rare earth elements such as Sr/Y and La/Yb have been calibrated to provide quantitative estimates of crustal thickness in orogenic settings where Moho depth is well constrained by seismic observations (Chapman et al., 2015; Chiaradia, 2015; Profeta et al., 2015). These ratios rely on the preferential incorporation of Sr and La into minerals such as plagioclase at low pressures and temperatures, and Y and Yb into minerals including garnet and amphibole at higher pressure temperature conditions (Chapman et al., 2015). Thus, magmas that undergo partial melting at greater depths will have relatively high Sr/Y and La/Yb ratios compared to those generated in settings with lower crustal thicknesses.

Empirical calibration of these ratios to modern crustal thicknesses was conducted by Profeta et al. (2015), allowing application to orogenic settings hosting igneous rocks of intermediate composition. Geochemical data were filtered to include rocks with 55-68 wt. % SiO_2, 0-4% MgO, and average Rb/Sr ratios between 0.05 and 0.2 to exclude ultramafic/mantle-derived melts, high silica granites, and rocks formed by partial melting of pre-existing metasedimentary rocks (Profeta et al., 2015). Recent work by Sundell et al. (2021) revisited and recalibrated these ratios to better account for extreme crustal thickness estimated from high ratios and application to the Himalayan-Tibetan orogen.

Single grain zircon T/REE abundances were converted to whole rock geochemistry and normalized to Chondrite-normalized Uniform Reservoir (CHUR) after Chapman et al. (2016), and subsequently used in the revised crustal thickness equation from Sundell et al. (2021):

$$d_m = (17.0 \pm 3.7) \times \ln(La/Yb_n) + (6.9 \pm 5.8) \text{ (at } 2\sigma)$$

where d_m refers to depth of the crust-mantle boundary (crustal thickness). Crustal thickness estimates are reported with a ± 10.8 km (2σ) uncertainty based on residuals from the proxy recalibration outlined in Sundell et al. (2021).

Compilation of Geochemical Data for South-Central Tibet

To evaluate Lu-Hf isotope and single-grain zircon T/REE geochemical data produced from this study in a regional context, previously published geochemical data from south-central Tibet were downloaded from the Tibetan Magmatism Database on March 23rd, 2020 (Chapman and Kapp, 2017). Each data set was filtered to include samples collected between 28-32° North and 82-92° East, with U-Pb crystallization ages ≤ 200 Ma. For T/REE geochemistry, data were further filtered using the parameters of Profeta et al. (2015) mentioned in the previous section. From this reduced dataset, quantitative crustal thickness estimates were calculated using the approach of Sundell et al. (2020, 2021).

Results

Geologic Mapping Results

Rock Units and Correlations. The northernmost rocks in the Dajiamang Tso Rift field area are porphyritic rhyolite with quartz-feldspar phenocrysts and pyroclastic flow deposits with incorporated volcaniclastic sandstone clasts (Figure 2b). We correlate these rocks with the Paleocene-Eocene volcanic and volcaniclastic rocks of the Linzizong Formation (Lee et al., 2009). In the eastern third of the map area, quartz-feldspar-biotite granodiorite locally intruded by aphanitic dikes shares an intrusive contact with the rhyolite unit. We correlate these rocks to the Cretaceous-Paleogene calc-alkaline intrusive rocks of the Gangdese Batholith (Schärer et al., 1984). In the central portion of the map area, sandstone and cobble-boulder conglomerate containing porphyritic andesite is exposed. We correlate these rocks with Oligocene-Miocene nonmarine conglomeratic strata of the Kailas Formation based on similar facies and clast compositions exposed along the suture zone (Gansser, 1964; Aitchison et al., 2002; DeCelles et al., 2011; Leary et al., 2016, Shen et al., 2019). The southernmost rocks of the Dajiamang Tso Rift field area are litharenites and re-worked tuff, which we correlate to forearc basin strata of the Cretaceous-Paleogene Xigaze Group, part of the forearc basin in southern Tibet (Einsele et al., 1994; Dürr et al., 1996; An et al., 2014; Orme and Laskowski, 2016; Wang et al., 2012, 2017; Orme et al. 2015, 2019).

Fault Systems. In the southern portion of the map area, Xigaze forearc strata are juxtaposed atop nonmarine strata of the Kailas Formation along a moderately south-dipping, top-to-the-north reverse fault (Figure 2b). This fault dips approximately 64° to the south and exhibits fault grooves consistent with a top-to-the-northeast oblique sense of motion. We interpret this structure to represent a splay of the regionally extensive Great Counter Thrust system (Figure 1) (Heim and Gassner, 1939; Yin et al., 1999; Murphy and Yin, 2003). Approximately 4 km north of the GCT splay, Linzizong Formation volcanic and volcaniclastic rocks are juxtaposed against Kailas Formation strata in the hanging wall of a second steeply south-dipping, top-to-the-north reverse fault. Exposure of this structure is limited; however, similar geometries and kinematics lead us to interpret that this fault is likely a splay of the Great Counter Thrust system.

Gangdese Rifts. The Dajiamang Tso Rift is characterized by a central horst block bound by two moderate-to-steeply dipping (43-76°) normal faults. The horst is expressed as a high relief range that exposes Gangdese Batholith granodiorite, Linzizong Formation volcanic rocks, and Kailas Formation strata (Figure 3). The range trends NW-SE in the central part of the field area before transitioning to a nearly N-S trend farther north.

U-Pb Geochronology, Lu-Hf Isotope Geochemistry, and T/REE Geochemistry Results

Nine igneous samples were collected from bedrock exposures in the Dajiamang Tso Rift region for zircon U-Pb geochronology, Lu-Hf isotope geochemistry, and T/REE geochemistry. Seven samples were collected from igneous outcrops located in the central horst structure of the rift, one sample was collected from a re-worked tuff in the hanging wall of the GCT, and one sample was collected from a volcanic outcrop in the Dajiamang Tso rift valley. Igneous samples were divided into three groups based on their age distributions and rock type: (1) volcanic and volcaniclastic rocks of the Linzizong Formation (7318DA1, 7218DA2, 7718DA2, 7718DA1), (2) Gandese batholith

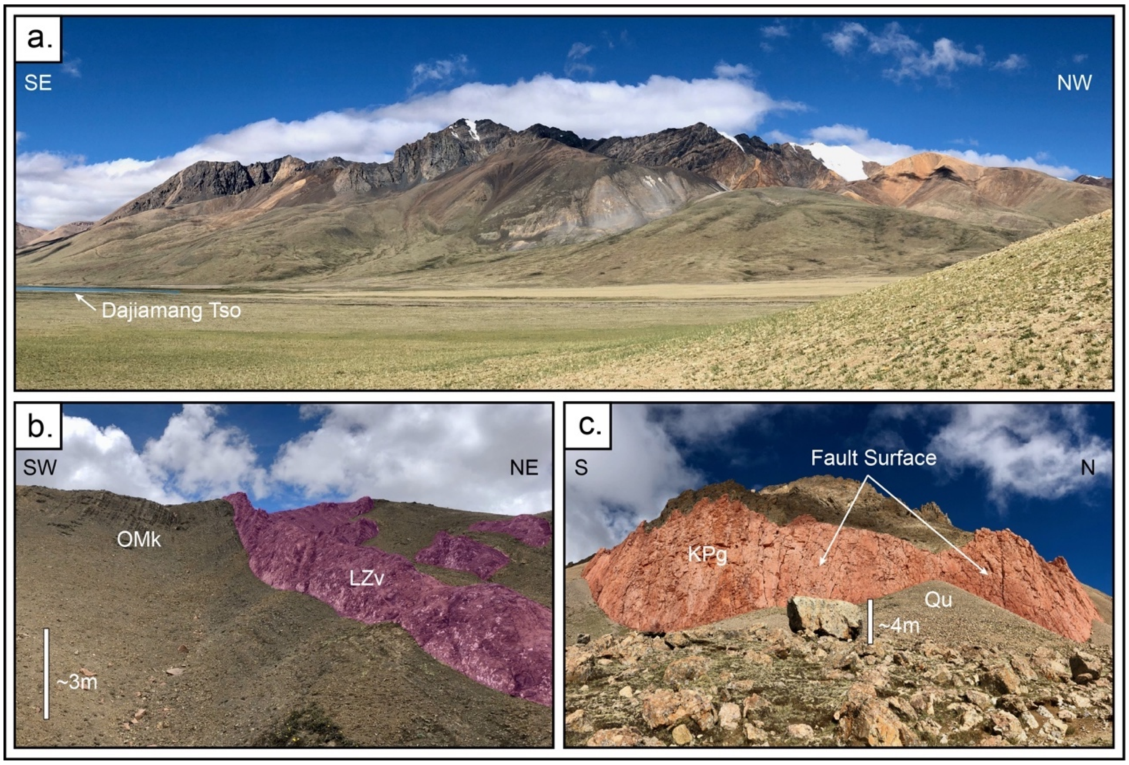

Figure 3. Selected field photos from the Dajiamang Tso Rift mapping area. (a) Southwest facing view of the DTR's central horst block, expressed as a roughly NNW-SSE trending, high relief range. (b) Northwest facing view of the depositional contact between Oligocene-Miocene nonmarine conglomeratic strata of the Kailas Formation (OMk) and Paleocene-Eocene volcanic rocks of the Linzizong Formation (LZv). (c) West facing view of Cretaceous-Paleogene rocks of the Gangdese Batholith (KPg), displaying a major fault surface at the southeast extent of the range.

granodiorites and associated dikes and fault rocks (7418DA1, 7418DA2, 7618DA1, 7418DA3), and (3) Xigaze forearc tuff in the hanging wall of the GCT (7318DA2). Analytical results tables for each method can be found in APPENDIX A, B, and C.

Group 1: Linzizong Formation Volcanic Rocks. Sample 7318DA1 is porphyritic diorite with quartz and feldspar phenocrysts. This sample was collected just north of the Kailas basal contact in the footwall of the Dajiamang Tso Rift in the southeast corner of the mapping area (Figure 2b). Zircon U-Pb geochronology for this sample produced a weighted mean age of 56.6 ± 0.3 Ma (n=15, mean square weighted deviate (MSWD)=3.0) (Figure 4). Lu-Hf isotopic analysis for this sample yielded εHf values from -4.4 ± 0.9 to 0.4 ± 0.9 (Figure 5). No T/REE geochemical data was collected for this sample.

Sample 7218DA2 is porphyritic rhyolite with quartz and feldspar phenocrysts. This sample was collected on top of the ridge-forming horst of the Dajiamang Tso Rift, just north of the contact with Kailas Formation strata in the center of mapping area. Zircon U-Pb geochronology for this sample produced a weighted mean age of 59.0 ± 0.4 Ma (n=20, MSWD=4.0) (Figure 4). Lu-Hf isotopic analysis for this sample yielded εHf values from -4.1 ± 1.1 to 1.5 ± 1.4 (Figure 5). No T/REE geochemical data was collected for this sample.

Sample 7718DA2 is aphanitic rhyolite. This sample was collected from the Dajiamang Tso Rift footwall, approximately 250m west of the inferred normal fault that bounds the central horst range to the east (Figure 2b). Zircon U-Pb geochronology for this sample produced a weighted mean age of 61.4 ± 0.56 Ma (n=21, MSWD=8.9) (Figure 4). Lu-Hf isotopic analysis for this sample yielded εHf values from -7.5 ± 1.2 to -1.8 ± 1.1 (Figure 5). La/Yb(n) ratios ranged from 5.8 to 10.7, with a mean of 7.9. Crustal thickness estimates (n=8) determined from this sample range from 37 ± 10.8 km to 47 ± 10.8 km, with a mean calculated thickness of 42 km (Figure 6).

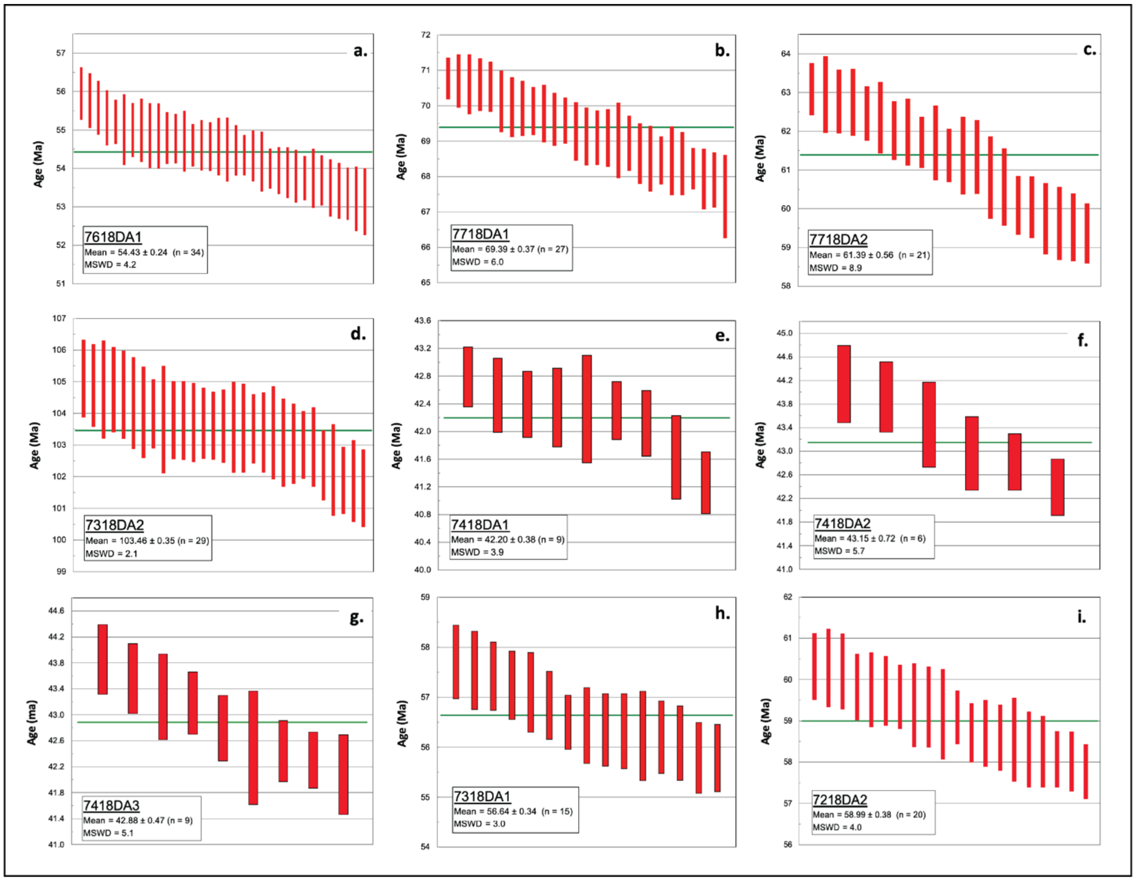

Figure 4. Zircon U-Pb geochronology weighted-mean age results by sample (a-i). Ages were calculated using the TuffZirc algorithm (Ludwig and Mundil, 2002) from Berkley Geochronology Center's ISOPLOT program (Ludwig, 2003). Box heights are 2σ. Panels in the lower left of each graph display sample name, weighted-average crystallization age, sample size, and MSWD (mean square weighted deviate). Complete zircon U-Pb Geochronology results for individual grains can be found in APPENDIX A.

Sample 7718DA1 is fine-grained rhyolite with rare phenocrysts of quartz and biotite. This sample was collected ~2 km north of the lake that occupies the Dajiamang Tso rift valley and is the northernmost sample. Zircon U-Pb geochronology for this sample produced a weighted mean age of 69.4 ± 0.4 Ma (n=27, MSWD=6.0) (Figure 4). Lu-Hf isotopic analysis for this sample yielded εHf values from -8.4 ± 1.1 to -2.4 ± 1.3

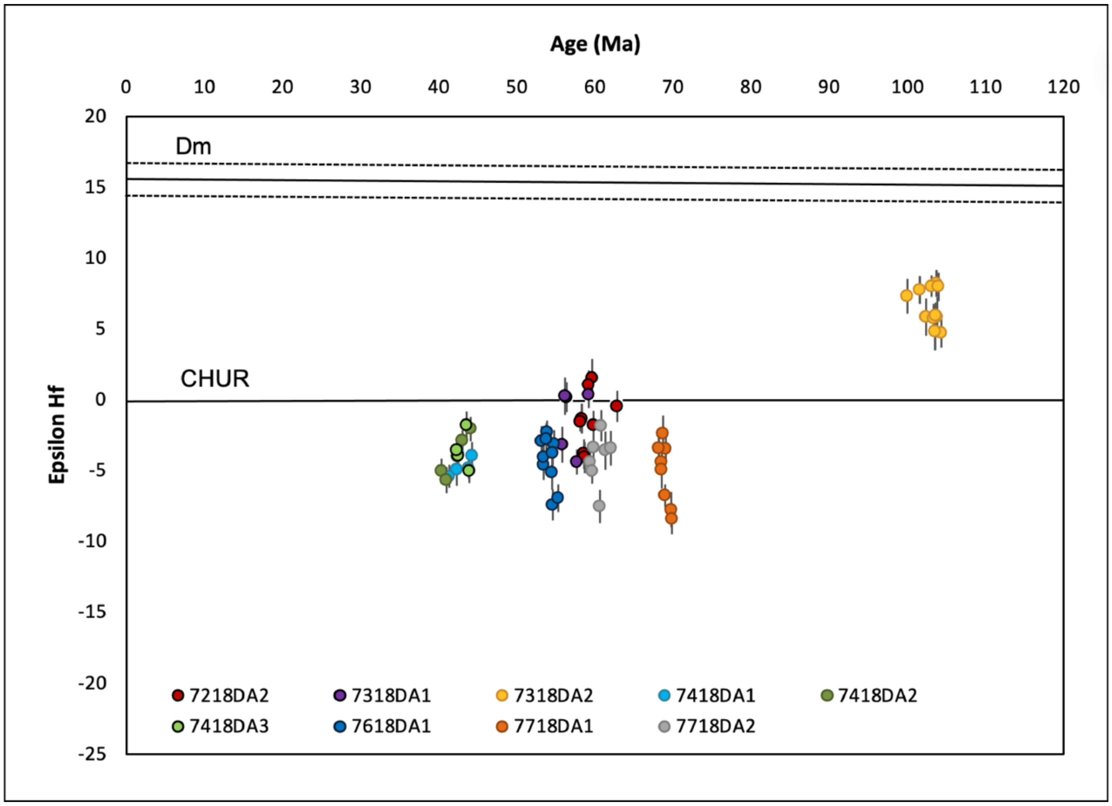

Figure 5. Epsilon Hf (^{176}Hf/^{177}Hf) values for igneous zircons plotted against corresponding U-Pb geochronology crystallization ages. More negative values represent more evolved isotopic signatures. Chondritic Uniform Reservoir (CHUR) line depicts expected crustal composition of bulk silicate earth. Depleted Mantle (DM) line represents the natural depletion of incompatible elements within the mantle over time. Note the change in εHf values from ~100 Ma grains to 70-40 Ma grains. Complete zircon Lu-Hf isotope geochemistry results for individual grains can be found in APPENDIX B.

(Figure 5). La/Yb(n) ratios ranged from 3.7 to 13.8, with a mean of 7.1. Crustal thickness estimates (n=15) determined from this sample range from 29 ± 10.8 km to 47 ± 10.8 km, with a mean calculated thickness of 39 km (Figure 6).

Group 2: Gandese Batholith Granodiorites and Associated Dikes and Fault Rocks.

Sample 7418DA1 is a is quartz-feldspar-biotite granite. This sample was collected from

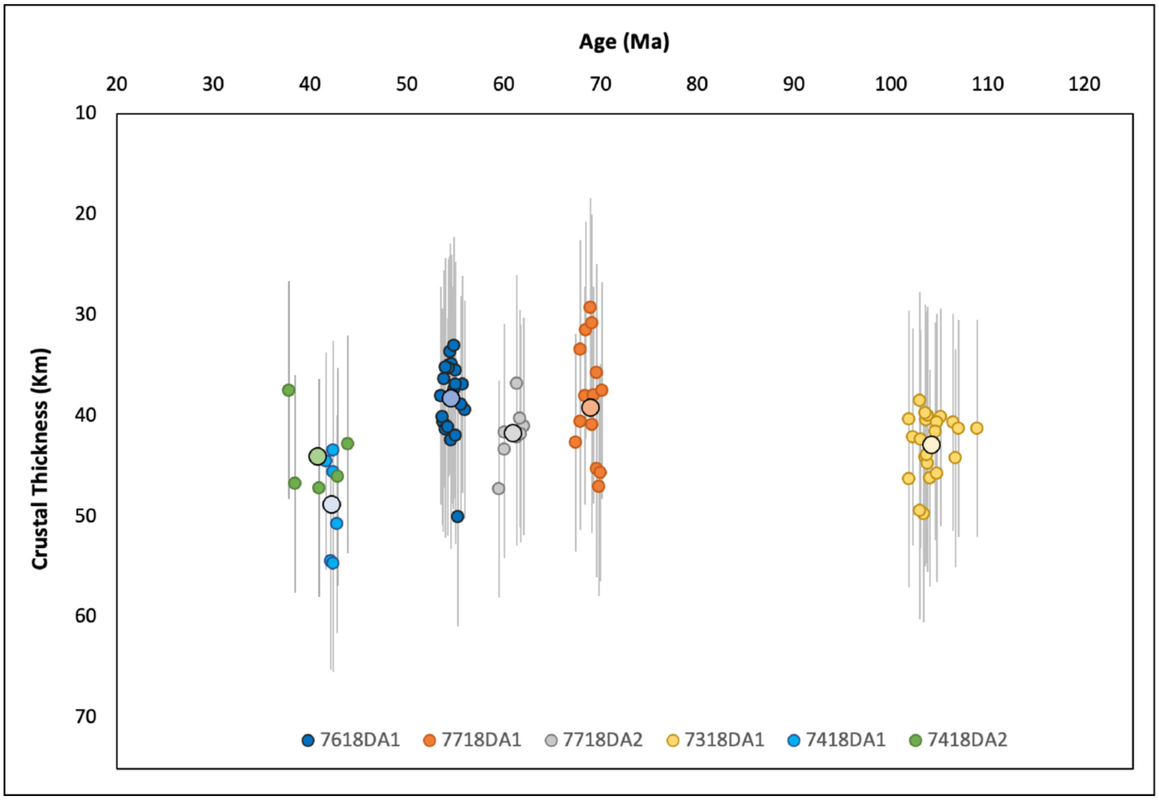

Figure 6. Trace/Rate Earth Element (T/REE) geochemistry crustal thickness estimates for igneous zircons plotted against corresponding U-Pb geochronology crystallization ages. Crustal thickness estimates were calculated using the equations of Sundell et al. (2020, 2021) modified from the original equations calibrated by Profeta et al. (2015). These equations utilize La/Yb ratios as proxies for depth of magma diversification and thus, crustal thickness at the time of crystallization. Error bars represent ±10.8 km (2σ) residuals after Sundell et al. (2020, 2021). Large circles with black outlines represent mean age and crustal thickness estimates for each sample Moving right to left through time across the chart, average crustal thickness estimates decrease thickness from ~100 Ma to ~70 Ma, followed by increasing thickness estimates until ~40 Ma. Complete zircon TREE geochemistry results for individual grains can be found in APPENDIX C.

the Dajiamang Tso Rift footwall in the central-eastern portion of the mapping area. Zircon U-Pb geochronology for this sample produced a weighted mean age of 42.2 ± 0.4Ma (n=9, MSWD=3.9) (Figure 4). Lu-Hf isotopic analysis for this sample yielded εHf values from -5.4 ± 0.8 to -3.7 ± 0.7 (Figure 5). La/Yb(n) ratios ranged from 8.5 to 16.5, with a mean of 12.2. Crustal thickness estimates (n=6) determined from this sample range from 43 ± 10.8 km to 54 ± 10.8 km, with a mean calculated thickness of 48 km (Figure 6).

Sample 7418DA2 is a medium-gray-green, aphanitic dike that intrudes sample 7418DA1. This sample was collected in the Dajiamang Tso Rift footwall. Zircon U-Pb geochronology for this sample produced a weighted mean age of 43.2 ± 0.7 Ma (n=6, MSWD=5.7) (Figure 4). Lu-Hf isotopic analysis for this sample yielded εHf values from -5.7 ± 0.9 to -2.1 ± 0.9 (Figure 5). La/Yb(n) ratios ranged from 6.0 to 10.6, with a mean of 9.0. Crustal thickness estimates (n=5) determined from this sample range from 37 ± 10.8 km to 47 ± 10.8 km, with a mean calculated thickness of 44 km (Figure 6).

Sample 7618DA1 is undeformed granodiorite containing quartz, feldspar, biotite and hornblende. This sample was collected from the Dajiamang Tso Rift footwall, approximately 550m west of the inferred normal fault that bounds the central horst range to the east and approximately 2 km northwest of 7718DA2 (Figure 2b). Zircon U-Pb geochronology for this sample produced a weighted mean age of 54.4 ± 0.2 Ma (n=34, MSWD=4.2) (Figure 4). Lu-Hf isotopic analysis for this sample yielded εHf values from -7.4 ± 1.1 to -2.3 ± 0.9 (Figure 5). La/Yb(n) ratios ranged from 4.6 to 12.6, with a mean of 6.5. Crustal thickness estimates (n=23) determined from this sample range from 33 ± 10.8 km to 50 ± 10.8 km, with a mean calculated thickness of 38 km (Figure 6).

Sample 7418DA3 is silicified breccia with hematite, collected from a 0.75m fault zone where the central range of the Dajiamang Tso Rift changes strike from NW-SE to

N-S in the northern section of the mapping area. Zircon U-Pb geochronology for this sample produced a weighted mean age of 42.9 ± 0.5 Ma (n=9, MSWD=5.1) (Figure 4). Lu-Hf isotopic analysis for this sample yielded εHf values from -5.0 ± 0.8 to -1.8 ± 1.0 (Figure 5). No T/REE geochemical data was collected for this sample.

Group 3: Xigaze Group Forearc Rocks. Sample 7318DA2 is white volcanic tuff with quartz, feldspar, and biotite phenocrysts interbedded with medium grained lithic sandstone, interpreted to represent Xigaze Group forearc basin strata (e.g., Orme and Laskowski, 2016). This sample was collected ~100m south of the GCT in the southern portion of the mapping area. Zircon U-Pb geochronology for this sample produced a weighted mean age of 103.5 ± 0.4 Ma (n=29, MSWD=2.1) (Figure 4). Lu-Hf isotopic analysis for this sample yielded εHf values from 4.7 ± 1.0 to 8.2 ± 1.0 (Figure 5). La/Yb(n) ratios ranged from 6.4 to 12.4, with a mean of 8.4. Crustal thickness estimates (n=22) determined from this sample range from 38 ± 10.8 km to 50 ± 10.8 km, with a mean calculated thickness of 43 km (Figure 6).

ZHe Thermochronology and HeFTy Thermal History Modelling Results

ZHe cooling ages were calculated for seven igneous samples collected from the Dajiamang Tso Rift field area. These samples are divided into two groups: (A) samples collected from within the footwall/central horst of the Dajiamang Tso Rift (7318DA1, 7218DA2, 7718DA2, 7418DA1, 7618DA1), and (B) samples collected from within the hanging wall of the Dajiamang Tso Rift and GCT (7718DA1, 7318DA2). ZHe cooling ages were determined for five zircons per sample, with reported mean cooling ages and errors representing the averages of all grains from each sample.

Samples collected from the within the horst block of the Dajiamang Tso Rift display a range in ZHe cooling ages from 15.9 ± 0.2 to 8.4 ± 0.1 Ma. Ages from this group show a roughly positive correlation with sample elevation as well as a positive correlation with average horizontal distance measured perpendicular to range bounding faults (Figure 7). No correlations with grain size or eU are present. Samples collected from the hanging walls of the Dajiamang Tso Rift and GCT record cooling ages from approximately 30-28 Ma. No major trends are visible in these data given the small sample size (n=2). The following sections report ZHe cooling ages and HeFTy inverse modeling results for each sample. Complete analytical results for ZHe thermochronology and HeFTy input parameters can be found in APPENDIX D and E, respectively.

Group A: Dajiamang Tso Footwall Rocks. Analysis of five zircon grains separated from sample 7318DA1 produced a range in cooling ages from 10.05 ± 0.12 to 6.91 ± 0.08 Ma. All five analyses were used to calculate a mean sample cooling age of 8.4 ± 0.1 Ma. HeFTy modeling results for this sample display significant variation in potential time-temperature paths from zircon's crystallization at ~58 Ma to its passage through the He partial retention zone (HePRZ) at ~8 Ma (Figure 8a). There is, however, significant overlap of "good" and "acceptable" paths beginning at ~36 Ma, suggesting monotonic cooling until the sample reached surface conditions at present. Using this concentration of paths, we estimate an exhumation rate of 0.61 km/Myr since 36 Ma for this sample.

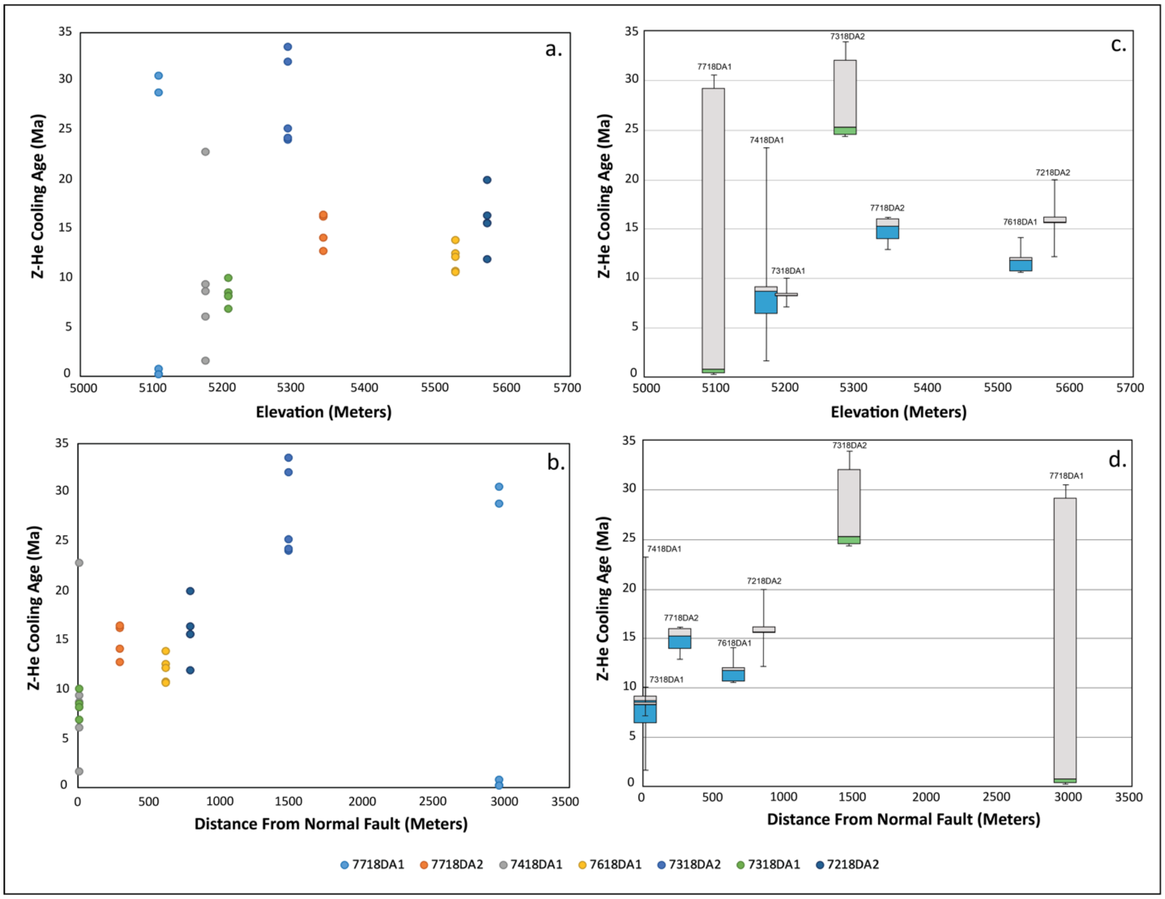

Figure 7. ZHe thermochronology cooling ages plotted vs. elevation (a) and vs. distance measured orthogonal from the trace of the horst-bounding normal fault (b). Panels (c) and (d) are box and whisker plots visually depicting the same data presented in panels (a) and (b). Samples depicted with blue and gray box and whisker plots were collected from the central horst of the Dajiamang Tso Rift (DTR), while the green and gray box and whisker plots represent the two samples collected from the hanging walls of the DTR and Great Counter Thrust (GCT). The line dividing the two colors within each box and whisker plot represents the median, the lower and upper box boundaries represent the 1st and 3rd quartiles respectively, and the error bars represent the minimum and maximum values of the analyzed grains. Note roughly positive correlations within footwall samples (blue/gray) between ZHe cooling age and (1) elevation and (2) distance from the normal fault.

Analysis of five zircon grains separated from sample 7218DA2 produced a range in cooling ages from 19.99 ± 0.25 to 11.95 ± 0.15 Ma. All five analyses were used to calculate a mean sample cooling age of 15.9 ± 0.2 Ma. HeFTy modeling results for this

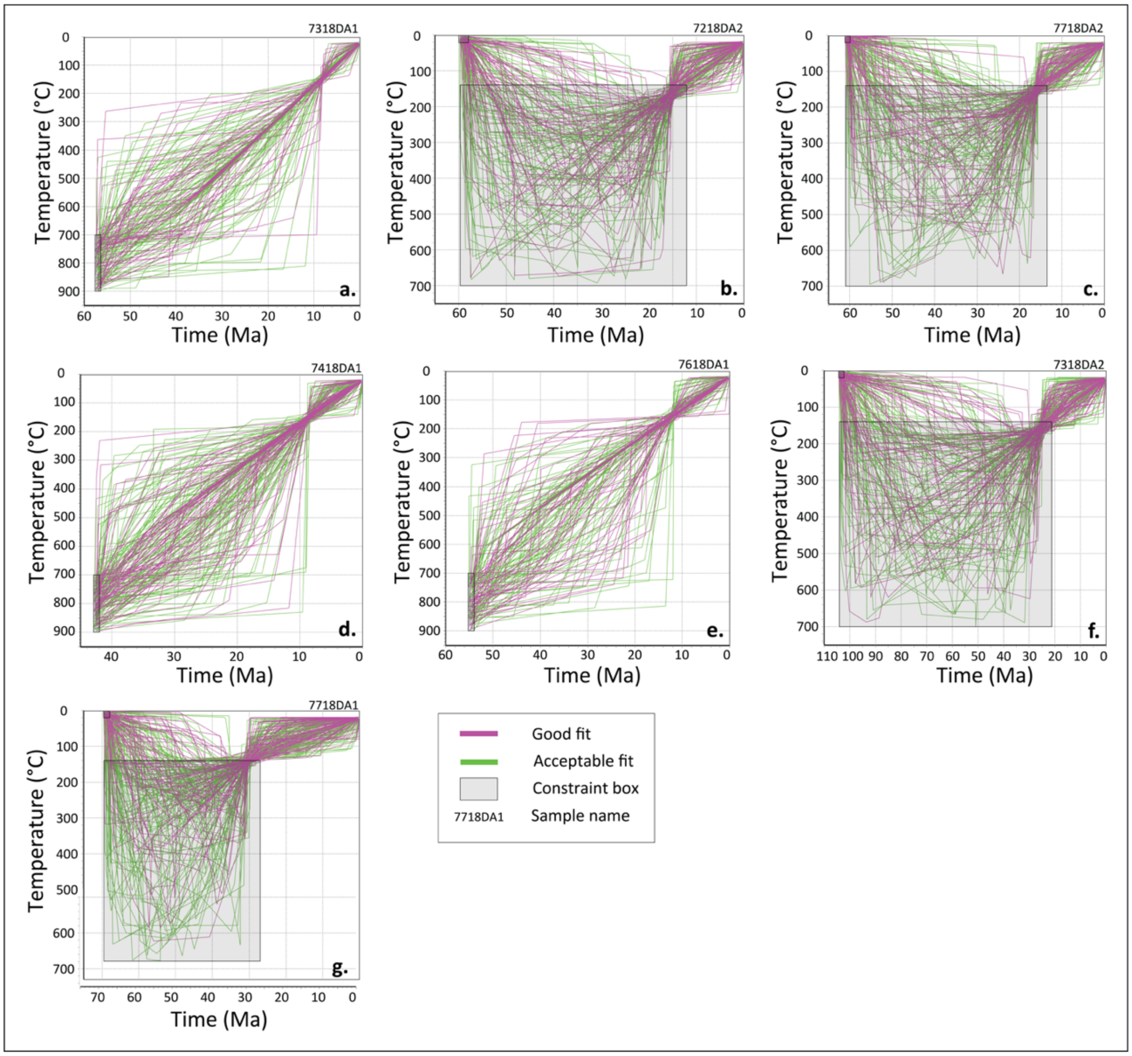

Figure 8. HeFTy inverse modeling (Ketcham et al., 2005) results displaying “good” (purple) and “acceptable” (green) time-temperature paths for each sample based on n=10,000 model runs. Black boxes with gray shading represent geologic controls: For intrusive samples, U-Pb geochronology ages were used in conjunction with assumed zircon crystallization temperatures between 900°-700°C to constrain path start points. For extrusive samples, U-Pb geochronology ages were used with assumption that samples were erupted at surface conditions (0°-25°C) to constrain path start points. Subsequent constraint boxes were implemented for extrusive samples because ZHe cooling ages require burial up to at least 140° (within the ZHe partial retention zone (PRZ)) following crystallization. All model runs require T-t paths to terminate at surface conditions (25°C) at 0 Ma. “Best fit” and “weighted mean” paths are not displayed to allow the viewer to better identify concentrations of “good-fit” path clusters.

sample display considerable variation in potential time-temperature paths from zircon's crystallization at ~59 Ma, subsequent burial, and ascent through the HePRZ at ~16 Ma (Figure 8b). No major concentrations of "good" or "acceptable" paths were observed to calculate exhumation rates for this sample.

Analysis of four zircon grains separated from sample 7718DA2 produced a range in cooling ages from 16.48 ± 0.21 to 12.76 ± 0.16 Ma. For this sample, we report a mean cooling age of 14.9 ± 0.2 Ma. HeFTy modeling results for this sample display considerable variation in potential time-temperature paths following zircon's crystallization at ~60 Ma and subsequent burial prior to exhumation at ~15 Ma (Figure 8c). No major concentrations of "good" or "acceptable" paths were observed to calculate exhumation rates for this sample.

Analysis of five zircon grains separated from sample 7418DA1 produced significant intrasample variation in cooling ages, ranging from 22.86 ± 0.41 to 1.62 ± 0.03 Ma. Effective uranium concentrations display a large range from approximately 800 to 9900 ppm. Including all five analyses, we report a mean cooling age of 9.7 ± 0.2 Ma for this sample. HeFTy modeling results for this sample display significant variation in potential time-temperature paths from zircon's crystallization at ~42 Ma to its passage through the HePRZ at ~9 Ma (Figure 8d). There is, however, significant overlap of "good" and "acceptable" paths beginning at ~26 Ma, suggesting monotonic cooling until the sample reached surface conditions at present. Using this concentration of paths, we estimate an exhumation rate of 0.62 km/Myr since ~26 Ma for this sample.

Analysis of five zircon grains separated from sample 7618DA1 produced a range in cooling ages from 13.90 ± 0.16 to 10.63 ± 0.12 Ma. For this sample, we report a mean cooling age of 12.0 ± 0.1 Ma. HeFTy modeling results for this sample display significant variation in potential time-temperature paths from zircon's crystallization at ~54 Ma to its passage through the HePRZ at ~12 Ma (Figure 8e). The sample displays significant overlap of "good" and "acceptable" paths beginning at ~36 Ma, suggesting monotonic cooling until the sample reached surface conditions at present. Using this concentration of paths, we estimate an exhumation rate of 0.44 km/Myr since ~36 Ma for this sample.

<u>Group B: Local Hanging Wall Rocks</u>. Sample 7318DA2 is the southernmost sample and was collected in the hanging wall proximal to the GCT. Analysis of five zircon grains separated from this sample produced a range in cooling ages from 33.56 ± 0.40 to 24.12 ± 0.29 Ma. For this sample, we report a mean cooling age of 27.9 ± 0.3 Ma. HeFTy modeling results for this sample display considerable variation in potential time-temperature paths following zircon's crystallization at ~103 Ma, subsequent burial, and its ascent through the HePRZ at ~28 Ma (Figure 8f). No major concentrations of "good" or "acceptable" paths were observed to calculate exhumation rates for this sample.

Sample 7718DA1 is the northernmost sample and was collected in the low elevation hanging wall of the Dajiamang Tso Rift. Analysis of five zircon grains separated from this sample produced significant intrasample variation in cooling ages, ranging from 30.62 ± 0.36 to 0.19 ± 0.01 Ma. Three of the five grains yielded very little He and near-zero ages compared to other grains and were therefore excluded. For this sample, we report a mean cooling age of 29.8 ± 0.4 Ma. HeFTy modeling results for this sample display considerable variation in potential time-temperature paths following zircon's crystallization at ~69 Ma, subsequent burial, and its ascent through the HePRZ at ~30 Ma (Figure 8g). The majority of "good" paths are concentrated cooler than 300°C, possibly indicating that the sample was buried at relatively shallow depths (≤~12 km).

Discussion

Tectonic Integration

Neo-Tethyan Subduction Along the Southern Margin of the Lhasa Terrane. The oldest igneous crystallization age from this study (103.5 ± 0.4 Ma) comes from a re-worked volcanic tuff collected from within Xigaze forearc basin stratigraphy, reflecting coeval volcanism in the Gangdese Range during mid-Cretaceous time. At this period in the development of the southern Lhasa terrane, ongoing north-directed subduction of the Neo-Tethyan oceanic slab produced Gangdese Arc magmatism until ~90 Ma, followed by a period of decreased forearc deposition rates and a lull in Gangdese magmatism that persisted until ~70 Ma (Kapp and DeCelles, 2019). U-Pb geochronology ages of approximately 70-42 Ma from granodiorites of the Gangdese Batholith and overlying volcanic rocks of the Linzizong Formation suggest there was active magmatism along the Gangdese magmatic arc preceding and throughout the proposed period for the initiation of India-Eurasia collision (~58 Ma) (DeCelles et al., 2014; Orme et al., 2015; Hu et al., 2016). A recent geologic synthesis of Tibet by Kapp and DeCelles (2019) provides two leading hypotheses to explain the lull and associated high-T metamorphism and adakitic magmatism in SE Tibet: (1) Neo-Tethyan flat slab subduction and (2) formation and subsequent closure of a backarc basin within the Gandese arc (the "Xigaze backarc basin”). These hypotheses require dramatically different tectonic configurations and will be further addressed within the context of this study later in the discussion (section 5.4).

Post-Collisional Deformation Along the Gangdese Thrust and Great Counter Thrust. The oldest ZHe cooling age produced from this study comes from sample 7718DA1 (29.8 ± 0.4 Ma) collected ~5 km north of the mapping area in the hanging wall of the Dajiamang Tso Rift. This sample displays a significantly older age than nearby footwall samples, suggesting different structural mechanisms for cooling. It is possible that this relatively older cooling age represents south-directed exhumation in the hanging wall of the north-dipping Gangdese Thrust (GT), as previous work on this regional structure suggests that the southernmost splay of the thrust fault became active by ~27 Ma (Yin et al., 1994). The older cooling age of ~30 Ma could potentially represent cooling via exhumation along an older, unmapped splay of the GT (Figure 7).

The sample with the second oldest ZHe cooling age was collected from Xigaze forearc strata in the hanging wall of the south-dipping GCT (Heim and Gansser, 1939). Analysis of this sample produced a mean cooling age of 27.9 ± 0.3 Ma, which we interpret to represent hanging wall erosion during northward thrusting along the GCT. This cooling age appears slightly older than previous estimates for thrusting along the GCT (23-17 Ma) (Heim and Gansser, 1939; Zhang et al., 2011; Laskowski et al., 2018), but falls within the range of approximately 30-10 Ma for other local ZHe cooling ages from Xigaze forearc basin strata near Saga (Orme, 2019). Thermal modeling conducted by Orme (2019) suggests that Xigaze forearc samples were buried to maximum temperatures of 140-200 °C by 35-21 Ma, immediately followed by exhumation, indicating that the cooling age produced from this study is compatible with the burial and exhumation of Xigaze forearc strata in this region.

The last group of ZHe cooling ages comes from samples collected within the central horst of the Dajiamang Tso Rift. These samples display cooling ages from 15.9 ± 0.2 Ma to 8.4 ± 0.1 Ma, which we attribute to footwall exhumation of the Dajiamang Tso Rift. Prior to their late Miocene exhumation via east-west extension, HeFTy thermal modeling (Ketchum, 2005) suggests that volcanic rock samples were buried up to 5-7 km by overlying volcanic rocks and/or Kailas Formation strata (Figures 2, 7). The Kailas basin has been variably interpreted as a peripheral foreland basin (Searle et al., 1987; Harrison et al., 1992), an extensional basin related to rollback of Greater Indian Lithosphere (DeCelles et al., 2011), a foreland basin related to a doubly-vergent orogenic wedge at the time of India-Eurasia collision (Wang et al., 2015), and most recently as a flexural basin produced by Greater India rollback, with slab breakoff causing flexural rebound and thrusting ultimately inverting Kailas strata (Webb et al., 2017). While the formation history of the Kailas basin remains unclear, U-Pb geochronology of a tuff bed constrains the depositional age of basin strata to 26-24 Ma (DeCelles et al., 2011). We interpret that Kailas sediments combined with overlying Linzizong volcanic rocks provided the overburden necessary to reset the (U-Th)/He system of more deeply buried Linzizong volcanic samples prior to their exhumation in the DTR.

Constraints on the Timing of Extension Along North-Striking Rifts

Gangdese Rifts.

The geology, geochronology, and thermochronology of the Dajiamang Tso Rift are consistent with a normal fault characterized by a central horst bound by NNE and SSW-dipping normal faults. ZHe thermochrnology results for igneous rocks collected from within the footwall of the DTR display a range in cooling ages from approximately 16-8 Ma, providing a minimum age for the onset of east-west extension in southern Tibet. This minimum age of ~16 Ma appears consistent with the findings of numerous studies of other Gangdese rifts (Figure 1). Similar (± 2 Ma) minimum ages of extension produced by previous studies include a U-Pb crystallization age of ~18 Ma for north-striking dikes located near the Daggyai Tso graben (Williams et al., 2001), an ^{40}Ar-^{39}Ar age of ~15 Ma for movement along the Lopu Kangri rift (Murphy et al., 2010; Sanchez et al., 2013), and an ^{40}Ar-^{39}Ar age of ~14 Ma for north-striking mineralized fractures near the Thakkhola graben (Coleman et al., 1995; Garizone et al., 2000) (Figure 9). Many of these Gangdese rifts also show evidence of recent exhumation and seismogenic activity, including young ZHe cooling ages (e.g., Laskowski et al., 2017) and fault scarps offsetting quaternary landforms consistent with active east-west extension (e.g., Zhang et al., 2004; Gan et al., 2007).

Tibetan Rifts. To better understand possible linkages in extensional processes between the two scales of rifts, we compare results produced from this research to previous thermochronology studies of Tibetan Rifts. In south-western Tibet, ZHe cooling ages coupled with U-Pb geochronology of a tuff in the western basin of the South Lunggar Rift suggest that east-west extension was underway by ~17 Ma (Styron et al., 2013). In the North Lunggar Rift, Kapp et al. (2008) and Sundell et al. (2013) reported minimum extensional ages of ~10 Ma for the same Tibetan rift system, suggesting that considerable N-S variation in minimum timing of extension may exist within these extensional structures (Figure 9). Approximately 300 km east, Tangra Yumco represents another regional-scale normal fault. Wolff et al. (2019) interprets extension along this rift system as underway by ~13 Ma based on zircon and apatite-He thermochronology and Apatite Fission Track data. The Pum Qu-Xainza and Nyainqentanghla Shan rifts are located farther to the east and display minimum ages of extension of ~ 15 Ma (Harrison et al., 1995; J. Kapp et al., 2005) (Figures 1, 9).

ZHe cooling ages from the Dajiamang Tso Rift reported here overlap with published cooling ages for other Gandese and Tibetan rifts. Based on this study alone, we cannot confidently identify any significant difference in timing for the initiation of extension between the two classes of rifts. When observing both rift classes together, we can however identify a spatial relationship throughout the Tethyan Himalaya, with north-striking rifts displaying progressively younger extension estimates moving from SSW to NNE (orthogonal to the IYS) (Figure 9). This trend is also present, albeit less well-defined, for rifts in the Lhasa terrane north of the IYS zone.

Despite an overlap in timing for the initiation of Gangdese and Tibetan rift extension, the two rift classes display distinctly different orientations when viewed at the plateau-scale (Figure 10). Gangdese rifts generally strike between 330° and 350° with a subset of rift segments that strike ~030°. Tibetan rift segments tend to strike between 0° and 15°, however also display a subset of rift segments that strike ~030°. This apparent difference in orientation was one of the initial observations that inspired our investigation into Gangdese rifts. We postulate that active uplift of the Gangdese Range or kinematic linkage with Karakorum fault system to the northwest could be contributing factors to the

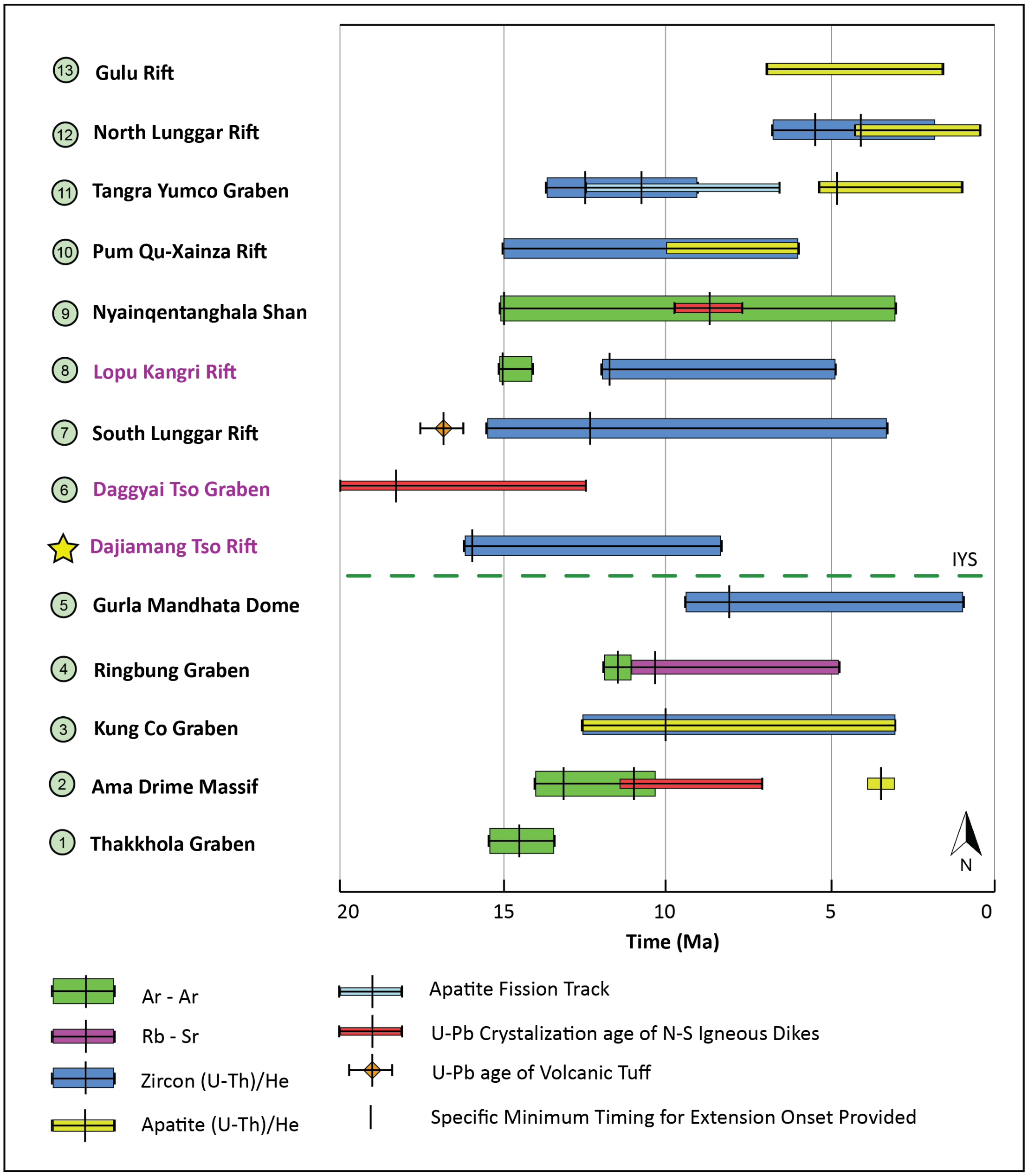

Figure 9. Regional correlation figure comparing ZHe cooling ages from this study to minimum timing estimates for the onset of east-west extension from previously studied rifts throughout central and southern Tibet. Rift numbers increase from SSW-NNE (measured orthogonal to the suture zone) and correspond to studies referenced in Figure 1. Gangdese Rift names are labeled in purple (corresponding to Figure 1) and Tibetan Rift names are labelled in black. The Indus-Yarlung Suture (IYS) zone is also included for spatial reference. Horizontal colored bars represent the range of measurements (including errors) while vertical black ticks represent the earliest evidence of extension observed for each technique.

different surface expressions of the two rift classes, however further investigation is required to provide a higher resolution look at these possible linkages.

Crustal Evolution and Crustal Thickness Trends

Lu-Hf isotope geochemistry is a valuable tool for evaluating the evolution of continental crust (Hawkesworth and Kemp, 2005). Typically, Lu-Hf isotope data is presented as εHf values vs. corresponding U-Pb age, with more evolved (negative) εHf values at the time of crystallization representing more incorporation of older and more evolved crustal material. εHf values for the oldest sample from this study (~103 Ma) and the youngest samples (~43-42 Ma) are generally in agreement with the compiled dataset for southern Tibet, however samples with U-Pb ages from 69-56 Ma display more evolved signatures than similarly aged regional data (Figure 11a). As crustal thickness estimates from the DTR appear consistent with regional data at this time (Figure 11b), the less evolved signatures from the TMDB could be a function of a sample location within a large sampling area throughout southern Tibet. Combined Hf datasets for this region also display a lack of evolved εHf values from ~100 Ma to ~70 Ma, followed by the appearance of increasingly evolved values towards the present. The lack of evolved εHf values combined with the presence of numerous samples with depleted εHf values for this time period may suggest increased tapping of juvenile asthenosphere, or less crust-mantle differentiation, implying assimilation with relatively thin and/or young crust.

T/REE crustal thickness estimates from our study also appear in general agreement with regional data downloaded from the Tibetan Magmatism Database (Chapman and Kapp, 2017) (Figure 11b). From ~190-160 Ma, crustal thickness appears

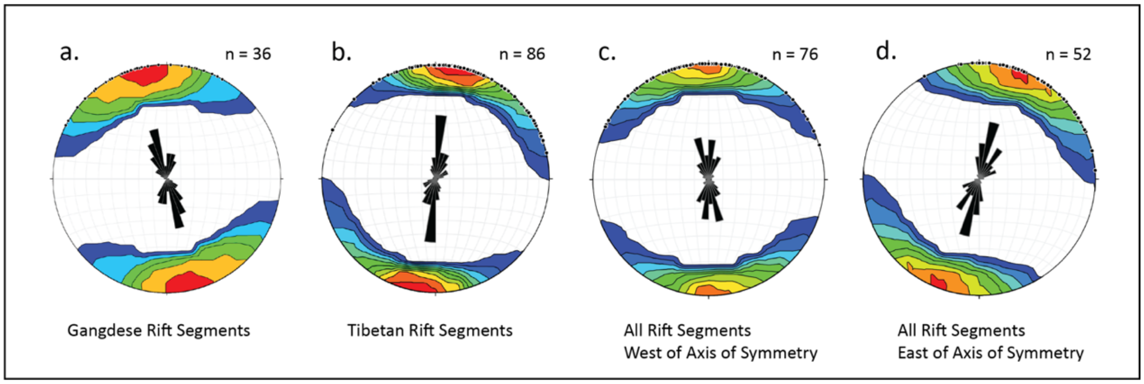

Figure 10. Rose diagrams constructed in Stereonet 11 (Allmendinger, 2020) for rift segments from Gangdese Rifts (a), Tibetan Rifts (b) (see Figure 1), as well as all rifts located to the west (c) and east (d) of the axis of symmetry suggested by Kapp and Guynn (2005). Rifts were measured using Google Earth Pro in 20 km segments to ensure equal weighted representation in rose diagrams. Note that Gangdese Rift segments dominantly strike between 330° and 0°, with a secondary cluster striking between 0° and 030° characteristic of Tibetan Rifts. It is important, however, to acknowledge that all Gangdese Rifts defined in this study are located to the west of the proposed axis of symmetry (Kapp and Guynn, 2005) (Figure 1).

to increase from ~35 to ~45 km, followed by a lack of substantial data until ~105 Ma. From ~105-70 Ma (a period that roughly corresponds with the lack of evolved εHf values), crustal thickness appears to decrease, followed by an increase until ~15 Ma when data are no longer available. Modern crustal thickness estimates based on geophysical of observations range from ~65 km (Zhao et al., 2001; Kind et al., 2002) to ~85 km (Xu et al., 2015) and appear consistent with continued thickening since the last calculated crustal thickness estimate (55-70 km) at 15 Ma.

Tectonic Implications

Geochemical data from this study combined with compiled data from the TMDB provide key insights into the controversial period preceding India-Eurasia collision. The

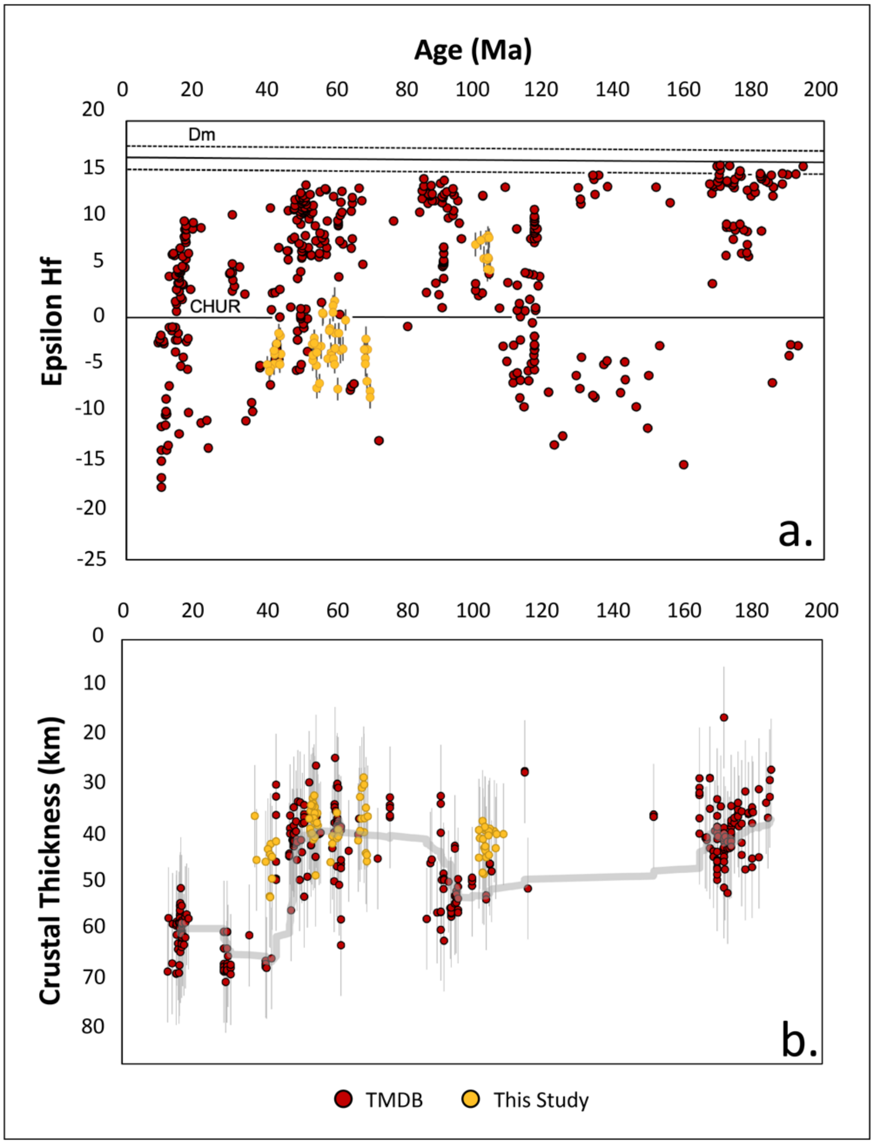

Figure 11. (a) εHf vs. U-Pb geochronology plots for igneous zircons from this study in the context of regional data downloaded from the Tibetan Magmatism Database (TMDB) (Chapman and Kapp, 2017). CHUR and Dm explanations can be referenced in Figure 5. Lu-Hf filtering criteria for TMBD samples can be referenced in the methods section of this paper. (b) T/REE geochemistry crustal thickness estimates vs. U-Pb geochronology crystallization age plots from this study in the context of crustal thickness estimates for regional data downloaded from the Tibetan Magmatism Database (TMDB) (Chapman and Kapp, 2017). TMBD crustal thicknesses were calculated using the equations from Sundell et al. (2020, 2021), with data filtered to exclude ultramafic/mantle derived melts, high silica granites, and rocks formed by partial melting of pre-existing meta-sedimentary rocks. Error bars represent ±10.8 km residuals (Sundell et al., 2020, 2021). Gray trendline represents a moving average with a sampling period of 30 analyses.

lack of evolved εHf values from TMDB data paired with decreasing crustal thickness estimates from 100-70 Ma support a tectonic model for the mid-Cretaceous evolution of the southern Lhasa terrane invoking crustal thinning and upper plate extension. These findings question the traditional interpretation of a simple, Andean-style margin along the southern Lhasa terrane (Kapp et al., 2007), and are more consistent with the opening of a back-arc basin inboard of the Xigaze volcanic arc (Kapp and DeCelles, 2019; Sundell et al., 2020, 2021). This tectonic configuration suggests that continental India initially collided with the rifted Xigaze arc at ~58 Ma, followed by subduction of back-arc oceanic lithosphere until the Xigaze-India collision with Eurasia and the cessation of Gangdese Arc magmatism at ~38 Ma (Laskowski et al., 2017). Additional geologic mapping is needed to determine the viability of the Xigaze backarc basin model, but our data highlight its relevance as an important hypothesis for future studies.

Results from this study also provide tests of models for the Cenozoic tectonic evolution of the Himalayan-Tibetan orogen. If Miocene extension were due to gravitational collapse of the plateau (e.g., Molnar & Tapponnier, 1975, 1978); Dewey, 1988), we would expect peak crustal thickness to be coincident with the timing of extension, with subsequent collapse leading to thinner crust at present. Our results show no indication of crustal thinning following the onset of east-west extension, requiring an alternative explanation for either maintenance or addition of crustal thickness since the establishment of Miocene normal faults. Additionally, if upper plate extension was due to convective removal of the lower layer of Tibet's over-thickened lithosphere (England & Houseman, 1989) we would expect to see a juvenile excursion in Hf isotope data as well as a possible decrease in crustal thickness preceding or coincident with the onset of extension, neither of which are apparent from our compiled datasets.

Data from our study best support a tectonic model in which the addition of crustal material into the Himalayan-Tibetan orogen is facilitated by underthrusting Indian lithosphere (Kind et al., 2002; Kapp and Guynn, 2004; Styron et al., 2015). In this model, crustal thickness in southern Tibet likely reached a critical threshold in the period directly preceding the onset of east-west extension, with modern crustal thicknesses representing underthrusting Indian lithosphere balanced by upper plate extension (Styron et al., 2015). This model would also suggest that the earliest evidence of east-west extension would be localized to high elevation regions in the southern portion of the plateau (i.e. Gangdese Range), with progressive northward underthrusting of Indian lithosphere manifesting on the surface as progressively younger thermochronology ages as you move to the north. While this trend cannot be clearly observed from ages summarized in this study (Figure 9), future work to constrain the timing of the initiation of east-west extension throughout the plateau may further elucidate contributing tectonic processes.

Conclusions

The Dajiamang Tso Rift records development of the southern-central Tibetan Plateau from mid-Cretaceous to Miocene time. U-Pb ages are interpreted to represent Xigaze Group volcanic activity (~103 Ma) as well as Gangdese Batholith and Linzizong Formation magmatism (~70-40 Ma) along the Lhasa terrane’s southern convergent margin. ZHe thermochronology data suggest northward thrusting and erosion of the hanging wall of the GCT (~28 Ma), as well as east-west extension occurring along the

Dajiamang Tso Rift from approximately 16-8 Ma. HeFTy thermal modeling suggests burial of volcanic samples but to 7 km prior to exhumation along north-striking normal faults. Lu-Hf isotope geochemistry results display slightly depleted signatures for the Xigaze sample and slightly enriched signatures for Gandese and Linzizong samples, while compiled data (TMBD) show a lack of evolved signatures from approximately 105-70 Ma. Crustal thickness calculations utilizing T/REE geochemistry presented with regional calculations (TMBD) (Sundell et al., 2020, 2021) suggest crustal thinning from approximately 100-70 Ma, followed by crustal thickening until present. Geochemical data support a tectonic model in which the addition of crustal material into the Himalayan-Tibetan orogen is facilitated by underthrusting Indian lithosphere (Kind et al., 2002; Kapp and Guynn, 2004; Styron et al., 2015), while allowing the possibility for crustal thinning and upper plate extension in the Lhasa terrane prior to India-Eurasia collision (Kapp and DeCelles, 2019).

Literature Cited

Aitchison, J. C., Davis, A. M., & Luo, H. (2002). New constraints on the India–Asia collision: the lower Miocene Gangrinboche conglomerates, Yarlung Tsangpo suture zone, SE Tibet. *Journal of Asian Earth Sciences, 21*(3), 251-263.

Allegre, C. o., Courtillot, V., Tapponnier, P., Hirn, A., Mattauer, M., Coulon, C., . . . Marcoux, J. (1984). Structure and evolution of the Himalaya–Tibet orogenic belt. *Nature, 307*(5946), 17.

Alsdorf, D., Brown, L., Nelson, K. D., Makovsky, Y., Klemperer, S., & Zhao, W. (1998). Crustal deformation of the Lhasa terrane, Tibet plateau from Project INDEPTH deep seismic reflection profiles. *Tectonics, 17*(4), 501-519.

An, W., Hu, X., Garzanti, E., BouDagher-Fadel, M. K., Wang, J., & Sun, G. (2014). Xigaze forearc basin revisited (South Tibet): Provenance changes and origin of the Xigaze Ophiolite. *Bulletin, 126*(11-12), 1595-1613.

Armijo, R., Tapponnier, P., & Han, T. (1989). Late Cenozoic right-lateral strike-slip faulting in southern Tibet. *Journal of Geophysical Research: Solid Earth, 94*(B3), 2787-2838.

Armijo, R., Tapponnier, P., Mercier, J., & Han, T. L. (1986). Quaternary extension in southern Tibet: Field observations and tectonic implications. *Journal of Geophysical Research: Solid Earth, 91*(B14), 13803-13872.

Black, L. P., Kamo, S. L., Allen, C. M., Davis, D. W., Aleinikoff, J. N., Valley, J. W., . . . Williams, I. S. (2004). Improved 206Pb/238U microprobe geochronology by the monitoring of a trace-element-related matrix effect; SHRIMP, ID–TIMS, ELA–ICP–MS and oxygen isotope documentation for a series of zircon standards. *Chemical Geology, 205*(1-2), 115-140.

Brown, L., Zhao, W., Nelson, K., Hauck, M., Alsdorf, D., Ross, A., . . . Che, J. (1996). Bright spots, structure, and magmatism in southern Tibet from INDEPTH seismic reflection profiling. *science, 274*(5293), 1688-1690.

Chapman, J. B., & Ducea, M. N. (2019). The role of arc migration in Cordilleran orogenic cyclicity. *Geology, 47*(7), 627-631.

Chapman, J. B., Ducea, M. N., DeCelles, P. G., & Profeta, L. (2015). Tracking changes in crustal thickness during orogenic evolution with Sr/Y: An example from the North American Cordillera. *Geology, 43*(10), 919-922.

Chapman, J. B., Gehrels, G. E., Ducea, M. N., Giesler, N., & Pullen, A. (2016). A new method for estimating parent rock trace element concentrations from zircon. *Chemical Geology, 439*, 59-70.

Chapman, J. B., & Kapp, P. (2017). Tibetan magmatism database. *Geochemistry, Geophysics, Geosystems, 18*(11), 4229-4234.

Chiaradia, M. (2015). Crustal thickness control on Sr/Y signatures of recent arc magmas: an Earth scale perspective. *Scientific Reports, 5*, 8115.

Coleman, M., & Hodges, K. (1995). Evidence for Tibetan plateau uplift before 14 Myr ago from a new minimum age for east–west extension. *Nature, 374*(6517), 49.

Coulon, C., Maluski, H., Bollinger, C., & Wang, S. (1986). Mesozoic and Cenozoic volcanic rocks from central and southern Tibet: 39Ar-40Ar dating, petrological characteristics and geodynamical significance. *Earth and Planetary Science Letters, 79*(3-4), 281-302.

DeCelles, P. G., Kapp, P., Quade, J., & Gehrels, G. E. (2011). Oligocene–Miocene Kailas basin, southwestern Tibet: Record of postcollisional upper-plate extension in the Indus-Yarlung suture zone. *GSA Bulletin, 123*(7-8), 1337-1362.

DeCelles, P. G., Kapp, P., Gehrels, G. E., & Ding, L. (2014). Paleocene-Eocene foreland basin evolution in the Himalaya of southern Tibet and Nepal: Implications for the age of initial India-Asia collision. *Tectonics, 33*(5), 824-849.

Dewey, J. (1988). Extensional collapse of orogens. *Tectonics, 7*(6), 1123-1139.

Dürr, S. r. B. (1996). Provenance of Xigaze fore-arc basin clastic rocks (Cretaceous, south Tibet). *Geological Society of America Bulletin, 108*(6), 669-684.

Einsele, G., Liu, B., Dürr, S., Frisch, W., Liu, G., Luterbacher, H., . . . Wetzel, A. (1994). The Xigaze forearc basin: evolution and facies architecture (Cretaceous, Tibet). *Sedimentary Geology, 90*(1-2), 1-32.

England, P., & Houseman, G. (1989). Extension during continental convergence, with application to the Tibetan Plateau. *Journal of Geophysical Research: Solid Earth, 94*(B12), 17561-17579.

Gan, W., Zhang, P., Shen, Z. K., Niu, Z., Wang, M., Wan, Y., . . . Cheng, J. (2007). Present-day crustal motion within the Tibetan Plateau inferred from GPS measurements. *Journal of Geophysical Research: Solid Earth, 112*(B8).

Gansser, A. (1964). Geology of the Himalayas.

Garzione, C. N., Dettman, D. L., Quade, J., DeCelles, P. G., & Butler, R. F. (2000). High times on the Tibetan Plateau: Paleoelevation of the Thakkhola graben, Nepal. *Geology, 28*(4), 339-342.

Gehrels, G., & Pecha, M. (2014). Detrital zircon U-Pb geochronology and Hf isotope geochemistry of Paleozoic and Triassic passive margin strata of western North America. *Geosphere, 10*(1), 49-65.

Gehrels, G., Valencia, V., & Pullen, A. (2006). Detrital zircon geochronology by laser-ablation multicollector ICPMS at the Arizona LaserChron Center. *The Paleontological Society Papers, 12*, 67-76.

Gehrels, G. E., Valencia, V. A., & Ruiz, J. (2008). Enhanced precision, accuracy, efficiency, and spatial resolution of U-Pb ages by laser ablation–multicollector–inductively coupled plasma–mass spectrometry. *Geochemistry, Geophysics, Geosystems, 9*(3).

Guenthner, W. R., Reiners, P. W., Ketcham, R. A., Nasdala, L., & Giester, G. (2013). Helium diffusion in natural zircon: Radiation damage, anisotropy, and the interpretation of zircon (U-Th)/He thermochronology. *American Journal of Science, 313*(3), 145-198.

Harrison, T. M., Copeland, P., Kidd, W., & Lovera, O. M. (1995). Activation of the Nyainqentanghla shear zone: Implications for uplift of the southern Tibetan Plateau. *Tectonics, 14*(3), 658-676.

Harrison, T. M., Copeland, P., Kidd, W., & Yin, A. (1992). Raising tibet. *science, 255*(5052), 1663-1670.

Hawkesworth, C., & Kemp, A. (2006). Using hafnium and oxygen isotopes in zircons to unravel the record of crustal evolution. *Chemical Geology, 226*(3-4), 144-162.

Heim, A., & Gansser, A. (1975). *Central Himalaya: Geological observations of the Swiss expedition, 1936* (Vol. 73): Hindustan Publishing Corporation (India).

Hourigan, J. K., Reiners, P. W., & Brandon, M. T. (2005). U-Th zonation-dependent alpha-ejection in (U-Th)/He chronometry. *Geochimica et Cosmochimica Acta, 69*(13), 3349-3365.

Hu, X., Wang, J., BouDagher-Fadel, M., Garzanti, E., & An, W. (2016). New insights into the timing of the India–Asia collision from the Paleogene Quxia and Jialazi formations of the Xigaze forearc basin, South Tibet. *Gondwana Research, 32*, 76-92.

Kapp, J. L. D. A., Harrison, T. M., Kapp, P., Grove, M., Lovera, O. M., & Lin, D. (2005). Nyainqentanglha Shan: a window into the tectonic, thermal, and geochemical evolution of the Lhasa block, southern Tibet. *Journal of Geophysical Research: Solid Earth, 110*(B8).

Kapp, P., & DeCelles, P. G. (2019). Mesozoic–Cenozoic geological evolution of the Himalayan-Tibetan orogen and working tectonic hypotheses. *American Journal of Science, 319*(3), 159-254.

Kapp, P., & Guynn, J. H. (2004). Indian punch rifts Tibet. *Geology, 32*(11), 993-996.

Kapp, P., Taylor, M., Stockli, D., & Ding, L. (2008). Development of active low-angle normal fault systems during orogenic collapse: Insight from Tibet. *Geology, 36*(1), 7-10.

Karplus, M., Zhao, W., Klemperer, S., Wu, Z., Mechie, J., Shi, D., . . . Chen, C. (2011). Injection of Tibetan crust beneath the south Qaidam Basin: Evidence from INDEPTH IV wide-angle seismic data. *Journal of Geophysical Research: Solid Earth, 116*(B7).

Ketcham, R. A. (2005). Forward and inverse modeling of low-temperature thermochronometry data. *Reviews in Mineralogy and Geochemistry, 58*(1), 275-314.

Ketcham, R. A., Gautheron, C., & Tassan-Got, L. (2011). Accounting for long alpha-particle stopping distances in (U–Th–Sm)/He geochronology: refinement of the baseline case. *Geochimica et Cosmochimica Acta, 75*(24), 7779-7791.

Kind, R., Yuan, X., Saul, J., Nelson, D., Sobolev, S., Mechie, J., . . . Achauer, U. (2002). Seismic images of crust and upper mantle beneath Tibet: evidence for Eurasian plate subduction. *science, 298*(5596), 1219-1221.

Laskowski, A. K. (2016). *Tectonic evolution of the Yarlung suture zone, Lopu Range and Lazi Regions, central southern Tibet*: The University of Arizona.

Laskowski, A. K., Kapp, P., & Cai, F. (2018). Gangdese culmination model: Oligocene–Miocene duplexing along the India-Asia suture zone, Lazi region, southern Tibet. *GSA Bulletin, 130*(7-8), 1355-1376.

Laskowski, A. K., Kapp, P., Ding, L., Campbell, C., & Liu, X. (2017). Tectonic evolution of the Yarlung suture zone, Lopu Range region, southern Tibet. *Tectonics, 36*(1), 108-136.

Leary, R., Orme, D. A., Laskowski, A. K., DeCelles, P. G., Kapp, P., Carrapa, B., & Dettinger, M. (2016). Along-strike diachroneity in deposition of the Kailas Formation in central southern Tibet: Implications for Indian slab dynamics. *Geosphere, 12*(4), 1198-1223.

Lee, H., Chung, S., Wang, Y., Zhu, D., Yang, J., Song, B., . . . Wu, F. (2007). Age, petrogenesis and geological significance ofthe Linzizong volcanic successions in the Linzhou basin, southern Tibet: Evidence from zircon U-Pb dates and Hf isotopes.

Lee, H.-Y., Chung, S.-L., Lo, C.-H., Ji, J., Lee, T.-Y., Qian, Q., & Zhang, Q. (2009). Eocene Neotethyan slab breakoff in southern Tibet inferred from the Linzizong volcanic record. *Tectonophysics, 477*(1-2), 20-35.

Ludwig, K., & Mundil, R. (2002). *Extracting reliable U-Pb ages and errors from complex populations of zircons from Phanerozoic tuffs.* Paper presented at the Geochimica et Cosmochimica Acta.

Ludwig, K. R. (2003). Isoplot 3.00: A geochronological toolkit for Microsoft Excel. *Berkeley Geochronology Center Special Publication, 4*, 70.

Maluski, H., Proust, F., & Xiao, X. (1982). 39 Ar/40 Ar dating of the trans-Himalayan calc-alkaline magmatism of southern Tibet. *Nature, 298*(5870), 152-154.

Mechie, J., & Kind, R. (2013). A model of the crust and mantle structure down to 700 km depth beneath the Lhasa to Golmud transect across the Tibetan plateau as derived from seismological data. *Tectonophysics, 606*, 187-197.

Mechie, J., Zhao, W., Karplus, M., Wu, Z., Meissner, R., Shi, D., . . . Xue, G. (2012). Crustal shear (S) velocity and Poisson's ratio structure along the INDEPTH IV profile in northeast Tibet as derived from wide-angle seismic data. *Geophysical Journal International, 191*(2), 369-384.

Molnar, P., & Tapponnier, P. (1975). Cenozoic tectonics of Asia: effects of a continental collision. *science, 189*(4201), 419-426.

Molnar, P., & Tapponnier, P. (1978). Active tectonics of Tibet. *Journal of Geophysical Research: Solid Earth, 83*(B11), 5361-5375.

Murphy, M., Sanchez, V., & Taylor, M. (2010). Syncollisional extension along the India–Asia suture zone, south-central Tibet: Implications for crustal deformation of Tibet. *Earth and Planetary Science Letters, 290*(3-4), 233-243.

Murphy, M., & Yin, A. (2003). Structural evolution and sequence of thrusting in the Tethyan fold-thrust belt and Indus-Yalu suture zone, southwest Tibet. *Geological Society of America Bulletin, 115*(1), 21-34.

Nábělek, J., Hetényi, G., Vergne, J., Sapkota, S., Kafle, B., Jiang, M., . . . Huang, B.-S. (2009). Underplating in the Himalaya-Tibet collision zone revealed by the Hi-CLIMB experiment. *science, 325*(5946), 1371-1374.

Orme, D. A. (2019). Burial and exhumation history of the Xigaze forearc basin, Yarlung suture zone, Tibet. *Geoscience Frontiers, 10*(3), 895-908.

Orme, D. A., Carrapa, B., & Kapp, P. (2015). Sedimentology, provenance and geochronology of the upper Cretaceous–lower Eocene western Xigaze forearc basin, southern Tibet. *Basin Research, 27*(4), 387-411.

Orme, D. A., & Laskowski, A. K. (2016). Basin analysis of the Albian–Santonian Xigaze forearc, Lazi region, south-central Tibet. *Journal of Sedimentary Research, 86*(8), 894-913.

Paces, J. B., & Miller Jr, J. D. (1993). Precise U-Pb ages of Duluth complex and related mafic intrusions, northeastern Minnesota: Geochronological insights to physical, petrogenetic, paleomagnetic, and tectonomagmatic processes associated with the 1.1 Ga midcontinent rift system. *Journal of Geophysical Research: Solid Earth, 98*(B8), 13997-14013.

Pan, G., Ding, J., Yao, D., & Wang, L. (2004). Guidebook of 1: 1,500,000 geologic map of the Qinghai–Xizang (Tibet) plateau and adjacent areas. *Chengdu, China: Chengdu Cartographic Publishing House, 48*.

Profeta, L., Ducea, M. N., Chapman, J. B., Paterson, S. R., Gonzales, S. M. H., Kirsch, M., . . . DeCelles, P. G. (2015). Quantifying crustal thickness over time in magmatic arcs. *Scientific Reports, 5*, 17786.

Pullen, A., Ibáñez-Mejia, M., Gehrels, G. E., Giesler, D., & Pecha, M. (2018). Optimization of a laser ablation-single collector-inductively coupled plasma-mass spectrometer (Thermo Element 2) for accurate, precise, and efficient zircon U-Th-Pb geochronology. *Geochemistry, Geophysics, Geosystems, 19*(10), 3689-3705.

Reiners, P. W. (2005). Zircon (U-Th)/He thermochronometry. *Reviews in Mineralogy and Geochemistry, 58*(1), 151-179.

Sanchez, V., Murphy, M., Robinson, A., Lapen, T., & Heizler, M. (2013). Tectonic evolution of the India–Asia suture zone since Middle Eocene time, Lopukangri area, south-central Tibet. *Journal of Asian Earth Sciences, 62*, 205-220.

Schärer, U., Xu, R.-H., & Allègre, C. J. (1984). UPb geochronology of Gangdese (Transhimalaya) plutonism in the Lhasa-Xigaze region, Tibet. *Earth and Planetary Science Letters, 69*(2), 311-320.

Schmitz, M. D., Bowring, S. A., & Ireland, T. R. (2003). Evaluation of Duluth Complex anorthositic series (AS3) zircon as a U-Pb geochronological standard: New high-precision isotope dilution thermal ionization mass spectrometry results. *Geochimica et Cosmochimica Acta, 67*(19), 3665-3672.

Searle, M., Windley, B., Coward, M., Cooper, D., Rex, A., Rex, D., . . . Thakur, V. (1987). The closing of Tethys and the tectonics of the Himalaya. *Geological Society of America Bulletin, 98*(6), 678-701.

Shen, T., Wang, G., Bernet, M., Replumaz, A., Ai, K., Song, B., . . . Zhang, P. (2019). Long-term exhumation history of the Gangdese magmatic arc: Implications for the evolution of the Kailas Basin, western Tibet. *Geological Journal*.

Styron, R., Taylor, M., & Sundell, K. (2015). Accelerated extension of Tibet linked to the northward underthrusting of Indian crust. *Nature Geoscience, 8*(2), 131.

Styron, R. H., Taylor, M. H., Sundell, K. E., Stockli, D. F., Oalmann, J. A., Möller, A., . . . Ding, L. (2013). Miocene initiation and acceleration of extension in the South Lunggar rift, western Tibet: Evolution of an active detachment system from structural mapping and (U-Th)/He thermochronology. *Tectonics, 32*(4), 880-907.

Sundell, K. E., Taylor, M. H., Styron, R. H., Stockli, D. F., Kapp, P., Hager, C., . . . Ding, L. (2013). Evidence for constriction and Pliocene acceleration of east-west extension in the North Lunggar rift region of west central Tibet. *Tectonics, 32*(5), 1454-1479.

Sundell, K., Laskowski, A. K., Kapp, P. A., & Ducea, M. N. (2020, December). Jurassic to Neogene quantitative crustal thickness estimates in southern Tibet from recalibrated Sr/Y and La/Yb trace element geochemical proxies. In *AGU Fall Meeting* 2020. AGU.

Sundell, K., Laskowski, A. K., Kapp, P. A., & Ducea, M. N. (2021). Jurassic to Neogene quantitative crustal thickness estimates in southern Tibet from recalibrated Sr/Y and La/Yb trace element geochemical proxies. *GSA today*.

Taylor, M., & Yin, A. (2009). Active structures of the Himalayan-Tibetan orogen and their relationships to earthquake distribution, contemporary strain field, and Cenozoic volcanism. *Geosphere, 5*(3), 199-214.

Taylor, M., Yin, A., Ryerson, F. J., Kapp, P., & Ding, L. (2003). Conjugate strike-slip faulting along the Bangong-Nujiang suture zone accommodates coeval east-west extension and north-south shortening in the interior of the Tibetan Plateau. *Tectonics, 22*(4).

Wang, C., Li, X., Liu, Z., Li, Y., Jansa, L., Dai, J., & Wei, Y. (2012). Revision of the Cretaceous–Paleogene stratigraphic framework, facies architecture and provenance of the Xigaze forearc basin along the Yarlung Zangbo suture zone. *Gondwana Research, 22*(2), 415-433.

Wang, E., Kamp, P. J., Xu, G., Hodges, K. V., Meng, K., Chen, L., . . . Luo, H. (2015). Flexural bending of southern Tibet in a retro foreland setting. *Scientific Reports, 5*, 12076.

Wang, J.-G., Hu, X., Garzanti, E., An, W., & Liu, X.-C. (2017). The birth of the Xigaze forearc basin in southern Tibet. *Earth and Planetary Science Letters, 465*, 38-47.

Webb, A. A. G., Guo, H., Clift, P. D., Husson, L., Müller, T., Costantino, D., . . . Wang, Q. (2017). The Himalaya in 3D: Slab dynamics controlled mountain building and monsoon intensification. *Lithosphere, 9*(4), 637-651.

Williams, H., Turner, S., Kelley, S., & Harris, N. (2001). Age and composition of dikes in Southern Tibet: New constraints on the timing of east-west extension and its relationship to postcollisional volcanism. *Geology, 29*(4), 339-342.

Wolff, R., Hetzel, R., Dunkl, I., Xu, Q., Bröcker, M., & Anczkiewicz, A. A. (2019). High-Angle Normal Faulting at the Tangra Yumco Graben (Southern Tibet) since~ 15 Ma. *The Journal of Geology, 127*(1), 15-36.

Xu, Q., Zhao, J., Yuan, X., Liu, H., & Pei, S. (2015). Mapping crustal structure beneath southern Tibet: Seismic evidence for continental crustal underthrusting. *Gondwana Research, 27*(4), 1487-1493.

Yin, A. (2000). Mode of Cenozoic east-west extension in Tibet suggesting a common origin of rifts in Asia during the Indo-Asian collision. *Journal of Geophysical Research: Solid Earth, 105*(B9), 21745-21759.

Yin, A., & Harrison, T. M. (2000). Geologic evolution of the Himalayan-Tibetan orogen. *Annual review of earth and planetary sciences, 28*(1), 211-280.

Yin, A., Harrison, T. M., Murphy, M., Grove, M., Nie, S., Ryerson, F., . . . Zeng Le, C. (1999). Tertiary deformation history of southeastern and southwestern Tibet during the Indo-Asian collision. *Geological Society of America Bulletin, 111*(11), 1644-1664.

Yin, A., Harrison, T. M., Ryerson, F., Wenji, C., Kidd, W., & Copeland, P. (1994). Tertiary structural evolution of the Gangdese thrust system, southeastern Tibet. *Journal of Geophysical Research: Solid Earth, 99*(B9), 18175-18201.

Yin, A., & Taylor, M. H. (2011). Mechanics of V-shaped conjugate strike-slip faults and the corresponding continuum mode of continental deformation. *Bulletin, 123*(9-10), 1798-1821.

Zhang, P.-Z., Shen, Z., Wang, M., Gan, W., Bürgmann, R., Molnar, P., . . . Wu, J. (2004). Continuous deformation of the Tibetan Plateau from global positioning system data. *Geology, 32*(9), 809-812.

Zhang, R., Murphy, M. A., Lapen, T. J., Sanchez, V., & Heizler, M. (2011). Late Eocene crustal thickening followed by Early-Late Oligocene extension along the India-Asia suture zone: Evidence for cyclicity in the Himalayan orogen. *Geosphere, 7*(5), 1249-1268.

Zhao, W., Brown, L., Wu, Z., Klemperer, S., Shi, D., Mechie, J., . . . Makovsky, Y. (2008). Seismology across the northeastern edge of the Tibetan Plateau. *Eos, Transactions American Geophysical Union, 89*(48), 487-487.

Zhao, W., Mechie, J., Brown, L., Guo, J., Haines, S., Hearn, T., . . . Nelson, K. (2001). Crustal structure of central Tibet as derived from project INDEPTH wide-angle seismic data. *Geophysical Journal International, 145*(2), 486-498.

Zuza, A. V., Gavillot, Y., Haproff, P. J., & Wu, C. (2020). Kinematic evolution of a continental collision: Constraining the Himalayan-Tibetan orogen via bulk strain rates. *Tectonophysics, 797*, 228642.

REFERENCES CITED

Aitchison, J. C., Davis, A. M., & Luo, H. (2002). New constraints on the India–Asia collision: the lower Miocene Gangrinboche conglomerates, Yarlung Tsangpo suture zone, SE Tibet. *Journal of Asian Earth Sciences, 21*(3), 251-263.

Allegre, C. o., Courtillot, V., Tapponnier, P., Hirn, A., Mattauer, M., Coulon, C., . . . Marcoux, J. (1984). Structure and evolution of the Himalaya–Tibet orogenic belt. *Nature, 307*(5946), 17.

Alsdorf, D., Brown, L., Nelson, K. D., Makovsky, Y., Klemperer, S., & Zhao, W. (1998). Crustal deformation of the Lhasa terrane, Tibet plateau from Project INDEPTH deep seismic reflection profiles. *Tectonics, 17*(4), 501-519.

An, W., Hu, X., Garzanti, E., BouDagher-Fadel, M. K., Wang, J., & Sun, G. (2014). Xigaze forearc basin revisited (South Tibet): Provenance changes and origin of the Xigaze Ophiolite. *Bulletin, 126*(11-12), 1595-1613.

Armijo, R., Tapponnier, P., & Han, T. (1989). Late Cenozoic right-lateral strike-slip faulting in southern Tibet. *Journal of Geophysical Research: Solid Earth, 94*(B3), 2787-2838.

Armijo, R., Tapponnier, P., Mercier, J., & Han, T. L. (1986). Quaternary extension in southern Tibet: Field observations and tectonic implications. *Journal of Geophysical Research: Solid Earth, 91*(B14), 13803-13872.

Black, L. P., Kamo, S. L., Allen, C. M., Davis, D. W., Aleinikoff, J. N., Valley, J. W., . . . Williams, I. S. (2004). Improved 206Pb/238U microprobe geochronology by the monitoring of a trace-element-related matrix effect; SHRIMP, ID–TIMS, ELA–ICP–MS and oxygen isotope documentation for a series of zircon standards. *Chemical Geology, 205*(1-2), 115-140.

Brown, L., Zhao, W., Nelson, K., Hauck, M., Alsdorf, D., Ross, A., . . . Che, J. (1996). Bright spots, structure, and magmatism in southern Tibet from INDEPTH seismic reflection profiling. *science, 274*(5293), 1688-1690.

Chapman, J. B., & Ducea, M. N. (2019). The role of arc migration in Cordilleran orogenic cyclicity. *Geology, 47*(7), 627-631.

Chapman, J. B., Ducea, M. N., DeCelles, P. G., & Profeta, L. (2015). Tracking changes in crustal thickness during orogenic evolution with Sr/Y: An example from the North American Cordillera. *Geology, 43*(10), 919-922.

Chapman, J. B., Gehrels, G. E., Ducea, M. N., Giesler, N., & Pullen, A. (2016). A new method for estimating parent rock trace element concentrations from zircon. *Chemical Geology, 439*, 59-70.

Chapman, J. B., & Kapp, P. (2017). Tibetan magmatism database. *Geochemistry, Geophysics, Geosystems, 18*(11), 4229-4234.

Chiaradia, M. (2015). Crustal thickness control on Sr/Y signatures of recent arc magmas: an Earth scale perspective. *Scientific Reports, 5*, 8115.

Coleman, M., & Hodges, K. (1995). Evidence for Tibetan plateau uplift before 14 Myr ago from a new minimum age for east–west extension. *Nature, 374*(6517), 49.

Coulon, C., Maluski, H., Bollinger, C., & Wang, S. (1986). Mesozoic and Cenozoic volcanic rocks from central and southern Tibet: 39Ar-40Ar dating, petrological characteristics and geodynamical significance. *Earth and Planetary Science Letters, 79*(3-4), 281-302.

DeCelles, P. G., Kapp, P., Quade, J., & Gehrels, G. E. (2011). Oligocene–Miocene Kailas basin, southwestern Tibet: Record of postcollisional upper-plate extension in the Indus-Yarlung suture zone. *GSA Bulletin, 123*(7-8), 1337-1362.

DeCelles, P. G., Kapp, P., Gehrels, G. E., & Ding, L. (2014). Paleocene-Eocene foreland basin evolution in the Himalaya of southern Tibet and Nepal: Implications for the age of initial India-Asia collision. *Tectonics, 33*(5), 824-849.

Dewey, J. (1988). Extensional collapse of orogens. *Tectonics, 7*(6), 1123-1139.

Dürr, S. r. B. (1996). Provenance of Xigaze fore-arc basin clastic rocks (Cretaceous, south Tibet). *Geological Society of America Bulletin, 108*(6), 669-684.

Einsele, G., Liu, B., Dürr, S., Frisch, W., Liu, G., Luterbacher, H., . . . Wetzel, A. (1994). The Xigaze forearc basin: evolution and facies architecture (Cretaceous, Tibet). *Sedimentary Geology, 90*(1-2), 1-32.

England, P., & Houseman, G. (1989). Extension during continental convergence, with application to the Tibetan Plateau. *Journal of Geophysical Research: Solid Earth, 94*(B12), 17561-17579.

Gan, W., Zhang, P., Shen, Z. K., Niu, Z., Wang, M., Wan, Y., . . . Cheng, J. (2007). Present-day crustal motion within the Tibetan Plateau inferred from GPS measurements. *Journal of Geophysical Research: Solid Earth, 112*(B8).

Gansser, A. (1964). Geology of the Himalayas.

Garzione, C. N., Dettman, D. L., Quade, J., DeCelles, P. G., & Butler, R. F. (2000). High times on the Tibetan Plateau: Paleoelevation of the Thakkhola graben, Nepal. *Geology, 28*(4), 339-342.

Gehrels, G., & Pecha, M. (2014). Detrital zircon U-Pb geochronology and Hf isotope geochemistry of Paleozoic and Triassic passive margin strata of western North America. *Geosphere, 10*(1), 49-65.

Gehrels, G., Valencia, V., & Pullen, A. (2006). Detrital zircon geochronology by laser-ablation multicollector ICPMS at the Arizona LaserChron Center. *The Paleontological Society Papers, 12*, 67-76.

Gehrels, G. E., Valencia, V. A., & Ruiz, J. (2008). Enhanced precision, accuracy, efficiency, and spatial resolution of U-Pb ages by laser ablation–multicollector–inductively coupled plasma–mass spectrometry. *Geochemistry, Geophysics, Geosystems, 9*(3).

Guenthner, W. R., Reiners, P. W., Ketcham, R. A., Nasdala, L., & Giester, G. (2013). Helium diffusion in natural zircon: Radiation damage, anisotropy, and the interpretation of zircon (U-Th)/He thermochronology. *American Journal of Science, 313*(3), 145-198.

Harrison, T. M., Copeland, P., Kidd, W., & Lovera, O. M. (1995). Activation of the Nyainqentanghla shear zone: Implications for uplift of the southern Tibetan Plateau. *Tectonics, 14*(3), 658-676.

Harrison, T. M., Copeland, P., Kidd, W., & Yin, A. (1992). Raising tibet. *science, 255*(5052), 1663-1670.

Hawkesworth, C., & Kemp, A. (2006). Using hafnium and oxygen isotopes in zircons to unravel the record of crustal evolution. *Chemical Geology, 226*(3-4), 144-162.

Heim, A., & Gansser, A. (1975). *Central Himalaya: Geological observations of the Swiss expedition, 1936* (Vol. 73): Hindustan Publishing Corporation (India).

Hourigan, J. K., Reiners, P. W., & Brandon, M. T. (2005). U-Th zonation-dependent alpha-ejection in (U-Th)/He chronometry. *Geochimica et Cosmochimica Acta, 69*(13), 3349-3365.

Hu, X., Wang, J., BouDagher-Fadel, M., Garzanti, E., & An, W. (2016). New insights into the timing of the India–Asia collision from the Paleogene Quxia and Jialazi formations of the Xigaze forearc basin, South Tibet. *Gondwana Research, 32*, 76-92.

Kapp, J. L. D. A., Harrison, T. M., Kapp, P., Grove, M., Lovera, O. M., & Lin, D. (2005). Nyainqentanglha Shan: a window into the tectonic, thermal, and geochemical evolution of the Lhasa block, southern Tibet. *Journal of Geophysical Research: Solid Earth, 110*(B8).

Kapp, P., & DeCelles, P. G. (2019). Mesozoic–Cenozoic geological evolution of the Himalayan-Tibetan orogen and working tectonic hypotheses. *American Journal of Science, 319*(3), 159-254.

Kapp, P., & Guynn, J. H. (2004). Indian punch rifts Tibet. *Geology, 32*(11), 993-996.

Kapp, P., Taylor, M., Stockli, D., & Ding, L. (2008). Development of active low-angle normal fault systems during orogenic collapse: Insight from Tibet. *Geology, 36*(1), 7-10.

Karplus, M., Zhao, W., Klemperer, S., Wu, Z., Mechie, J., Shi, D., . . . Chen, C. (2011). Injection of Tibetan crust beneath the south Qaidam Basin: Evidence from INDEPTH IV wide-angle seismic data. *Journal of Geophysical Research: Solid Earth, 116*(B7).

Ketcham, R. A. (2005). Forward and inverse modeling of low-temperature thermochronometry data. *Reviews in Mineralogy and Geochemistry, 58*(1), 275-314.

Ketcham, R. A., Gautheron, C., & Tassan-Got, L. (2011). Accounting for long alpha-particle stopping distances in (U–Th–Sm)/He geochronology: refinement of the baseline case. *Geochimica et Cosmochimica Acta, 75*(24), 7779-7791.

Kind, R., Yuan, X., Saul, J., Nelson, D., Sobolev, S., Mechie, J., . . . Achauer, U. (2002). Seismic images of crust and upper mantle beneath Tibet: evidence for Eurasian plate subduction. *science, 298*(5596), 1219-1221.

Laskowski, A. K. (2016). *Tectonic evolution of the Yarlung suture zone, Lopu Range and Lazi Regions, central southern Tibet*: The University of Arizona.

Laskowski, A. K., Kapp, P., & Cai, F. (2018). Gangdese culmination model: Oligocene–Miocene duplexing along the India-Asia suture zone, Lazi region, southern Tibet. *GSA Bulletin, 130*(7-8), 1355-1376.

Laskowski, A. K., Kapp, P., Ding, L., Campbell, C., & Liu, X. (2017). Tectonic evolution of the Yarlung suture zone, Lopu Range region, southern Tibet. *Tectonics, 36*(1), 108-136.

Leary, R., Orme, D. A., Laskowski, A. K., DeCelles, P. G., Kapp, P., Carrapa, B., & Dettinger, M. (2016). Along-strike diachroneity in deposition of the Kailas Formation in central southern Tibet: Implications for Indian slab dynamics. *Geosphere, 12*(4), 1198-1223.

Lee, H., Chung, S., Wang, Y., Zhu, D., Yang, J., Song, B., . . . Wu, F. (2007). Age, petrogenesis and geological significance ofthe Linzizong volcanic successions in the Linzhou basin, southern Tibet: Evidence from zircon U-Pb dates and Hf isotopes.

Lee, H.-Y., Chung, S.-L., Lo, C.-H., Ji, J., Lee, T.-Y., Qian, Q., & Zhang, Q. (2009). Eocene Neotethyan slab breakoff in southern Tibet inferred from the Linzizong volcanic record. *Tectonophysics, 477*(1-2), 20-35.

Ludwig, K., & Mundil, R. (2002). *Extracting reliable U-Pb ages and errors from complex populations of zircons from Phanerozoic tuffs.* Paper presented at the Geochimica et Cosmochimica Acta.

Ludwig, K. R. (2003). Isoplot 3.00: A geochronological toolkit for Microsoft Excel. *Berkeley Geochronology Center Special Publication, 4*, 70.

Maluski, H., Proust, F., & Xiao, X. (1982). 39 Ar/40 Ar dating of the trans-Himalayan calc-alkaline magmatism of southern Tibet. *Nature, 298*(5870), 152-154.

Mechie, J., & Kind, R. (2013). A model of the crust and mantle structure down to 700 km depth beneath the Lhasa to Golmud transect across the Tibetan plateau as derived from seismological data. *Tectonophysics, 606*, 187-197.

Mechie, J., Zhao, W., Karplus, M., Wu, Z., Meissner, R., Shi, D., . . . Xue, G. (2012). Crustal shear (S) velocity and Poisson's ratio structure along the INDEPTH IV profile in northeast Tibet as derived from wide-angle seismic data. *Geophysical Journal International, 191*(2), 369-384.

Molnar, P., & Tapponnier, P. (1975). Cenozoic tectonics of Asia: effects of a continental collision. *science, 189*(4201), 419-426.

Molnar, P., & Tapponnier, P. (1978). Active tectonics of Tibet. *Journal of Geophysical Research: Solid Earth, 83*(B11), 5361-5375.

Murphy, M., Sanchez, V., & Taylor, M. (2010). Syncollisional extension along the India–Asia suture zone, south-central Tibet: Implications for crustal deformation of Tibet. *Earth and Planetary Science Letters, 290*(3-4), 233-243.

Murphy, M., & Yin, A. (2003). Structural evolution and sequence of thrusting in the Tethyan fold-thrust belt and Indus-Yalu suture zone, southwest Tibet. *Geological Society of America Bulletin, 115*(1), 21-34.

Nábělek, J., Hetényi, G., Vergne, J., Sapkota, S., Kafle, B., Jiang, M., . . . Huang, B.-S. (2009). Underplating in the Himalaya-Tibet collision zone revealed by the Hi-CLIMB experiment. *science, 325*(5946), 1371-1374.

Orme, D. A. (2019). Burial and exhumation history of the Xigaze forearc basin, Yarlung suture zone, Tibet. *Geoscience Frontiers, 10*(3), 895-908.

Orme, D. A., Carrapa, B., & Kapp, P. (2015). Sedimentology, provenance and geochronology of the upper Cretaceous–lower Eocene western Xigaze forearc basin, southern Tibet. *Basin Research, 27*(4), 387-411.

Orme, D. A., & Laskowski, A. K. (2016). Basin analysis of the Albian–Santonian Xigaze forearc, Lazi region, south-central Tibet. *Journal of Sedimentary Research, 86*(8), 894-913.

Paces, J. B., & Miller Jr, J. D. (1993). Precise U-Pb ages of Duluth complex and related mafic intrusions, northeastern Minnesota: Geochronological insights to physical, petrogenetic, paleomagnetic, and tectonomagmatic processes associated with the 1.1 Ga midcontinent rift system. *Journal of Geophysical Research: Solid Earth, 98*(B8), 13997-14013.

Pan, G., Ding, J., Yao, D., & Wang, L. (2004). Guidebook of 1: 1,500,000 geologic map of the Qinghai–Xizang (Tibet) plateau and adjacent areas. *Chengdu, China: Chengdu Cartographic Publishing House, 48*.

Profeta, L., Ducea, M. N., Chapman, J. B., Paterson, S. R., Gonzales, S. M. H., Kirsch, M., . . . DeCelles, P. G. (2015). Quantifying crustal thickness over time in magmatic arcs. *Scientific Reports, 5*, 17786.

Pullen, A., Ibáñez-Mejia, M., Gehrels, G. E., Giesler, D., & Pecha, M. (2018). Optimization of a laser ablation-single collector-inductively coupled plasma-mass spectrometer (Thermo Element 2) for accurate, precise, and efficient zircon U-Th-Pb geochronology. *Geochemistry, Geophysics, Geosystems, 19*(10), 3689-3705.

Reiners, P. W. (2005). Zircon (U-Th)/He thermochronometry. *Reviews in Mineralogy and Geochemistry, 58*(1), 151-179.

Sanchez, V., Murphy, M., Robinson, A., Lapen, T., & Heizler, M. (2013). Tectonic evolution of the India–Asia suture zone since Middle Eocene time, Lopukangri area, south-central Tibet. *Journal of Asian Earth Sciences, 62*, 205-220.

Schärer, U., Xu, R.-H., & Allègre, C. J. (1984). UPb geochronology of Gangdese (Transhimalaya) plutonism in the Lhasa-Xigaze region, Tibet. *Earth and Planetary Science Letters, 69*(2), 311-320.

Schmitz, M. D., Bowring, S. A., & Ireland, T. R. (2003). Evaluation of Duluth Complex anorthositic series (AS3) zircon as a U-Pb geochronological standard: New high-precision isotope dilution thermal ionization mass spectrometry results. *Geochimica et Cosmochimica Acta, 67*(19), 3665-3672.

Searle, M., Windley, B., Coward, M., Cooper, D., Rex, A., Rex, D., . . . Thakur, V. (1987). The closing of Tethys and the tectonics of the Himalaya. *Geological Society of America Bulletin, 98*(6), 678-701.

Shen, T., Wang, G., Bernet, M., Replumaz, A., Ai, K., Song, B., . . . Zhang, P. (2019). Long-term exhumation history of the Gangdese magmatic arc: Implications for the evolution of the Kailas Basin, western Tibet. *Geological Journal*.

Styron, R., Taylor, M., & Sundell, K. (2015). Accelerated extension of Tibet linked to the northward underthrusting of Indian crust. *Nature Geoscience, 8*(2), 131.

Styron, R. H., Taylor, M. H., Sundell, K. E., Stockli, D. F., Oalmann, J. A., Möller, A., . . . Ding, L. (2013). Miocene initiation and acceleration of extension in the South Lunggar rift, western Tibet: Evolution of an active detachment system from structural mapping and (U-Th)/He thermochronology. *Tectonics, 32*(4), 880-907.

Sundell, K. E., Taylor, M. H., Styron, R. H., Stockli, D. F., Kapp, P., Hager, C., . . . Ding, L. (2013). Evidence for constriction and Pliocene acceleration of east-west extension in the North Lunggar rift region of west central Tibet. *Tectonics, 32*(5), 1454-1479.

Sundell, K., Laskowski, A. K., Kapp, P. A., & Ducea, M. N. (2020, December). Jurassic to Neogene quantitative crustal thickness estimates in southern Tibet from recalibrated Sr/Y and La/Yb trace element geochemical proxies. In *AGU Fall Meeting* 2020. AGU.

Sundell, K., Laskowski, A. K., Kapp, P. A., & Ducea, M. N. (2021). Jurassic to Neogene quantitative crustal thickness estimates in southern Tibet from recalibrated Sr/Y and La/Yb trace element geochemical proxies. *GSA today*.

Taylor, M., & Yin, A. (2009). Active structures of the Himalayan-Tibetan orogen and their relationships to earthquake distribution, contemporary strain field, and Cenozoic volcanism. *Geosphere, 5*(3), 199-214.

Taylor, M., Yin, A., Ryerson, F. J., Kapp, P., & Ding, L. (2003). Conjugate strike-slip faulting along the Bangong-Nujiang suture zone accommodates coeval east-west extension and north-south shortening in the interior of the Tibetan Plateau. *Tectonics, 22*(4).

Wang, C., Li, X., Liu, Z., Li, Y., Jansa, L., Dai, J., & Wei, Y. (2012). Revision of the Cretaceous–Paleogene stratigraphic framework, facies architecture and provenance of the Xigaze forearc basin along the Yarlung Zangbo suture zone. *Gondwana Research, 22*(2), 415-433.

Wang, E., Kamp, P. J., Xu, G., Hodges, K. V., Meng, K., Chen, L., . . . Luo, H. (2015). Flexural bending of southern Tibet in a retro foreland setting. *Scientific Reports, 5*, 12076.

Wang, J.-G., Hu, X., Garzanti, E., An, W., & Liu, X.-C. (2017). The birth of the Xigaze forearc basin in southern Tibet. *Earth and Planetary Science Letters, 465*, 38-47.

Webb, A. A. G., Guo, H., Clift, P. D., Husson, L., Müller, T., Costantino, D., . . . Wang, Q. (2017). The Himalaya in 3D: Slab dynamics controlled mountain building and monsoon intensification. *Lithosphere, 9*(4), 637-651.

Williams, H., Turner, S., Kelley, S., & Harris, N. (2001). Age and composition of dikes in Southern Tibet: New constraints on the timing of east-west extension and its relationship to postcollisional volcanism. *Geology, 29*(4), 339-342.

Wolff, R., Hetzel, R., Dunkl, I., Xu, Q., Bröcker, M., & Anczkiewicz, A. A. (2019). High-Angle Normal Faulting at the Tangra Yumco Graben (Southern Tibet) since~ 15 Ma. *The Journal of Geology, 127*(1), 15-36.

Xu, Q., Zhao, J., Yuan, X., Liu, H., & Pei, S. (2015). Mapping crustal structure beneath southern Tibet: Seismic evidence for continental crustal underthrusting. *Gondwana Research, 27*(4), 1487-1493.

Yin, A. (2000). Mode of Cenozoic east-west extension in Tibet suggesting a common origin of rifts in Asia during the Indo-Asian collision. *Journal of Geophysical Research: Solid Earth, 105*(B9), 21745-21759.

Yin, A., & Harrison, T. M. (2000). Geologic evolution of the Himalayan-Tibetan orogen. *Annual review of earth and planetary sciences, 28*(1), 211-280.

Yin, A., Harrison, T. M., Murphy, M., Grove, M., Nie, S., Ryerson, F., . . . Zeng Le, C. (1999). Tertiary deformation history of southeastern and southwestern Tibet during the Indo-Asian collision. *Geological Society of America Bulletin, 111*(11), 1644-1664.

Yin, A., Harrison, T. M., Ryerson, F., Wenji, C., Kidd, W., & Copeland, P. (1994). Tertiary structural evolution of the Gangdese thrust system, southeastern Tibet. *Journal of Geophysical Research: Solid Earth, 99*(B9), 18175-18201.

Yin, A., & Taylor, M. H. (2011). Mechanics of V-shaped conjugate strike-slip faults and the corresponding continuum mode of continental deformation. *Bulletin, 123*(9-10), 1798-1821.

Zhang, P.-Z., Shen, Z., Wang, M., Gan, W., Bürgmann, R., Molnar, P., . . . Wu, J. (2004). Continuous deformation of the Tibetan Plateau from global positioning system data. *Geology, 32*(9), 809-812.

Zhang, R., Murphy, M. A., Lapen, T. J., Sanchez, V., & Heizler, M. (2011). Late Eocene crustal thickening followed by Early-Late Oligocene extension along the India-Asia suture zone: Evidence for cyclicity in the Himalayan orogen. *Geosphere, 7*(5), 1249-1268.

Zhao, W., Brown, L., Wu, Z., Klemperer, S., Shi, D., Mechie, J., . . . Makovsky, Y. (2008). Seismology across the northeastern edge of the Tibetan Plateau. *Eos, Transactions American Geophysical Union, 89*(48), 487-487.

Zhao, W., Mechie, J., Brown, L., Guo, J., Haines, S., Hearn, T., . . . Nelson, K. (2001). Crustal structure of central Tibet as derived from project INDEPTH wide-angle seismic data. *Geophysical Journal International, 145*(2), 486-498.

Zuza, A. V., Gavillot, Y., Haproff, P. J., & Wu, C. (2020). Kinematic evolution of a continental collision: Constraining the Himalayan-Tibetan orogen via bulk strain rates. *Tectonophysics, 797*, 228642.

APPENDICES

APPENDIX A

U-PB GEOCHRONOLOGY DATA

Analysis	U	206Pb	U/Th	206Pb*	±	207Pb*	±	206Pb*	±	error	206Pb*	±	207Pb*	±	206Pb*	±	Best age	±	Conc	Used for AVG
	(ppm)	204Pb		207Pb*	(%)	235U*	(%)	238U	(%)	corr.	238U*	(Ma)	235U	(Ma)	207Pb*	(Ma)	(Ma)	(Ma)	(%)	
-7618DA1 Spot 1	123	2188	0.9	23.5109	2.9	0.0485	3.3	0.0083	1.6	0.49	53.1	0.9	48.1	1.6	NA	NA	53.1	0.9	110.5	AVG
-7618DA1 Spot 2	305	55168	0.6	20.1370	1.5	0.0581	2.1	0.0085	1.5	0.72	54.5	0.8	57.3	1.2	178.1	34.6	54.5	0.8	95.0	AVG
-7618DA1 Spot 3	171	2091	0.9	17.3033	5.6	0.0692	5.7	0.0087	1.3	0.22	55.8	0.7	67.9	3.8	520.9	122.4	55.8	0.7	82.1	AVG
-7618DA1 Spot 4	121	2400	0.9	23.1447	2.9	0.0499	3.2	0.0084	1.4	0.44	53.8	0.8	49.4	1.6	NA	NA	53.8	0.8	108.8	AVG
-7618DA1 Spot 5	371	11567	0.6	20.9662	1.7	0.0557	2.0	0.0085	1.0	0.50	54.4	0.5	55.0	1.0	83.2	40.3	54.4	0.5	98.8	AVG
-7618DA1 Spot 6	213	3376	0.8	23.2016	5.5	0.0505	5.6	0.0085	1.0	0.18	54.6	0.6	50.1	2.7	NA	NA	54.6	0.6	109.1	AVG
-7618DA1 Spot 7	166	8323	0.9	21.2078	2.4	0.0544	2.6	0.0084	1.1	0.41	53.8	0.6	53.8	1.4	55.9	56.5	53.8	0.6	99.9	AVG
-7618DA1 Spot 8	175	4776	0.8	22.6382	2.1	0.0518	2.5	0.0085	1.4	0.55	54.6	0.7	51.2	1.3	NA	NA	54.6	0.7	106.5	AVG
-7618DA1 Spot 9	274	7118	0.7	21.7127	1.8	0.0531	2.2	0.0084	1.2	0.57	53.7	0.7	52.5	1.1	NA	NA	53.7	0.7	102.2	AVG
-7618DA1 Spot 10	191	3066	0.8	22.7476	2.6	0.0517	2.9	0.0085	1.2	0.41	54.8	0.6	51.2	1.4	NA	NA	54.8	0.6	107.0	AVG
-7618DA1 Spot 11	302	3982	0.7	22.3572	1.7	0.0528	2.3	0.0086	1.5	0.67	55.0	0.8	52.3	1.2	NA	NA	55.0	0.8	105.2	AVG
-7618DA1 Spot 12	204	51127	0.8	21.1282	2.3	0.0555	2.6	0.0085	1.2	0.46	54.6	0.7	54.8	1.4	64.9	54.5	54.6	0.7	99.6	AVG
-7618DA1 Spot 13	221	3275	0.8	22.2195	3.4	0.0527	3.6	0.0085	1.2	0.32	54.6	0.6	52.2	1.8	NA	NA	54.6	0.6	104.6	AVG
-7618DA1 Spot 14	175	5734	0.9	21.5260	2.8	0.0538	3.0	0.0084	1.2	0.40	53.9	0.7	53.2	1.6	20.3	66.6	53.9	0.7	101.4	AVG
-7618DA1 Spot 15	142	1248	0.9	26.6633	4.3	0.0434	4.4	0.0084	1.1	0.26	54.0	0.6	43.2	1.9	NA	NA	54.0	0.6	125.0	AVG
-7618DA1 Spot 16	133	1178	0.8	13.6704	3.6	0.0867	3.7	0.0086	1.1	0.28	55.2	0.6	84.5	3.0	1017.2	72.6	55.2	0.6	65.4	AVG
-7618DA1 Spot 18	254	4247	0.7	22.0065	2.0	0.0535	2.6	0.0085	1.6	0.60	54.8	0.8	52.9	1.3	NA	NA	54.8	0.8	103.6	AVG
-7618DA1 Spot 19	296	1254987	0.7	20.3519	1.2	0.0584	1.7	0.0086	1.3	0.75	55.3	0.7	57.6	1.0	153.3	27.2	55.3	0.7	96.0	AVG
-7618DA1 Spot 20	278	4328	0.8	22.0198	2.3	0.0525	2.6	0.0084	1.3	0.49	53.8	0.7	51.9	1.3	NA	NA	53.8	0.7	103.6	AVG
-7618DA1 Spot 21	317	887454	0.6	20.5453	1.8	0.0573	2.4	0.0085	1.5	0.64	54.9	0.8	56.6	1.3	131.1	43.1	54.9	0.8	96.9	AVG
-7618DA1 Spot 22	344	2362	0.7	23.7325	1.7	0.0493	2.1	0.0085	1.2	0.58	54.5	0.7	48.8	1.0	NA	NA	54.5	0.7	111.5	AVG
-7618DA1 Spot 23	316	7706	0.8	21.8149	1.5	0.0541	2.0	0.0086	1.3	0.64	55.0	0.7	53.5	1.0	NA	NA	55.0	0.7	102.7	AVG
-7618DA1 Spot 24	173	5721	0.9	21.4353	2.5	0.0534	2.9	0.0083	1.3	0.45	53.4	0.7	52.9	1.5	30.4	61.0	53.4	0.7	100.9	AVG
-7618DA1 Spot 25	229	10330	0.9	21.0503	1.9	0.0554	2.3	0.0085	1.2	0.53	54.3	0.7	54.8	1.2	73.7	46.0	54.3	0.7	99.2	AVG
-7618DA1 Spot 26	304	6307	0.8	21.8801	3.0	0.0537	3.3	0.0085	1.5	0.44	54.7	0.8	53.1	1.7	NA	NA	54.7	0.8	103.0	AVG
-7618DA1 Spot 27	257	3478	0.7	20.2020	5.1	0.0585	5.4	0.0086	1.7	0.31	55.0	0.9	57.7	3.0	170.5	118.9	55.0	0.9	95.3	AVG
-7618DA1 Spot 28	166	5848	0.9	21.8939	2.1	0.0525	2.5	0.0083	1.4	0.56	53.5	0.7	51.9	1.3	NA	NA	53.5	0.7	103.0	AVG
-7618DA1 Spot 29	230	7932	1.0	21.7619	1.9	0.0525	2.5	0.0083	1.6	0.64	53.2	0.8	52.0	1.2	NA	NA	53.2	0.8	102.4	AVG
-7618DA1 Spot 30	282	52285	0.9	20.5874	1.4	0.0584	1.8	0.0087	1.2	0.67	56.0	0.7	57.6	1.0	126.3	32.5	56.0	0.7	97.2	AVG
-7618DA1 Spot 31	202	4004	0.7	22.7485	2.0	0.0511	2.4	0.0084	1.4	0.59	54.2	0.8	50.6	1.2	NA	NA	54.2	0.8	107.0	AVG
-7618DA1 Spot 32	269	9952	0.8	21.4519	2.0	0.0548	2.4	0.0085	1.2	0.53	54.8	0.7	54.2	1.2	28.6	47.9	54.8	0.7	101.1	AVG
-7618DA1 Spot 34	227	6651	1.0	21.2197	2.0	0.0562	2.3	0.0087	1.3	0.54	55.6	0.7	55.6	1.3	54.6	47.1	55.6	0.7	100.0	AVG
-7618DA1 Spot 35	266	12255	0.6	21.7408	1.8	0.0533	2.0	0.0084	1.0	0.48	54.0	0.5	52.8	1.0	NA	NA	54.0	0.5	102.4	AVG
-7618DA1 Spot 33	154	1521	0.9	25.7171	7.1	0.0446	7.2	0.0083	1.4	0.19	53.4	0.7	44.3	3.1	NA	NA	53.4	0.7	120.6	AVG

Analysis	**U**	**206Pb**	**U/Th**	**206Pb***	**±**	**207Pb***	**±**	**206Pb***	**±**	**error**	**206Pb***	**±**	**207Pb***	**±**	**206Pb***	**±**	**Best age**	**±**	**Conc**	**Used for AVG**
	(ppm)	**204Pb**		**207Pb***	**(%)**	**235U***	**(%)**	**238U**	**(%)**	**corr.**	**238U***	**(Ma)**	**235U**	**(Ma)**	**207Pb***	**(Ma)**	**(Ma)**	**(Ma)**	**(%)**	
-7718DA1 Spot 51	244	46979	2.0	20.8270	1.9	0.0696	2.5	0.0105	1.7	0.68	67.4	1.2	68.3	1.7	99.0	43.9	67.4	1.2	98.7	AVG
-7718DA1 Spot 59	479	15352	1.6	20.9471	1.3	0.0697	1.8	0.0106	1.1	0.65	67.9	0.8	68.4	1.2	85.4	32.0	67.9	0.8	99.3	AVG
-7718DA1 Spot 63	426	11420	1.1	19.5229	1.6	0.0748	2.1	0.0106	1.3	0.61	67.9	0.8	73.2	1.5	249.8	38.0	67.9	0.8	92.8	AVG
-7718DA1 Spot 69	190	5759	1.7	20.6614	2.3	0.0710	2.5	0.0106	0.8	0.34	68.2	0.6	69.6	1.7	117.8	54.7	68.2	0.6	98.0	AVG
-7718DA1 Spot 38	265	17848	1.4	18.1527	1.7	0.0810	2.1	0.0107	1.3	0.62	68.4	0.9	79.0	1.6	414.8	37.1	68.4	0.9	86.5	AVG
-7718DA1 Spot 65	355	17816	2.3	16.2362	4.8	0.0906	5.0	0.0107	1.4	0.28	68.5	1.0	88.1	4.2	659.0	102.2	68.5	1.0	77.7	AVG
-7718DA1 Spot 45	645	6927	2.5	21.5877	1.3	0.0682	1.6	0.0107	1.0	0.61	68.5	0.7	67.0	1.0	13.4	30.5	68.5	0.7	102.3	AVG
-7718DA1 Spot 54	534	41174	1.8	20.3450	1.2	0.0724	1.8	0.0107	1.3	0.75	68.5	0.9	71.0	1.2	154.1	28.1	68.5	0.9	96.6	AVG
-7718DA1 Spot 46	712	23232	1.1	20.8155	1.3	0.0709	1.8	0.0107	1.2	0.69	68.7	0.8	69.5	1.2	100.3	31.0	68.7	0.8	98.7	AVG
-7718DA1 Spot 52	811	42740	1.5	18.6327	1.2	0.0795	1.7	0.0108	1.1	0.67	69.0	0.8	77.7	1.3	356.2	28.0	69.0	0.8	88.7	AVG
-7718DA1 Spot 66	147	3073	1.7	22.3851	4.6	0.0663	4.8	0.0108	1.5	0.32	69.0	1.1	65.2	3.0	NA	NA	69.0	1.1	105.9	AVG
-7718DA1 Spot 43	658	48419	1.7	19.3340	1.2	0.0768	1.7	0.0108	1.2	0.69	69.1	0.8	75.1	1.2	272.1	28.4	69.1	0.8	91.9	AVG
-7718DA1 Spot 44	652	113940	2.2	20.7108	1.1	0.0717	1.6	0.0108	1.1	0.71	69.1	0.8	70.3	1.1	112.2	26.1	69.1	0.8	98.3	AVG
-7718DA1 Spot 53	897	24187	1.5	20.2619	0.7	0.0733	1.4	0.0108	1.2	0.85	69.1	0.8	71.9	1.0	163.6	16.8	69.1	0.8	96.2	AVG
-7718DA1 Spot 62	410	97774	0.9	18.8671	1.8	0.0789	2.1	0.0108	1.2	0.55	69.3	0.8	77.1	1.6	327.9	40.5	69.3	0.8	89.8	AVG
-7718DA1 Spot 36	208	29083	3.4	20.5119	1.8	0.0729	2.1	0.0109	0.9	0.45	69.6	0.6	71.5	1.4	134.9	43.1	69.6	0.6	97.4	AVG
-7718DA1 Spot 47	932	110925	1.3	20.7091	1.0	0.0723	1.5	0.0109	1.1	0.73	69.6	0.7	70.9	1.0	112.4	23.8	69.6	0.7	98.3	AVG
-7718DA1 Spot 37	801	21059	1.5	20.7156	1.3	0.0724	1.7	0.0109	1.2	0.68	69.8	0.8	71.0	1.2	111.7	29.9	69.8	0.8	98.3	AVG
-7718DA1 Spot 50	281	4942	2.6	21.6344	3.0	0.0694	3.1	0.0109	1.0	0.31	69.9	0.7	68.1	2.1	8.2	71.6	69.9	0.7	102.5	AVG
-7718DA1 Spot 40	1169	43562	1.3	20.9843	1.2	0.0716	1.6	0.0109	1.1	0.69	69.9	0.8	70.2	1.1	81.1	28.0	69.9	0.8	99.5	AVG
-7718DA1 Spot 68	282	5952	2.3	21.2573	2.0	0.0707	2.4	0.0109	1.2	0.51	70.0	0.8	69.4	1.6	50.3	48.8	70.0	0.8	100.8	AVG
-7718DA1 Spot 67	631	8777	1.8	21.0501	2.1	0.0716	2.4	0.0109	1.2	0.51	70.1	0.9	70.2	1.6	73.7	49.6	70.1	0.9	99.9	AVG
-7718DA1 Spot 70	1030	17735	2.1	20.3322	0.9	0.0746	1.4	0.0110	1.0	0.73	70.5	0.7	73.0	1.0	155.5	22.2	70.5	0.7	96.6	AVG
-7718DA1 Spot 48	353	152040	1.6	21.0056	1.5	0.0722	1.8	0.0110	1.0	0.58	70.6	0.7	70.8	1.2	78.7	34.7	70.6	0.7	99.7	AVG
-7718DA1 Spot 49	581	8272	0.8	19.1648	1.5	0.0792	1.9	0.0110	1.2	0.63	70.6	0.8	77.4	1.4	292.3	33.1	70.6	0.8	91.2	AVG
-7718DA1 Spot 55	183	6736	1.0	21.2429	1.7	0.0716	2.0	0.0110	1.1	0.52	70.7	0.7	70.2	1.4	52.0	41.2	70.7	0.7	100.8	AVG
-7718DA1 Spot 64	1622	258495	1.4	20.2869	0.9	0.0750	1.2	0.0110	0.8	0.67	70.8	0.6	73.4	0.9	160.8	21.6	70.8	0.6	96.4	AVG
-7718DA1 Spot 60	1445	19910	1.6	21.2029	1.0	0.0725	1.3	0.0112	0.9	0.66	71.5	0.6	71.1	0.9	56.5	23.4	71.5	0.6	100.6	
-7718DA1 Spot 56	718	12783	2.3	19.9484	1.3	0.0772	1.8	0.0112	1.2	0.68	71.7	0.9	75.5	1.3	200.0	30.1	71.7	0.9	94.9	
-7718DA1 Spot 57	149	2348	0.5	18.8546	6.4	0.0823	6.5	0.0113	1.1	0.18	72.1	0.8	80.3	5.0	329.4	144.7	72.1	0.8	89.9	
-7718DA1 Spot 58	1723	41998	1.6	20.8838	0.7	0.0743	1.2	0.0113	1.0	0.83	72.2	0.7	72.8	0.8	92.5	15.7	72.2	0.7	99.2	
-7718DA1 Spot 42	1626	25990	1.7	20.9712	1.0	0.0745	1.6	0.0113	1.3	0.80	72.6	0.9	72.9	1.1	82.6	22.6	72.6	0.9	99.6	
-7718DA1 Spot 41	646	71093	1.2	20.3532	1.3	0.0769	1.7	0.0114	1.0	0.62	72.8	0.8	75.2	1.2	153.1	31.0	72.8	0.8	96.8	
~~-7718DA1 Spot 61~~	~~658~~	~~1230~~	~~1.9~~	~~10.5791~~	~~12.4~~	~~0.1501~~	~~12.6~~	~~0.0115~~	~~2.2~~	~~0.17~~	~~73.9~~	~~1.6~~	~~142.0~~	~~16.7~~	~~1517.8~~	~~235.3~~	~~73.9~~	~~1.6~~	~~52.0~~	*DISCORD

Analysis	U	206Pb	U/Th	206Pb*	±	207Pb*	±	206Pb*	±	error	206Pb*	±	207Pb*	±	206Pb*	±	Best age	±	Conc	Used for AVG
	(ppm)	204Pb		207Pb*	(%)	235U*	(%)	238U	(%)	corr.	238U*	(Ma)	235U	(Ma)	207Pb*	(Ma)	(Ma)	(Ma)	(%)	
-7718DA2 Spot 19	99	1718	1.1	23.6432	2.5	0.0539	2.8	0.0093	1.3	0.47	59.4	0.8	53.3	1.4	NA	NA	59.4	0.8	111.3	AVG
-7718DA2 Spot 23	124	2054	1.5	23.4776	4.7	0.0545	4.9	0.0093	1.5	0.30	59.5	0.9	53.8	2.6	NA	NA	59.5	0.9	110.6	AVG
-7718DA2 Spot 5	302	14234	1.0	21.2428	1.6	0.0603	2.2	0.0093	1.6	0.71	59.6	0.9	59.4	1.3	52.0	37.4	59.6	0.9	100.3	AVG
-7718DA2 Spot 21	225	10962	1.8	21.6653	1.8	0.0592	2.3	0.0093	1.5	0.65	59.8	0.9	58.4	1.3	4.7	42.7	59.8	0.9	102.3	AVG
-7718DA2 Spot 24	979	12298	1.7	20.3329	1.8	0.0634	2.2	0.0094	1.3	0.59	60.1	0.8	62.5	1.3	155.5	42.0	60.1	0.8	96.2	AVG
-7718DA2 Spot 18	355	3531	1.4	19.1349	2.3	0.0675	2.6	0.0094	1.2	0.48	60.1	0.7	66.3	1.7	295.9	52.2	60.1	0.7	90.7	AVG
-7718DA2 Spot 11	296	11208	1.9	20.7658	2.1	0.0627	2.6	0.0094	1.6	0.62	60.6	1.0	61.7	1.6	105.9	48.9	60.6	1.0	98.2	AVG
-7718DA2 Spot 1	57	11622	1.1	19.5571	4.1	0.0668	4.5	0.0095	1.7	0.39	60.8	1.1	65.7	2.8	245.8	94.7	60.8	1.1	92.6	AVG
-7718DA2 Spot 16	390	37876	1.7	21.1918	1.4	0.0622	2.1	0.0096	1.5	0.74	61.3	0.9	61.3	1.2	57.7	33.8	61.3	0.9	100.1	AVG
-7718DA2 Spot 28	116	2268	1.8	19.9365	6.8	0.0661	7.0	0.0096	1.6	0.23	61.4	1.0	65.0	4.4	201.4	157.6	61.4	1.0	94.4	AVG
-7718DA2 Spot 8	1540	12688	2.9	20.6212	1.2	0.0639	1.7	0.0096	1.1	0.66	61.4	0.7	62.9	1.0	122.4	29.4	61.4	0.7	97.5	AVG
-7718DA2 Spot 30	301	5590	2.1	20.9486	3.0	0.0633	3.4	0.0096	1.6	0.46	61.7	1.0	62.3	2.1	85.2	71.7	61.7	1.0	99.0	AVG
-7718DA2 Spot 31	1391	46698	2.4	20.7164	1.1	0.0640	1.5	0.0096	1.1	0.71	61.7	0.7	63.0	0.9	111.5	25.2	61.7	0.7	98.0	AVG
-7718DA2 Spot 32	1610	59092	2.2	20.5278	1.5	0.0649	2.0	0.0097	1.4	0.69	62.0	0.9	63.8	1.2	133.1	34.5	62.0	0.9	97.1	AVG
-7718DA2 Spot 12	1344	21375	1.8	20.5747	1.2	0.0648	1.7	0.0097	1.2	0.71	62.0	0.8	63.7	1.1	127.7	28.3	62.0	0.8	97.3	AVG
-7718DA2 Spot 20	86	5437	1.1	21.0394	3.4	0.0637	3.7	0.0097	1.5	0.39	62.4	0.9	62.7	2.3	74.9	81.6	62.4	0.9	99.5	AVG
-7718DA2 Spot 17	987	25369	2.8	19.8582	1.1	0.0676	1.6	0.0097	1.1	0.71	62.5	0.7	66.4	1.0	210.5	25.7	62.5	0.7	94.1	AVG
-7718DA2 Spot 33	118	3167	1.0	21.0275	5.6	0.0641	5.8	0.0098	1.4	0.24	62.8	0.9	63.1	3.5	76.2	133.0	62.8	0.9	99.5	AVG
-7718DA2 Spot 2	872	37679	2.2	20.2806	1.4	0.0665	1.9	0.0098	1.3	0.68	62.8	0.8	65.4	1.2	161.5	33.1	62.8	0.8	96.0	AVG
-7718DA2 Spot 34	145	6116	1.6	20.9718	2.7	0.0645	3.1	0.0098	1.6	0.50	63.0	1.0	63.5	1.9	82.5	64.2	63.0	1.0	99.2	AVG
-7718DA2 Spot 22	1775	44132	2.9	20.9522	1.2	0.0647	1.6	0.0098	1.1	0.67	63.1	0.7	63.7	1.0	84.7	28.1	63.1	0.7	99.1	AVG
-7718DA2 Spot 9	2224	123655	3.2	20.6602	0.9	0.0668	1.4	0.0100	1.1	0.78	64.3	0.7	65.7	0.9	117.9	20.4	64.3	0.7	97.8	
-7718DA2 Spot 27	2260	63270	1.6	20.8334	0.7	0.0677	1.3	0.0102	1.1	0.83	65.7	0.7	66.5	0.8	98.2	16.7	65.7	0.7	98.7	
-7718DA2 Spot 7	387	24593	2.8	20.4138	1.8	0.0704	2.8	0.0104	2.1	0.77	66.9	1.4	69.1	1.9	146.2	42.0	66.9	1.4	96.8	
-7718DA2 Spot 3	2765	45736	1.4	20.6948	0.9	0.0703	1.5	0.0106	1.1	0.76	67.7	0.7	69.0	1.0	114.0	22.2	67.7	0.7	98.1	
-7718DA2 Spot 14	2919	40527	1.1	20.6939	0.9	0.0719	1.2	0.0108	0.8	0.66	69.3	0.5	70.5	0.8	114.1	21.3	69.3	0.5	98.2	
-7718DA2 Spot 15	260	8239	2.3	21.2078	2.1	0.0725	3.0	0.0112	2.1	0.70	71.5	1.5	71.1	2.0	55.9	51.1	71.5	1.5	100.6	
-7718DA2 Spot 26	874	22808	1.2	19.2470	1.7	0.0809	2.0	0.0113	1.2	0.58	72.4	0.9	79.0	1.6	282.5	38.2	72.4	0.9	91.7	
-7718DA2 Spot 10	3142	54231	1.1	21.1403	1.0	0.0741	1.5	0.0114	1.1	0.73	72.8	0.8	72.6	1.1	63.5	24.8	72.8	0.8	100.4	
~~-7718DA2 Spot 25~~	~~32~~	~~435~~	~~1.8~~	~~53.5173~~	~~69.5~~	~~0.0244~~	~~69.5~~	~~0.0095~~	~~1.9~~	~~0.03~~	~~60.8~~	~~1.1~~	~~24.5~~	~~16.8~~	~~NA~~	~~NA~~	~~60.8~~	~~1.1~~	~~248.4~~	*REV DISC
~~-7718DA2 Spot 6~~	~~36~~	~~1948~~	~~1.6~~	~~6.1153~~	~~7.3~~	~~0.2671~~	~~8.2~~	~~0.0119~~	~~3.9~~	~~0.47~~	~~76.0~~	~~2.9~~	~~240.4~~	~~17.6~~	~~2491.7~~	~~122.4~~	~~76.0~~	~~2.9~~	~~31.6~~	*DISC
~~-7718DA2 Spot 4~~	~~70~~	~~830~~	~~1.6~~	~~29.3564~~	~~4.3~~	~~0.0450~~	~~4.5~~	~~0.0096~~	~~1.2~~	~~0.27~~	~~61.5~~	~~0.7~~	~~44.7~~	~~2.0~~	~~NA~~	~~NA~~	~~61.5~~	~~0.7~~	~~137.6~~	*REV DISC
~~-7718DA2 Spot 29~~	~~92~~	~~1441~~	~~0.8~~	~~11.4611~~	~~8.2~~	~~0.1189~~	~~8.4~~	~~0.0099~~	~~1.6~~	~~0.19~~	~~63.4~~	~~1.0~~	~~114.1~~	~~9.0~~	~~1365.2~~	~~158.2~~	~~63.4~~	~~1.0~~	~~55.6~~	*DISC
~~-7718DA2 Spot 13~~	~~804~~	~~2415~~	~~3.1~~	~~13.1149~~	~~6.5~~	~~0.0991~~	~~7.1~~	~~0.0094~~	~~2.7~~	~~0.39~~	~~60.5~~	~~1.6~~	~~95.9~~	~~6.5~~	~~1100.8~~	~~130.4~~	~~60.5~~	~~1.6~~	~~63.1~~	*DISC
~~-7718DA2 Spot 35~~	~~230~~	~~3061~~	~~1.5~~	~~13.8608~~	~~4.8~~	~~0.0937~~	~~5.1~~	~~0.0094~~	~~1.8~~	~~0.36~~	~~60.5~~	~~1.1~~	~~91.0~~	~~4.5~~	~~989.2~~	~~97.4~~	~~60.5~~	~~1.1~~	~~66.5~~	*DISC

Analysis	U	206Pb	U/Th	206Pb*	±	207Pb*	±	206Pb*	±	error	206Pb*	±	207Pb*	±	206Pb*	±	Best age	±	Conc	Used for AVG
	(ppm)	204Pb		207Pb*	(%)	235U*	(%)	238U	(%)	corr.	238U*	(Ma)	235U	(Ma)	207Pb*	(Ma)	(Ma)	(Ma)	(%)	
-7318DA2 Spot 9	596	17523	0.6	20.8239	1.3	0.1052	1.8	0.0159	1.2	0.67	101.6	1.2	101.6	1.7	99.3	31.4	101.6	1.2	100.1	AVG
-7318DA2 Spot 26	709	14146	0.7	20.6821	1.0	0.1061	1.6	0.0159	1.3	0.79	101.9	1.3	102.4	1.6	115.5	23.2	101.9	1.3	99.5	AVG
-7318DA2 Spot 18	148	308064	1.0	15.7620	3.0	0.1393	3.2	0.0159	1.0	0.33	101.9	1.1	132.4	4.0	722.2	63.8	101.9	1.1	76.9	AVG
-7318DA2 Spot 2	478	32170	1.0	20.4677	1.1	0.1076	1.8	0.0160	1.4	0.78	102.2	1.4	103.8	1.8	140.0	26.9	102.2	1.4	98.5	AVG
-7318DA2 Spot 22	241	5277	1.3	21.0387	2.2	0.1049	2.5	0.0160	1.1	0.44	102.4	1.1	101.3	2.4	75.0	52.6	102.4	1.1	101.1	AVG
-7318DA2 Spot 6	567	200980	0.7	20.0162	0.9	0.1108	1.5	0.0161	1.2	0.81	102.9	1.2	106.7	1.5	192.1	20.7	102.9	1.2	96.5	AVG
-7318DA2 Spot 33	185	44013	1.4	19.5468	1.7	0.1136	2.0	0.0161	1.0	0.53	103.0	1.1	109.2	2.0	247.0	38.6	103.0	1.1	94.3	AVG
-7318DA2 Spot 13	203	7345	1.3	19.9672	1.9	0.1112	2.3	0.0161	1.2	0.54	103.1	1.3	107.1	2.3	197.8	44.0	103.1	1.3	96.2	AVG
-7318DA2 Spot 29	147	6617	1.2	20.3614	2.1	0.1091	2.5	0.0161	1.3	0.55	103.1	1.4	105.2	2.5	152.2	48.1	103.1	1.4	98.0	AVG
-7318DA2 Spot 31	182	8844	1.5	20.5133	2.2	0.1086	2.6	0.0162	1.4	0.55	103.4	1.5	104.7	2.6	134.7	51.2	103.4	1.5	98.7	AVG
-7318DA2 Spot 30	239	4821	1.2	21.2519	1.5	0.1049	1.9	0.0162	1.2	0.63	103.4	1.3	101.3	1.9	50.9	36.2	103.4	1.3	102.1	AVG
-7318DA2 Spot 8	278	11502	0.9	17.9222	2.0	0.1245	2.2	0.0162	1.1	0.47	103.5	1.1	119.1	2.5	443.3	43.8	103.5	1.1	86.9	AVG
-7318DA2 Spot 1	363	22067	1.1	20.4497	1.4	0.1091	1.9	0.0162	1.4	0.71	103.5	1.4	105.2	1.9	142.1	31.7	103.5	1.4	98.5	AVG
-7318DA2 Spot 25	818	61698	0.6	20.7185	1.0	0.1077	1.7	0.0162	1.4	0.81	103.6	1.4	103.9	1.7	111.3	23.3	103.6	1.4	99.7	AVG
-7318DA2 Spot 32	398	130228	0.9	20.4952	1.3	0.1090	1.7	0.0162	1.1	0.64	103.6	1.1	105.0	1.7	136.8	31.0	103.6	1.1	98.7	AVG
-7318DA2 Spot 11	227	12020	1.1	21.1414	1.5	0.1056	1.9	0.0162	1.0	0.55	103.6	1.1	102.0	1.8	63.4	36.9	103.6	1.1	101.6	AVG
-7318DA2 Spot 24	534	10434	0.9	20.1363	1.2	0.1110	1.6	0.0162	1.1	0.68	103.7	1.1	106.9	1.6	178.1	27.2	103.7	1.1	97.0	AVG
-7318DA2 Spot 10	428	15265	0.9	20.8268	1.4	0.1073	1.9	0.0162	1.2	0.64	103.7	1.2	103.5	1.9	99.0	34.2	103.7	1.2	100.2	AVG
-7318DA2 Spot 12	278	38085	1.2	19.5406	2.0	0.1145	2.3	0.0162	1.2	0.52	103.8	1.2	110.0	2.4	247.7	45.0	103.8	1.2	94.3	AVG
-7318DA2 Spot 3	671	134376	0.8	19.9311	1.2	0.1122	1.7	0.0162	1.2	0.70	103.8	1.2	108.0	1.7	202.0	27.9	103.8	1.2	96.1	AVG
-7318DA2 Spot 4	273	8276	1.2	19.5030	2.5	0.1147	3.0	0.0162	1.6	0.55	103.8	1.7	110.3	3.1	252.2	57.0	103.8	1.7	94.1	AVG
-7318DA2 Spot 7	433	7210	1.2	21.6319	1.2	0.1036	1.6	0.0163	1.0	0.66	104.0	1.1	100.1	1.5	8.5	29.0	104.0	1.1	103.9	AVG
-7318DA2 Spot 23	421	27510	1.3	20.0335	1.4	0.1119	2.0	0.0163	1.4	0.70	104.0	1.4	107.7	2.0	190.1	32.7	104.0	1.4	96.6	AVG
-7318DA2 Spot 34	409	60852	0.9	19.9202	1.2	0.1129	1.8	0.0163	1.4	0.76	104.3	1.4	108.6	1.9	203.3	28.0	104.3	1.4	96.1	AVG
-7318DA2 Spot 35	192	275790	1.1	16.0749	4.4	0.1403	4.6	0.0164	1.3	0.29	104.6	1.4	133.3	5.7	680.3	94.1	104.6	1.4	78.5	AVG
-7318DA2 Spot 20	248	10729	1.2	20.4900	2.1	0.1102	2.5	0.0164	1.3	0.52	104.8	1.3	106.1	2.5	137.4	49.2	104.8	1.3	98.7	AVG
-7318DA2 Spot 14	211	136634	1.1	20.4219	1.6	0.1106	2.2	0.0164	1.5	0.67	104.8	1.5	106.5	2.2	145.2	38.6	104.8	1.5	98.4	AVG
-7318DA2 Spot 16	112	6513	1.3	21.3269	3.1	0.1060	3.3	0.0164	1.2	0.38	104.9	1.3	102.3	3.2	42.6	73.2	104.9	1.3	102.5	AVG
-7318DA2 Spot 17	343	9040	0.9	20.7902	2.2	0.1090	2.5	0.0164	1.2	0.46	105.1	1.2	105.0	2.5	103.1	52.4	105.1	1.2	100.1	AVG
-7318DA2 Spot 28	199	20440	1.1	18.6064	2.2	0.1232	2.5	0.0166	1.1	0.47	106.3	1.2	118.0	2.7	359.4	49.0	106.3	1.2	90.1	
-7318DA2 Spot 5	308	10126	2.7	18.2574	1.7	0.1256	2.2	0.0166	1.5	0.66	106.4	1.6	120.2	2.5	401.9	37.4	106.4	1.6	88.5	
-7318DA2 Spot 15	384	9149	1.1	20.8041	2.2	0.1106	2.7	0.0167	1.5	0.56	106.7	1.6	106.5	2.7	101.6	52.6	106.7	1.6	100.2	
-7318DA2 Spot 27	310	15864	1.2	20.6477	1.2	0.1117	1.9	0.0167	1.6	0.81	107.0	1.7	107.5	2.0	119.4	27.2	107.0	1.7	99.5	
-7318DA2 Spot 21	167	10518	0.9	20.4385	2.3	0.1149	2.6	0.0170	1.3	0.49	108.9	1.4	110.5	2.7	143.3	52.9	108.9	1.4	98.6	
-7318DA2 Spot 19	335	3759	0.7	19.7272	3.0	0.1222	3.2	0.0175	1.3	0.41	111.7	1.5	117.0	3.6	225.8	68.2	111.7	1.5	95.5	

Analysis	U	206Pb	U/Th	206Pb*	±	207Pb*	±	206Pb*	±	error	206Pb*	±	207Pb*	±	206Pb*	±	Best age	±	Conc	Used for AVG
	(ppm)	204Pb		207Pb*	(%)	235U*	(%)	238U	(%)	corr.	238U*	(Ma)	235U	(Ma)	207Pb*	(Ma)	(Ma)	(Ma)	(%)	
-7418DA1 Spot 46	6021	11152	6.2	17.7732	1.8	0.0446	2.2	0.0058	1.3	0.58	37.0	0.5	44.4	1.0	461.9	40.2	37.0	0.5	83.4	
-7418DA1 Spot 67	5834	50309	4.9	21.0415	0.9	0.0387	1.5	0.0059	1.2	0.78	38.0	0.4	38.6	0.6	74.7	22.1	38.0	0.4	98.5	
-7418DA1 Spot 68	2683	33853	3.8	21.2309	1.1	0.0406	1.5	0.0063	1.0	0.70	40.2	0.4	40.4	0.6	53.3	25.2	40.2	0.4	99.5	
-7418DA1 Spot 63	3313	12476	9.2	20.3948	1.1	0.0434	1.6	0.0064	1.1	0.69	41.3	0.4	43.1	0.7	148.3	26.3	41.3	0.4	95.7	AVG
-7418DA1 Spot 42	1266	23551	2.7	20.8719	1.4	0.0428	2.0	0.0065	1.5	0.71	41.6	0.6	42.5	0.8	93.8	33.8	41.6	0.6	97.9	AVG
-7418DA1 Spot 40	1315	26914	1.8	20.5791	1.3	0.0439	1.7	0.0066	1.1	0.65	42.1	0.5	43.6	0.7	127.2	31.0	42.1	0.5	96.5	AVG
-7418DA1 Spot 54	1680	24527	3.6	19.6517	1.5	0.0462	1.8	0.0066	1.0	0.56	42.3	0.4	45.8	0.8	234.7	33.9	42.3	0.4	92.3	AVG
-7418DA1 Spot 43	846	3983	1.6	16.1207	1.4	0.0563	2.3	0.0066	1.8	0.80	42.3	0.8	55.6	1.2	674.3	29.3	42.3	0.8	76.1	AVG
-7418DA1 Spot 61	736	16489	1.0	20.8056	1.3	0.0437	1.8	0.0066	1.3	0.73	42.4	0.6	43.4	0.8	101.4	29.7	42.4	0.6	97.6	AVG
-7418DA1 Spot 36	939	10394	1.4	20.1930	1.0	0.0450	1.5	0.0066	1.1	0.75	42.4	0.5	44.7	0.7	171.6	23.2	42.4	0.5	94.8	AVG
-7418DA1 Spot 62	1625	49443	2.1	21.3643	0.8	0.0427	1.5	0.0066	1.3	0.84	42.5	0.5	42.5	0.6	38.3	19.1	42.5	0.5	100.2	AVG
-7418DA1 Spot 37	1734	17534	2.6	21.5530	1.0	0.0426	1.4	0.0067	1.0	0.73	42.8	0.4	42.3	0.6	17.2	23.0	42.8	0.4	101.0	AVG
-7418DA1 Spot 48	883	9089	1.1	22.1213	2.3	0.0425	2.7	0.0068	1.4	0.52	43.8	0.6	42.3	1.1	NA	NA	43.8	0.6	103.7	
-7418DA1 Spot 53	788	63665	1.9	20.1995	1.0	0.0470	1.6	0.0069	1.3	0.78	44.3	0.6	46.7	0.7	170.8	23.8	44.3	0.6	94.9	
-7418DA1 Spot 52	270	5221	1.0	18.8208	2.2	0.1236	2.4	0.0169	1.0	0.41	107.9	1.1	118.4	2.7	333.5	50.3	107.9	1.1	91.2	

Analysis	U	206Pb	U/Th	206Pb*	±	207Pb*	±	206Pb*	±	error	206Pb*	±	207Pb*	±	206Pb*	±	Best age	±	Conc	Used for AVG
	(ppm)	204Pb		207Pb*	(%)	235U*	(%)	238U	(%)	corr.	238U*	(Ma)	235U	(Ma)	207Pb*	(Ma)	(Ma)	(Ma)	(%)	
-7418DA2 Spot 4	6326	41872	10.2	21.5563	0.9	0.0376	1.7	0.0059	1.4	0.84	37.8	0.5	37.5	0.6	16.9	22.0	37.8	0.5	100.9	
-7418DA2 Spot 7	2985	49368	7.1	20.9566	1.1	0.0393	1.8	0.0060	1.4	0.78	38.4	0.5	39.2	0.7	84.2	26.4	38.4	0.5	98.1	
-7418DA2 Spot 30	3845	25315	6.3	21.1013	1.1	0.0397	1.6	0.0061	1.1	0.73	39.1	0.4	39.5	0.6	67.9	25.1	39.1	0.4	98.8	
-7418DA2 Spot 11	2953	50419	5.4	21.3621	0.9	0.0406	1.6	0.0063	1.3	0.81	40.4	0.5	40.4	0.6	38.6	22.6	40.4	0.5	100.1	
-7418DA2 Spot 20	3116	5003	21.5	15.3107	3.2	0.0574	3.5	0.0064	1.3	0.39	41.0	0.5	56.7	1.9	783.5	66.8	41.0	0.5	72.3	
-7418DA2 Spot 6	2270	42972	3.0	19.5711	1.0	0.0449	1.6	0.0064	1.2	0.76	41.0	0.5	44.6	0.7	244.2	23.8	41.0	0.5	91.9	
-7418DA2 Spot 1	1085	15130	3.9	21.4409	1.4	0.0424	1.8	0.0066	1.1	0.62	42.4	0.5	42.2	0.8	29.8	34.2	42.4	0.5	100.5	AVG
-7418DA2 Spot 2	712	41387	1.2	20.2451	1.3	0.0454	1.7	0.0067	1.1	0.65	42.8	0.5	45.1	0.8	165.6	30.4	42.8	0.5	95.0	AVG
-7418DA2 Spot 35	443	6183582	0.9	21.1136	1.6	0.0437	2.2	0.0067	1.5	0.67	43.0	0.6	43.4	0.9	66.5	38.0	43.0	0.6	99.0	AVG
-7418DA2 Spot 28	494	8108	1.3	21.6698	2.7	0.0430	3.2	0.0068	1.7	0.52	43.5	0.7	42.8	1.3	4.3	66.2	43.5	0.7	101.6	AVG
-7418DA2 Spot 5	665	5117	2.6	19.2582	3.2	0.0489	3.5	0.0068	1.4	0.39	43.9	0.6	48.5	1.6	281.2	72.6	43.9	0.6	90.6	AVG
-7418DA2 Spot 3	950	16252	2.0	20.3715	1.5	0.0465	2.1	0.0069	1.5	0.71	44.1	0.7	46.1	0.9	151.0	34.5	44.1	0.7	95.7	AVG

Analysis	U	206Pb	U/Th	206Pb*	±	207Pb*	±	206Pb*	±	error	206Pb*	±	207Pb*	±	206Pb*	±	Best age	±	Conc	Used for AVG
	(ppm)	204Pb		207Pb*	(%)	235U*	(%)	238U	(%)	corr.	238U*	(Ma)	235U	(Ma)	207Pb*	(Ma)	(Ma)	(Ma)	(%)	
-7418DA3 Spot 14	1201	24153	1.0	20.4860	1.2	0.0429	1.6	0.0064	1.1	0.67	41.0	0.4	42.7	0.7	137.9	28.2	41.0	0.4	NA	
-7418DA3 Spot 29	812	32826	0.9	20.8023	1.4	0.0434	2.0	0.0066	1.5	0.73	42.1	0.6	43.1	0.8	101.7	32.3	42.1	0.6	NA	AVG
-7418DA3 Spot 28	1346	41138	2.2	20.9879	1.0	0.0432	1.4	0.0066	1.0	0.72	42.3	0.4	43.0	0.6	80.7	23.6	42.3	0.4	NA	AVG
-7418DA3 Spot 8	522	28187	3.1	20.5872	1.1	0.0442	1.6	0.0066	1.1	0.70	42.4	0.5	43.9	0.7	126.3	26.4	42.4	0.5	NA	AVG
-7418DA3 Spot 1_C	2134	11469	0.0	16.9094	3.5	0.0539	4.0	0.0066	2.1	0.51	42.5	0.9	53.3	2.1	571.2	75.4	42.5	0.9	NA	AVG
-7418DA3 Spot 20	1122	78036	3.5	20.5391	1.0	0.0447	1.5	0.0067	1.2	0.76	42.8	0.5	44.4	0.7	131.8	23.5	42.8	0.5	NA	AVG
-7418DA3 Spot 30	1143	12702	3.4	20.0788	1.1	0.0461	1.6	0.0067	1.1	0.71	43.2	0.5	45.8	0.7	184.8	25.5	43.2	0.5	NA	AVG
-7418DA3 Spot 4_C	133	7277	1.0	19.2251	2.6	0.0483	3.0	0.0067	1.5	0.51	43.3	0.7	47.9	1.4	285.1	58.6	43.3	0.7	NA	AVG
-7418DA3 Spot 2	1039	6089	2.2	18.4072	2.7	0.0508	3.0	0.0068	1.2	0.42	43.6	0.5	50.3	1.5	383.6	60.8	43.6	0.5	NA	AVG
-7418DA3 Spot 32	1251	25511	2.1	19.5265	1.1	0.0482	1.6	0.0068	1.2	0.76	43.9	0.5	47.8	0.8	249.4	24.5	43.9	0.5	NA	AVG
-7418DA3 Spot 12	1227	22747	3.8	20.6218	1.1	0.0463	1.6	0.0069	1.1	0.72	44.5	0.5	46.0	0.7	122.3	25.4	44.5	0.5	NA	
-7418DA3 Spot 5_R	357	11953	1.5	20.8931	1.4	0.0459	1.9	0.0070	1.2	0.67	44.7	0.6	45.6	0.8	91.4	32.5	44.7	0.6	NA	
-7418DA3 Spot 18	700	1426	1.1	7.1124	7.2	0.1411	7.6	0.0073	2.2	0.30	46.8	1.0	134.1	9.5	2233.8	125.4	46.8	1.0	NA	
-7418DA3 Spot 25	152	10345	1.7	20.3995	1.8	0.0562	2.2	0.0083	1.3	0.59	53.4	0.7	55.5	1.2	147.8	41.1	53.4	0.7	NA	
-7418DA3 Spot 24	137	5453	0.9	20.8406	2.1	0.0583	2.5	0.0088	1.4	0.55	56.6	0.8	57.6	1.4	97.4	49.4	56.6	0.8	NA	
-7418DA3 Spot 3	1656	21905	1.4	20.9616	1.1	0.0584	1.6	0.0089	1.1	0.73	57.0	0.6	57.6	0.9	83.7	25.6	57.0	0.6	NA	
-7418DA3 Spot 19	769	32763	1.9	21.1619	1.4	0.0581	2.0	0.0089	1.4	0.71	57.3	0.8	57.3	1.1	61.1	33.0	57.3	0.8	NA	
-7418DA3 Spot 6	284	5737	2.2	19.4313	2.1	0.0634	2.6	0.0089	1.5	0.58	57.4	0.9	62.4	1.6	260.6	48.0	57.4	0.9	NA	
-7418DA3 Spot 11	1003	38816	1.8	20.4997	1.0	0.0602	1.4	0.0090	1.0	0.72	57.5	0.6	59.4	0.8	136.3	23.3	57.5	0.6	NA	
-7418DA3 Spot 9	1175	195827	1.6	20.7937	0.8	0.0595	1.2	0.0090	0.9	0.74	57.6	0.5	58.7	0.7	102.7	19.1	57.6	0.5	NA	
-7418DA3 Spot 21	616	15029	2.5	21.4514	1.1	0.0577	1.7	0.0090	1.3	0.76	57.7	0.7	57.0	0.9	28.6	26.6	57.7	0.7	NA	
-7418DA3 Spot 33	897	109121	1.7	20.6517	0.9	0.0600	1.3	0.0090	0.9	0.71	57.7	0.5	59.2	0.7	118.9	21.6	57.7	0.5	NA	
-7418DA3 Spot 10	114	3120	1.6	20.6174	5.6	0.0604	5.8	0.0090	1.3	0.22	58.0	0.7	59.5	3.3	122.8	132.5	58.0	0.7	NA	
-7418DA3 Spot 23	1035	51411	1.6	20.9291	1.1	0.0597	1.7	0.0091	1.3	0.76	58.1	0.7	58.8	0.9	87.4	25.3	58.1	0.7	NA	
-7418DA3 Spot 27	124	2647	1.2	23.3622	5.3	0.0537	5.5	0.0091	1.3	0.23	58.4	0.7	53.1	2.8	NA	NA	58.4	0.7	NA	
-7418DA3 Spot 22	106	5548	1.4	20.4884	2.2	0.0616	2.7	0.0092	1.6	0.58	58.8	0.9	60.7	1.6	137.6	51.6	58.8	0.9	NA	
-7418DA3 Spot 26	358	15225	1.6	21.2475	1.4	0.0594	1.7	0.0092	1.0	0.59	58.8	0.6	58.6	1.0	51.4	33.0	58.8	0.6	NA	
-7418DA3 Spot 17	119	5496	2.4	21.4189	2.7	0.0595	2.9	0.0092	1.2	0.41	59.3	0.7	58.7	1.7	32.2	63.7	59.3	0.7	NA	
-7418DA3 Spot 31	182	2202	1.4	15.6767	5.9	0.0855	6.2	0.0097	1.7	0.27	62.4	1.0	83.3	4.9	733.7	126.1	62.4	1.0	NA	
-7418DA3 Spot 34	404	1568	1.3	8.4845	5.1	0.1655	5.3	0.0102	1.1	0.21	65.3	0.7	155.5	7.6	1923.3	92.3	65.3	0.7	NA	
-7418DA3 Spot 35	986	5614	1.2	16.0525	3.2	0.0882	3.7	0.0103	1.8	0.50	65.9	1.2	85.8	3.0	683.4	67.9	65.9	1.2	NA	
-7418DA3 Spot 16	291	1944637	1.8	13.1869	0.9	1.9802	1.6	0.1895	1.4	0.84	1118.5	14.1	1108.8	11.0	1089.8	17.8	1089.8	17.8	102.6	
-7418DA3 Spot 15	188	88353	2.2	13.1127	0.8	1.9875	1.6	0.1891	1.4	0.86	1116.5	14.0	1111.3	10.7	1101.1	16.0	1101.1	16.0	101.4	
-7418DA3 Spot 13	250	217027	1.9	8.0945	0.8	5.6083	1.4	0.3294	1.2	0.84	1835.4	19.4	1917.4	12.4	2007.2	13.7	2007.2	13.7	91.4	

Analysis	U	206Pb	U/Th	206Pb*	±	207Pb*	±	206Pb*	±	error	206Pb*	±	207Pb*	±	206Pb*	±	Best age	±	Conc	Used for AVG
	(ppm)	204Pb		207Pb*	(%)	235U*	(%)	238U	(%)	corr.	238U*	(Ma)	235U	(Ma)	207Pb*	(Ma)	(Ma)	(Ma)	(%)	
-7318DA1 Spot 53	158	5511	0.9	21.8469	2.2	0.0486	2.5	0.0077	1.2	0.46	49.5	0.6	48.2	1.2	NA	NA	49.5	0.6	NA	
-7318DA1 Spot 65	255	37499	1.0	21.1011	1.7	0.0515	2.1	0.0079	1.3	0.60	50.6	0.6	51.0	1.0	68.0	40.0	50.6	0.6	NA	
-7318DA1 Spot 69	178	4910	1.1	22.0772	1.9	0.0509	2.1	0.0081	1.0	0.49	52.3	0.5	50.4	1.0	NA	NA	52.3	0.5	NA	
-7318DA1 Spot 47	124	2038	1.6	23.9802	5.5	0.0500	5.6	0.0087	1.2	0.21	55.8	0.7	49.5	2.7	NA	NA	55.8	0.7	NA	AVG
-7318DA1 Spot 38	208	10626	1.6	20.4252	1.7	0.0587	2.2	0.0087	1.3	0.59	55.8	0.7	57.9	1.2	144.8	40.7	55.8	0.7	NA	AVG
-7318DA1 Spot 36_C	2114	21808	1.6	21.1029	1.1	0.0571	1.7	0.0087	1.3	0.77	56.1	0.7	56.4	1.0	67.8	26.6	56.1	0.7	NA	AVG
-7318DA1 Spot 51	202	5569	1.6	22.0862	2.0	0.0547	2.4	0.0088	1.3	0.54	56.2	0.7	54.0	1.3	NA	NA	56.2	0.7	NA	AVG
-7318DA1 Spot 44_C	250	2597	1.5	23.0308	1.8	0.0524	2.4	0.0088	1.6	0.66	56.2	0.9	51.9	1.2	NA	NA	56.2	0.9	NA	AVG
-7318DA1 Spot 49_R	124	1945	1.9	19.2262	4.4	0.0629	4.6	0.0088	1.3	0.29	56.3	0.7	62.0	2.8	285.0	101.6	56.3	0.7	NA	AVG
-7318DA1 Spot 43	71	2096	1.7	25.9908	3.6	0.0466	3.9	0.0088	1.3	0.33	56.4	0.7	46.2	1.7	NA	NA	56.4	0.7	NA	AVG
-7318DA1 Spot 42	101	3565	1.2	11.2745	7.8	0.1075	7.9	0.0088	1.3	0.17	56.4	0.8	103.7	7.8	1396.8	149.8	56.4	0.8	NA	AVG
-7318DA1 Spot 57	142	2550	1.2	23.6745	4.9	0.0513	5.0	0.0088	1.0	0.19	56.5	0.5	50.8	2.5	NA	NA	56.5	0.5	NA	AVG
-7318DA1 Spot 48_C	762	54885	1.6	20.8971	1.0	0.0584	1.5	0.0089	1.2	0.78	56.8	0.7	57.6	0.9	91.0	23.0	56.8	0.7	NA	AVG
-7318DA1 Spot 45_R	149	2327	1.7	23.3360	3.7	0.0526	4.0	0.0089	1.4	0.35	57.1	0.8	52.0	2.0	NA	NA	57.1	0.8	NA	AVG
-7318DA1 Spot 37_R	103	1434	1.1	12.6045	5.2	0.0975	5.4	0.0089	1.2	0.22	57.2	0.7	94.5	4.9	1179.7	103.9	57.2	0.7	NA	AVG
-7318DA1 Spot 66	256	12948	0.9	18.7240	1.6	0.0659	2.0	0.0089	1.2	0.60	57.4	0.7	64.8	1.2	345.2	36.0	57.4	0.7	NA	AVG
-7318DA1 Spot 54	77	16411	1.8	16.7996	4.0	0.0736	4.2	0.0090	1.4	0.32	57.5	0.8	72.1	2.9	585.4	86.4	57.5	0.8	NA	AVG
-7318DA1 Spot 50	110	9252	1.4	20.4047	2.5	0.0607	2.8	0.0090	1.3	0.45	57.7	0.7	59.9	1.7	147.2	59.4	57.7	0.7	NA	AVG
-7318DA1 Spot 62	411	18140	2.2	20.8731	1.4	0.0604	1.7	0.0092	1.0	0.58	58.7	0.6	59.6	1.0	93.7	32.9	58.7	0.6	NA	
-7318DA1 Spot 59	49	4060	1.8	17.5418	3.4	0.0722	3.8	0.0092	1.7	0.45	58.9	1.0	70.8	2.6	490.8	75.1	58.9	1.0	NA	
-7318DA1 Spot 41_R	157	13374	1.7	20.8320	1.8	0.0611	2.5	0.0092	1.7	0.67	59.2	1.0	60.2	1.5	98.4	43.8	59.2	1.0	NA	
-7318DA1 Spot 55	69	2508	1.6	6.8014	11.6	0.1895	11.7	0.0094	1.5	0.13	60.0	0.9	176.2	18.9	2310.9	200.0	60.0	0.9	NA	
-7318DA1 Spot 56	215	7998	2.0	13.2421	2.8	0.1057	3.1	0.0102	1.2	0.40	65.1	0.8	102.0	3.0	1081.4	56.6	65.1	0.8	NA	
-7318DA1 Spot 40_C	151	3582	1.3	22.8956	2.1	0.0672	2.7	0.0112	1.6	0.60	71.6	1.1	66.0	1.7	NA	NA	71.6	1.1	NA	
-7318DA1 Spot 61_R	120	1679	1.9	25.9359	1.9	0.0705	2.3	0.0133	1.3	0.55	85.0	1.1	69.2	1.6	NA	NA	85.0	1.1	NA	
-7318DA1 Spot 39	114	10428	1.4	20.6931	2.3	0.0983	2.8	0.0148	1.6	0.58	94.5	1.5	95.2	2.5	114.2	53.4	94.5	1.5	NA	
-7318DA1 Spot 46	94	8662	1.1	21.1548	2.0	0.1073	2.4	0.0165	1.2	0.52	105.4	1.3	103.5	2.3	61.9	48.3	105.4	1.3	NA	
-7318DA1 Spot 70	269	43606	0.7	20.4655	1.4	0.1291	2.0	0.0192	1.4	0.71	122.4	1.7	123.2	2.3	140.2	32.8	122.4	1.7	NA	
-7318DA1 Spot 52	791	122334	3.7	19.9251	0.9	0.2307	1.6	0.0333	1.3	0.80	211.5	2.6	210.8	3.0	202.7	21.5	211.5	2.6	NA	
-7318DA1 Spot 60_C	64	10322	2.1	17.0695	0.9	0.7853	1.3	0.0973	0.9	0.67	598.3	4.9	588.5	5.7	550.7	20.7	598.3	4.9	108.6	

Analysis	U	206Pb	U/Th	206Pb*	±	207Pb*	±	206Pb*	±	error	206Pb*	±	207Pb*	±	206Pb*	±	Best age	±	Conc	Used for AVG
	(ppm)	204Pb		207Pb*	(%)	235U*	(%)	238U	(%)	corr.	238U*	(Ma)	235U	(Ma)	207Pb*	(Ma)	(Ma)	(Ma)	(%)	
-7218DA2 Spot 10	867	30844	2.0	21.0254	1.0	0.0590	1.5	0.0090	1.1	0.74	57.8	0.7	58.2	0.9	76.5	24.5	57.8	0.7	NA	AVG
-7218DA2 Spot 14	1018	30461	2.3	21.0122	1.0	0.0593	1.6	0.0090	1.2	0.78	58.0	0.7	58.5	0.9	77.9	23.8	58.0	0.7	NA	AVG
-7218DA2 Spot 7	830	53174	1.8	20.8567	1.0	0.0598	1.5	0.0090	1.2	0.76	58.1	0.7	59.0	0.9	95.6	23.6	58.1	0.7	NA	AVG
-7218DA2 Spot 31	463	104477	2.0	20.2112	1.5	0.0619	2.2	0.0091	1.5	0.70	58.3	0.9	61.0	1.3	169.5	36.1	58.3	0.9	NA	AVG
-7218DA2 Spot 18	181	17369	1.2	20.6855	1.9	0.0605	2.5	0.0091	1.6	0.64	58.3	0.9	59.7	1.4	115.1	45.4	58.3	0.9	NA	AVG
-7218DA2 Spot 22	79	2862	1.1	22.4897	4.5	0.0559	4.9	0.0091	1.7	0.36	58.5	1.0	55.2	2.6	NA	NA	58.5	1.0	NA	AVG
-7218DA2 Spot 20_C	333	18812	2.2	20.3775	1.7	0.0618	2.2	0.0091	1.4	0.62	58.6	0.8	60.8	1.3	150.3	40.2	58.6	0.8	NA	AVG
-7218DA2 Spot 24_R	380	60696	1.4	20.2614	1.1	0.0622	1.8	0.0091	1.4	0.77	58.7	0.8	61.3	1.1	163.7	26.5	58.7	0.8	NA	AVG
-7218DA2 Spot 4	273	63014	3.2	21.0350	1.9	0.0600	2.2	0.0092	1.2	0.55	58.7	0.7	59.1	1.3	75.4	44.0	58.7	0.7	NA	AVG
-7218DA2 Spot 16	715	8278	1.8	21.6297	1.4	0.0587	1.8	0.0092	1.1	0.61	59.1	0.6	57.9	1.0	8.8	34.1	59.1	0.6	NA	AVG
-7218DA2 Spot 28	47	927	1.8	31.2441	26.0	0.0407	26.1	0.0092	1.9	0.07	59.2	1.1	40.5	10.3	NA	NA	59.2	1.1	NA	AVG
-7218DA2 Spot 15	541	17706	2.3	19.2378	1.5	0.0663	2.2	0.0092	1.7	0.75	59.3	1.0	65.1	1.4	283.6	33.9	59.3	1.0	NA	AVG
-7218DA2 Spot 17	355	19614	2.6	18.5038	2.2	0.0689	2.8	0.0093	1.7	0.61	59.4	1.0	67.7	1.8	371.8	49.5	59.4	1.0	NA	AVG
-7218DA2 Spot 25_C	89	4914	1.4	21.2608	4.1	0.0602	4.3	0.0093	1.3	0.30	59.6	0.8	59.4	2.5	50.0	98.7	59.6	0.8	NA	AVG
-7218DA2 Spot 32	271	30456	2.8	21.5874	1.4	0.0594	2.0	0.0093	1.4	0.70	59.7	0.8	58.6	1.2	13.4	34.7	59.7	0.8	NA	AVG
-7218DA2 Spot 30	658	11236	2.4	19.4147	1.7	0.0661	2.3	0.0093	1.5	0.66	59.8	0.9	65.0	1.4	262.6	39.6	59.8	0.9	NA	AVG
-7218DA2 Spot 26_R	51	1168	1.6	27.0410	17.9	0.0475	18.0	0.0093	1.4	0.08	59.8	0.8	47.1	8.3	NA	NA	59.8	0.8	NA	AVG
-7218DA2 Spot 6	688	34245	2.1	21.7566	1.3	0.0594	2.0	0.0094	1.5	0.76	60.2	0.9	58.6	1.1	NA	NA	60.2	0.9	NA	AVG
-7218DA2 Spot 11	116	2801	1.4	23.3953	2.5	0.0554	2.9	0.0094	1.6	0.54	60.3	0.9	54.7	1.6	NA	NA	60.3	0.9	NA	AVG
-7218DA2 Spot 19	1266	26145	2.3	21.0125	1.3	0.0617	1.9	0.0094	1.3	0.72	60.3	0.8	60.8	1.1	77.9	30.6	60.3	0.8	NA	AVG
-7218DA2 Spot 35_R	298	4066	1.7	17.3131	2.5	0.0758	3.1	0.0095	1.7	0.57	61.1	1.1	74.2	2.2	519.7	55.9	61.1	1.1	NA	
-7218DA2 Spot 29	155	3846	2.3	22.5550	2.5	0.0583	2.9	0.0095	1.6	0.54	61.2	1.0	57.6	1.6	NA	NA	61.2	1.0	NA	
-7218DA2 Spot 13_R	70	12617	2.0	20.6333	3.1	0.0653	3.5	0.0098	1.5	0.44	62.7	0.9	64.2	2.2	121.0	74.0	62.7	0.9	NA	
-7218DA2 Spot 34	56	29868	2.1	20.8301	3.3	0.0648	3.7	0.0098	1.6	0.44	62.8	1.0	63.8	2.3	98.6	78.8	62.8	1.0	NA	
-7218DA2 Spot 21_R	131	1472	1.5	9.2235	3.5	0.1464	3.7	0.0098	1.2	0.33	62.9	0.8	138.7	4.8	1772.2	64.4	62.9	0.8	NA	
-7218DA2 Spot 12_C	1841	90186	2.1	20.4490	0.9	0.0678	1.4	0.0101	1.0	0.73	64.6	0.6	66.6	0.9	142.1	22.1	64.6	0.6	NA	
-7218DA2 Spot 27	250	58775	3.5	19.7863	1.9	0.0702	2.5	0.0101	1.6	0.66	64.7	1.1	68.9	1.7	218.9	43.3	64.7	1.1	NA	
-7218DA2 Spot 5	303	46508	1.6	20.1829	1.6	0.0693	2.2	0.0101	1.5	0.69	65.1	1.0	68.0	1.5	172.7	37.9	65.1	1.0	NA	
-7218DA2 Spot 1	281	21625	1.9	21.2374	1.6	0.0666	2.1	0.0103	1.5	0.69	65.8	1.0	65.5	1.4	52.6	37.0	65.8	1.0	NA	
-7218DA2 Spot 33_C	175	8572	1.6	20.4319	2.5	0.0696	3.0	0.0103	1.6	0.53	66.2	1.0	68.3	2.0	144.1	59.8	66.2	1.0	NA	
-7218DA2 Spot 8	55	2869	1.4	8.2059	12.6	0.1790	12.9	0.0107	2.7	0.21	68.3	1.9	167.2	19.9	1982.9	225.5	68.3	1.9	NA	

APPENDIX B

LU-HF ISOTOPE GEOCHEMISTRY DATA

Sample	Order	(^{176}Yb + ^{176}Lu) / ^{176}Hf (%)	Volts Hf	^{176}Hf/^{177}Hf	± (1σ)	^{176}Lu/^{177}Hf	^{176}Hf/^{177}Hf (T)	E-Hf (0)	E-Hf (0) ± (1σ)	E-Hf (T)	U/Pb Age (Ma)
LASKOWSKI 7218DA2 SPOT 18	6	31.5	2.5	0.282747	0.000030	0.002002	0.282745	-1.3	1.1	-0.1	58
LASKOWSKI 7218DA2 SPOT 20_C	10	28.2	3.4	0.282677	0.000030	0.001767	0.282675	-3.8	1.0	-2.6	59
LASKOWSKI 7218DA2 SPOT 25_C	8	40.1	2.6	0.282828	0.000039	0.002502	0.282825	1.5	1.4	2.7	60
LASKOWSKI 7218DA2 SPOT 28	7	13.3	2.7	0.282814	0.000030	0.001017	0.282813	1.0	1.1	2.3	59
LASKOWSKI 7218DA2 SPOT 30	9	51.5	4.0	0.282734	0.000029	0.003060	0.282731	-1.8	1.0	-0.6	60
LASKOWSKI 7218DA2 SPOT 34	3	10.5	3.2	0.282772	0.000031	0.000683	0.282771	-0.5	1.1	0.9	63
LASKOWSKI 7218DA2 SPOT 4	11	27.5	3.8	0.282670	0.000031	0.001619	0.282668	-4.1	1.1	-2.8	59
LASKOWSKI 7218DA2 SPOT 7	4	41.1	4.1	0.282742	0.000020	0.002496	0.282739	-1.5	0.7	-0.3	58
LASKOWSKI 7318DA1 SPOT 41_R	1	17.0	3.5	0.282795	0.000027	0.001095	0.282794	0.4	0.9	1.6	59
LASKOWSKI 7318DA1 SPOT 43	16	13.7	2.8	0.282790	0.000029	0.000921	0.282789	0.2	1.0	1.4	56
LASKOWSKI 7318DA1 SPOT 47	12	31.7	2.8	0.282696	0.000036	0.002053	0.282694	-3.2	1.3	-2.0	56
LASKOWSKI 7318DA1 SPOT 50	13	21.9	3.2	0.282661	0.000025	0.001367	0.282659	-4.4	0.9	-3.2	58
LASKOWSKI 7318DA1 SPOT 51	14	31.7	4.4	0.282793	0.000037	0.002478	0.282790	0.3	1.3	1.4	56
LASKOWSKI 7318DA2 SPOT 10	19	37.4	3.4	0.283017	0.000027	0.002113	0.283013	8.2	1.0	10.4	104
LASKOWSKI 7318DA2 SPOT 13	24	28.8	3.1	0.283012	0.000021	0.001946	0.283008	8.0	0.7	10.2	103
LASKOWSKI 7318DA2 SPOT 22	33	19.3	3.3	0.282950	0.000037	0.001211	0.282948	5.9	1.3	8.0	102
LASKOWSKI 7318DA2 SPOT 23	25	28.9	2.8	0.283011	0.000028	0.001779	0.283007	8.0	1.0	10.2	104
LASKOWSKI 7318DA2 SPOT 28	34	14.6	3.3	0.282992	0.000035	0.000868	0.282990	7.3	1.2	9.5	100
LASKOWSKI 7318DA2 SPOT 3	20	49.4	3.2	0.282950	0.000040	0.002959	0.282945	5.8	1.4	7.9	104
LASKOWSKI 7318DA2 SPOT 31	17	16.6	3.2	0.282948	0.000029	0.001008	0.282946	5.8	1.0	8.0	103
LASKOWSKI 7318DA2 SPOT 32	23	34.6	3.3	0.282953	0.000026	0.001972	0.282950	6.0	0.9	8.1	104
LASKOWSKI 7318DA2 SPOT 34	18	46.9	3.4	0.282918	0.000029	0.002480	0.282913	4.7	1.0	6.9	104
LASKOWSKI 7318DA2 SPOT 8	21	24.5	2.8	0.282921	0.000037	0.001488	0.282918	4.8	1.3	7.0	104
LASKOWSKI 7318DA2 SPOT 9	31	37.9	3.1	0.283004	0.000027	0.002215	0.283000	7.7	1.0	9.8	102
LASKOWSKI 7418DA1 SPOT 48	28	19.1	3.3	0.282648	0.000020	0.001169	0.282647	-4.8	0.7	-3.9	44
LASKOWSKI 7418DA1 SPOT 53	30	8.3	4.4	0.282673	0.000027	0.000575	0.282673	-3.9	1.0	-3.0	44
LASKOWSKI 7418DA1 SPOT 54	29	18.3	3.0	0.282645	0.000032	0.001460	0.282644	-4.9	1.1	-4.0	42
LASKOWSKI 7418DA1 SPOT 62	27	16.8	4.1	0.282679	0.000021	0.001060	0.282678	-3.7	0.7	-2.8	43
LASKOWSKI 7418DA1 SPOT 63	26	19.6	4.9	0.282632	0.000023	0.001639	0.282631	-5.4	0.8	-4.5	41
LASKOWSKI 7418DA2 SPOT 1	46	20.5	4.3	0.282672	0.000019	0.001717	0.282671	-4.0	0.7	-3.1	42
LASKOWSKI 7418DA2 SPOT 11	48	14.6	5.0	0.282643	0.000025	0.001118	0.282642	-5.0	0.9	-4.2	40
LASKOWSKI 7418DA2 SPOT 3	47	18.3	3.9	0.282727	0.000025	0.001111	0.282726	-2.1	0.9	-1.1	44
LASKOWSKI 7418DA2 SPOT 35	49	22.4	3.7	0.282704	0.000020	0.001390	0.282703	-2.9	0.7	-2.0	43
LASKOWSKI 7418DA2 SPOT 6	50	8.2	4.0	0.282624	0.000026	0.000676	0.282624	-5.7	0.9	-4.8	41
LASKOWSKI 7418DA3 SPOT 1_C	36	23.5	3.0	0.282673	0.000027	0.001412	0.282672	-3.9	1.0	-3.0	43
LASKOWSKI 7418DA3 SPOT 2	39	16.6	4.0	0.282734	0.000028	0.001229	0.282733	-1.8	1.0	-0.9	44
LASKOWSKI 7418DA3 SPOT 28	35	15.8	3.6	0.282684	0.000025	0.001047	0.282683	-3.6	0.9	-2.7	42
LASKOWSKI 7418DA3 SPOT 32	38	25.1	3.0	0.282643	0.000024	0.001950	0.282641	-5.0	0.8	-4.1	44
LASKOWSKI 7618DA1 SPOT 12	40	44.6	3.0	0.282576	0.000031	0.002399	0.282573	-7.4	1.1	-6.3	55
LASKOWSKI 7618DA1 SPOT 14	55	31.3	3.1	0.282720	0.000024	0.002078	0.282718	-2.3	0.9	-1.2	54
LASKOWSKI 7618DA1 SPOT 19	45	61.6	3.0	0.282589	0.000027	0.003455	0.282585	-6.9	1.0	-5.8	55
LASKOWSKI 7618DA1 SPOT 22	56	46.2	3.3	0.282640	0.000035	0.002576	0.282637	-5.1	1.2	-4.0	55
LASKOWSKI 7618DA1 SPOT 24	41	36.1	3.1	0.282655	0.000030	0.001761	0.282653	-4.6	1.1	-3.5	53
LASKOWSKI 7618DA1 SPOT 29	54	32.0	3.2	0.282703	0.000030	0.001926	0.282701	-2.9	1.1	-1.8	53
LASKOWSKI 7618DA1 SPOT 32	58	45.6	2.9	0.282697	0.000028	0.002619	0.282694	-3.1	1.0	-2.0	55
LASKOWSKI 7618DA1 SPOT 33	52	25.3	2.9	0.282670	0.000034	0.001434	0.282668	-4.1	1.2	-2.9	53
LASKOWSKI 7618DA1 SPOT 4	57	29.4	2.7	0.282706	0.000033	0.001681	0.282704	-2.8	1.2	-1.7	54
LASKOWSKI 7618DA1 SPOT 8	53	37.4	3.0	0.282679	0.000025	0.002185	0.282676	-3.8	0.9	-2.6	55
LASKOWSKI 7718DA1 SPOT 37	43	49.0	3.1	0.282566	0.000036	0.002778	0.282562	-7.8	1.3	-6.3	70
LASKOWSKI 7718DA1 SPOT 40	42	53.8	3.1	0.282548	0.000031	0.003081	0.282544	-8.4	1.1	-7.0	70
LASKOWSKI 7718DA1 SPOT 44	64	32.2	3.4	0.282687	0.000026	0.001781	0.282685	-3.5	0.9	-2.0	69
LASKOWSKI 7718DA1 SPOT 46	62	88.4	2.6	0.282718	0.000036	0.005421	0.282711	-2.4	1.3	-1.1	69
LASKOWSKI 7718DA1 SPOT 54	61	51.1	3.1	0.282661	0.000032	0.002992	0.282657	-4.4	1.1	-3.0	69
LASKOWSKI 7718DA1 SPOT 65	60	26.2	3.0	0.282645	0.000037	0.001613	0.282643	-4.9	1.3	-3.5	69
LASKOWSKI 7718DA1 SPOT 66	63	12.1	3.8	0.282594	0.000023	0.000788	0.282593	-6.7	0.8	-5.3	69
LASKOWSKI 7718DA1 SPOT 69	59	44.5	2.5	0.282688	0.000025	0.002490	0.282685	-3.4	0.9	-2.0	68
LASKOWSKI 7718DA2 SPOT 1	69	17.3	2.7	0.282733	0.000031	0.001161	0.282732	-1.8	1.1	-0.5	61
LASKOWSKI 7718DA2 SPOT 11	68	45.6	3.2	0.282572	0.000033	0.002607	0.282569	-7.5	1.2	-6.3	61
LASKOWSKI 7718DA2 SPOT 16	70	48.4	3.2	0.282684	0.000038	0.002662	0.282681	-3.6	1.3	-2.3	61
LASKOWSKI 7718DA2 SPOT 19	65	20.8	3.1	0.282660	0.000029	0.001233	0.282659	-4.4	1.0	-3.1	59
LASKOWSKI 7718DA2 SPOT 21	67	21.1	3.3	0.282690	0.000023	0.001394	0.282688	-3.4	0.8	-2.1	60
LASKOWSKI 7718DA2 SPOT 32	44	65.7	3.9	0.282689	0.000035	0.004032	0.282684	-3.4	1.2	-2.2	62
LASKOWSKI 7718DA2 SPOT 5	66	31.2	2.8	0.282643	0.000025	0.001911	0.282641	-5.0	0.9	-3.8	60

APPENDIX C

T/REE GEOCHEMISTRY DATA

Sample	Scan	Al	Si	P	Sc	Ti	Y	Nb	La	Ce	Pr	Nd	Sm	Eu	Gd	Tb	Dy	Ho	Er	Tm	Yb	Lu	Hf	Ta	Th	U	Ti-Temp	Crustal	Age	Age Error
7618DA1 Spot 2	2	1	153,230	311	3	11	3,326	9	0	36	1	8	12	2	66	26	263	98	394	79	620	133	9,333	2	817	261	746	34	54.5	0.8
7618DA1 Spot 3	4	0	153,230	219	3	10	2,311	5	0	28	0	6	10	1	50	19	194	73	288	58	426	95	9,418	1	520	269	737	37	55.8	0.7
7618DA1 Spot 5	5	1	153,230	246	3	9	2,899	8	0	33	1	7	10	1	54	21	225	86	346	70	529	116	9,864	2	717	312	733	35	54.4	0.5
7618DA1 Spot 6	7	2	153,230	269	3	11	2,927	7	0	29	1	6	11	2	59	22	229	89	346	70	540	119	8,850	2	631	244	753	35	54.6	0.6
7618DA1 Spot 7	9	0	153,230	139	3	9	1,446	3	0	18	0	4	6	1	29	11	112	42	174	35	262	61	10,049	1	206	188	733	41	53.8	0.6
7618DA1 Spot 9	11	1	153,230	166	3	10	1,739	4	0	20	0	4	8	1	37	14	135	51	205	41	291	73	9,921	1	282	200	742	40	53.7	0.7
7618DA1 Spot 10	12	2	153,230	187	3	10	1,954	4	0	21	0	5	8	1	38	15	163	60	238	49	353	82	9,475	1	332	237	744	38	54.8	0.6
7618DA1 Spot 11	14	1	153,230	257	3	10	2,821	7	0	35	1	6	11	1	57	21	221	81	322	64	498	108	9,652	2	600	261	737	35	55.0	0.8
7618DA1 Spot 13	15	2,044	153,230	150	3	8	1,288	4	0	15	0	3	5	1	25	9	101	37	152	33	227	57	7,409	1	225	181	723	42	54.6	0.6
7618DA1 Spot 15	17	0	153,230	119	3	6	1,155	3	0	19	0	2	5	1	22	8	93	34	142	29	221	51	11,137	1	179	168	704	41	54.0	0.6
7618DA1 Spot 16	19	367	153,230	195	3	10	662	2	1	11	0	2	2	0	11	4	49	20	85	18	147	33	9,670	1	97	86	738	50	55.2	0.6
7618DA1 Spot 18	20	1	153,230	214	3	13	2,024	6	0	19	0	4	6	1	33	14	154	59	245	50	398	85	8,837	1	379	208	767	37	54.8	0.8
7618DA1 Spot 20	21	1	153,230	229	3	12	2,527	6	0	26	0	6	9	1	50	19	198	76	309	62	459	103	9,444	1	488	231	754	36	53.8	0.7
7618DA1 Spot 21	23	1	153,230	334	3	12	3,600	10	0	35	1	8	12	2	70	26	284	106	415	83	666	138	9,118	2	914	294	755	33	54.9	0.8
7618DA1 Spot 23	25	1	153,230	221	3	11	2,523	6	0	25	0	6	9	1	46	19	189	72	290	58	434	100	9,053	1	478	204	748	37	55.0	0.7
7618DA1 Spot 25	27	0	153,230	236	4	8	2,727	7	0	36	1	7	10	1	48	19	204	78	332	67	508	111	10,636	2	683	319	720	35	54.3	0.7
7618DA1 Spot 26	28	1	153,230	280	3	7	1,851	5	0	26	0	4	6	1	34	14	140	54	224	47	356	83	9,515	1	379	277	707	38	54.7	0.8
7618DA1 Spot 27	30	1	153,230	133	3	8	1,273	3	0	18	0	3	5	1	24	10	106	39	161	32	243	58	10,283	1	255	160	718	42	55.0	0.9
7618DA1 Spot 28	31	0	153,230	196	3	11	2,105	5	0	22	0	5	9	1	42	16	166	65	254	51	375	86	9,398	1	327	259	748	38	53.5	0.7
7618DA1 Spot 30	33	111	153,230	169	3	6	1,874	4	0	26	0	5	8	1	34	13	142	57	229	46	333	79	9,431	1	383	275	691	39	56.0	0.7
7618DA1 Spot 31	35	1	153,230	150	4	13	1,505	3	0	15	0	5	7	1	33	13	124	46	178	38	263	65	9,146	1	189	163	765	41	54.2	0.8
7618DA1 Spot 34	37	1	153,230	236	3	7	2,181	5	0	32	0	6	10	1	45	17	178	66	264	54	415	91	9,997	1	483	276	715	39	55.6	0.7
7618DA1 Spot 35	39	1	153,230	300	3	14	3,061	8	0	26	1	7	11	2	62	24	235	88	360	71	550	117	8,882	2	666	210	770	35	54.0	0.5
7718DA1 Spot 36	41	500	153,230	68	3	5	607	15	0	8	0	0	1	0	9	4	46	19	82	18	151	34	11,114	4	97	300	676	45	69.6	0.6
7718DA1 Spot 38	42	1,400	153,230	1,162	4	10	3,079	38	0	44	2	26	70	4	249	74	467	121	397	71	505	108	6,924	6	864	571	740	38	68.4	0.9
7718DA1 Spot 39	43	433	153,230	190	3	9	439	7	2	18	1	2	2	0	7	3	32	13	66	15	138	35	9,034	2	139	217	728	52		
7718DA1 Spot 43	45	53	153,230	273	3	3	2,312	38	2	36	2	9	9	0	45	18	192	74	291	58	425	98	9,462	6	627	932	643	41	69.1	0.8
7718DA1 Spot 45	46	1	153,230	263	4	2	3,044	110	0	35	0	1	7	0	54	23	252	96	400	79	627	137	11,682	17	1,165	1,789	619	31	68.5	0.7
7718DA1 Spot 47	48	1	153,230	281	4	2	2,000	23	0	26	0	3	7	0	38	15	165	62	254	51	399	91	9,029	4	463	623	621	36	69.6	0.7
7718DA1 Spot 50	50	1,179	153,230	172	3	9	747	11	0	6	0	1	3	0	17	7	67	22	87	19	142	32	10,277	3	78	221	733	47	69.9	0.7
7718DA1 Spot 51	52	0	153,230	121	4	3	656	8	0	11	0	1	2	0	8	4	46	18	88	19	168	39	11,322	4	159	375	635	43	67.4	1.2
7718DA1 Spot 52	54	1,731	153,230	3,512	3	13	0	48	1	50	12	149	346	22	1,401	376	2,240	525	1,443	212	1,306	229	7,962	8	809	679	763	29	69.0	0.8
7718DA1 Spot 53	55	1,401	153,230	544	5	10	3,827	55	0	100	0	8	20	1	90	33	315	115	454	94	757	164	8,805	8	2,497	1,527	744	31	69.1	0.8
7718DA1 Spot 59	57	1	153,230	158	4	1	2,590	17	0	21	0	4	10	0	51	20	212	81	332	68	516	113	10,349	3	501	639	577	33	67.9	0.8
7718DA1 Spot 62	59	897	153,230	1,610	3	76	2,849	11	0	39	3	41	120	9	481	125	845	174	540	78	481	102	5,498	2	487	266	957	38	69.3	0.8
7718DA1 Spot 63	61	68	153,230	190	4	6	1,594	13	0	42	0	4	6	1	27	11	112	44	192	43	333	83	8,551	2	802	529	691	41	67.9	0.8
7718DA1 Spot 67	63	20	153,230	211	4	3	2,071	47	0	36	0	2	6	0	35	15	167	63	264	56	442	100	9,823	7	638	917	644	37	70.1	0.9
7718DA1 Spot 68	65	1	153,230	139	3	2	479	7	0	19	0	0	1	0	5	2	31	14	69	17	155	40	12,732	3	99	224	623	46	70.0	0.8
7718DA2 Spot 8	67	837	153,230	1,034	3	6	2,733	45	3	38	4	19	13	2	45	18	196	78	350	79	696	162	11,501	16	1,095	2,018	703	37	61.4	0.7
7718DA2 Spot 12	70	1	153,230	189	4	2	1,063	32	0	16	0	1	2	0	12	6	78	31	142	31	245	60	12,259	10	344	777	627	41	62.0	0.8
7718DA2 Spot 18	72	2	153,230	164	4	5	1,116	10	0	19	0	1	3	0	17	7	79	32	141	31	237	56	9,647	2	532	328	677	42	60.1	0.7
7718DA2 Spot 23	74	0	153,230	255	4	3	913	6	1	15	1	5	3	0	15	6	68	27	122	26	216	52	9,782	2	91	159	637	47	59.5	0.9
7718DA2 Spot 24	76	1	153,230	187	3	1	1,044	14	0	13	0	1	2	0	10	5	66	29	139	33	279	73	13,061	6	248	580	585	43	60.1	0.8
7718DA2 Spot 28	77	564	153,230	156	3	3	1,041	6	0	7	0	1	3	0	17	7	76	32	134	31	228	57	8,916	2	142	207	647	42	61.4	1.0
7718DA2 Spot 30	80	42	153,230	305	3	2	1,724	41	1	21	1	3	3	0	18	9	118	50	225	52	423	104	13,880	17	1,254	1,794	626	40	61.7	1.0
7718DA2 Spot 31	82	6	153,230	118	3	2	743	9	0	10	0	0	1	0	8	4	48	21	101	24	211	52	11,255	4	270	543	607	42	61.7	0.7

Sample	Scan	Al	Si	P	Sc	Ti	Y	Nb	La	Ce	Pr	Nd	Sm	Eu	Gd	Tb	Dy	Ho	Er	Tm	Yb	Lu	Hf	Ta	Th	U	Ti-Temp	Crustal	Age	Age Error
7318DA2 Spot 1	85	2	153,230	155	4	10	683	6	0	15	0	1	2	0	12	5	53	20	90	19	157	36	10,700	2	158	230	739	44	103.5	1.4
7318DA2 Spot 2	87	2	153,230	283	4	10	2,022	8	1	20	1	7	9	1	43	16	163	59	245	49	347	83	9,516	2	311	353	745	42	102.2	1.4
7318DA2 Spot 4	88	4	153,230	211	3	9	1,383	8	1	15	1	4	5	1	27	11	110	42	170	35	255	66	8,219	2	235	307	730	45	103.8	1.7
7318DA2 Spot 5	90	4	153,230	197	4	7	1,374	10	0	36	0	2	5	0	24	10	100	38	166	36	279	66	13,521	6	705	651	713	41	106.4	1.6
7318DA2 Spot 6	92	1	153,230	328	4	13	2,277	18	0	47	0	5	10	2	49	18	182	69	273	56	416	94	10,377	4	1,244	396	763	38	102.9	1.2
7318DA2 Spot 7	94	67	153,230	285	3	5	1,209	6	1	26	1	5	5	0	21	8	88	35	145	32	237	58	10,561	2	310	377	690	46	104.0	1.1
7318DA2 Spot 11	96	0	153,230	152	3	9	1,461	5	0	16	0	4	6	1	32	12	121	44	182	35	267	64	8,877	1	220	256	733	40	103.6	1.1
7318DA2 Spot 12	97	3	153,230	171	3	10	1,612	5	0	20	0	3	7	1	34	13	127	48	189	39	284	67	10,286	2	274	294	738	40	103.8	1.2
7318DA2 Spot 14	99	2	153,230	161	4	10	1,060	4	0	15	0	3	4	1	21	8	81	31	136	28	214	50	10,467	1	160	194	742	46	104.8	1.5
7318DA2 Spot 15	100	2	153,230	224	4	14	1,177	9	0	15	0	2	4	1	20	8	87	33	142	30	224	54	9,485	2	359	321	770	44	106.7	1.6
7318DA2 Spot 17	102	3	153,230	174	3	8	1,635	6	0	19	0	4	8	1	38	14	139	51	207	41	284	71	8,850	2	277	312	721	40	105.1	1.2
7318DA2 Spot 18	104	5	153,230	117	4	9	586	4	0	12	0	1	2	0	10	4	44	17	76	17	142	31	11,850	1	104	163	730	46	101.9	1.1
7318DA2 Spot 20	105	0	153,230	142	4	9	1,378	4	0	11	0	4	7	1	30	11	113	42	170	33	253	58	9,441	1	183	235	733	41	104.8	1.3
7318DA2 Spot 21	107	55	153,230	184	3	20	1,473	6	0	16	0	3	6	1	32	12	118	46	185	38	276	64	11,147	2	290	240	806	41	108.9	1.4
7318DA2 Spot 24	109	212	153,230	527	3	11	2,031	15	3	59	3	15	11	2	47	17	159	61	241	49	334	82	8,237	3	938	353	751	44	103.7	1.1
7318DA2 Spot 25	110	0	153,230	268	4	11	2,025	17	0	48	0	4	8	1	42	16	162	62	246	49	352	87	8,574	4	895	395	750	40	103.6	1.4
7318DA2 Spot 26	112	1	153,230	207	4	9	1,379	10	0	26	0	2	5	1	24	9	102	39	167	34	256	60	11,083	3	417	382	728	40	101.9	1.3
7318DA2 Spot 27	113	0	153,230	154	4	5	933	7	0	18	0	1	2	0	13	5	65	26	122	26	215	53	12,110	3	203	372	686	41	107.0	1.7
7318DA2 Spot 29	115	4	153,230	147	4	10	998	3	0	10	0	2	4	1	21	8	78	31	122	25	197	45	10,226	1	126	163	738	42	103.1	1.4
7318DA2 Spot 30	117	20	153,230	246	3	11	787	5	1	15	1	3	3	1	15	5	59	23	94	20	160	37	8,534	1	166	219	746	50	103.4	1.3
7318DA2 Spot 33	118	64	153,230	153	3	11	553	4	0	9	0	1	2	0	10	4	42	17	75	16	133	30	8,812	1	126	179	749	49	103.0	1.1
7318DA2 Spot 35	119	0	153,230	174	4	9	1,663	6	0	20	0	4	7	1	34	13	136	51	200	41	303	71	10,230	2	275	324	729	41	104.6	1.4
7418DA1 Spot 36	121	0	153,230	195	4	12	1,076	10	0	56	0	5	7	2	25	8	81	30	129	28	220	52	9,802	3	671	498	755	43	42.4	0.5
7418DA1 Spot 37	123	264	153,230	2,882	4	5	926	12	57	373	31	102	20	1	28	8	74	27	120	25	215	51	11,308	4	1,152	2,052	684	51	42.8	0.4
7418DA1 Spot 40	124	230	153,230	1,250	3	9	564	12	23	167	13	41	9	1	13	4	41	16	72	16	135	31	9,911	4	733	1,056	733	54	42.1	0.5
7418DA1 Spot 42	126	2	153,230	108	4	7	705	8	0	43	0	3	4	1	14	5	52	20	91	20	178	43	11,346	3	579	761	709	44	41.6	0.6
7418DA1 Spot 43	127	9	153,230	119	3	9	603	8	0	27	0	2	3	1	12	4	47	17	78	18	149	36	9,526	2	197	386	732	46	42.3	0.8
7418DA1 Spot 61	128	793	153,230	514	3	17	444	9	12	91	6	20	5	1	10	4	36	13	61	14	124	31	11,505	3	382	730	791	55	42.4	0.6
7418DA2 Spot 2	130	1	153,230	113	3	9	559	10	0	45	0	1	2	0	11	4	40	15	72	15	140	32	9,396	3	575	565	729	46	42.8	0.5
7418DA2 Spot 4	132	1	153,230	44	5	2	812	30	0	43	0	1	1	0	6	3	36	18	111	33	381	121	15,447	7	712	6,524	615	37	37.8	0.5
7418DA2 Spot 5	134	3	153,230	156	3	5	1,085	13	0	75	1	7	11	3	38	13	110	38	151	32	247	59	9,867	3	1,214	631	683	43	43.9	0.6
7418DA2 Spot 7	136	14	153,230	64	4	6	361	14	0	35	0	1	1	0	5	3	33	13	69	19	179	44	9,245	5	331	1,048	691	47	38.4	0.5
7418DA2 Spot 20	138	19	153,230	56	4	2	287	64	4	34	2	5	1	0	2	1	15	8	51	17	239	72	14,289	26	927	1,599	624	47	41.0	0.5

APPENDIX D

ZHE THERMOCHRONOLOGY DATA

Sample Name	sample/ run type	He date	pmol He	1s ± pmol He	% 1s ± He	U+Th date	(238/233)m	(238/233)m 1s ±	(232/229)m	(232/229)m 1s ±	(91/90)m	(91/90)m 1s ±
19C207_7318DA2_Zr1	zirc	11/5/19	0.134067557	0.000295244	0.220220543	2/6/20	0.844005	0.006347	0.750853	0.001529	0.055808	0.000142
19C208_7318DA2_Zr2	zirc	11/5/19	0.08004516	0.000181742	0.227048723	2/6/20	0.679631	0.0039	0.801045	0.001196	0.044779	0.000447
19C209_7318DA2_Zr3	zirc	11/5/19	0.069677298	0.000155957	0.223826872	2/6/20	0.614574	0.004515	0.605756	0.004222	0.044882	0.000366
19C210_7318DA2_Zr4	zirc	11/5/19	0.053075207	0.000120638	0.227297023	2/6/20	0.460755	0.003402	0.540889	0.001147	0.036218	0.000182
19C211_7318DA2_Zr5	zirc	11/6/19	0.325274672	0.000921093	0.283174025	2/6/20	2.04982	0.014571	2.552074	0.009577	0.054562	0.000122
19C212_7318DA1_Zr1	zirc	11/6/19	0.199586315	0.000549602	0.275370457	2/6/20	4.796601	0.030749	3.446023	0.018821	0.103074	0.00012
19C213_7318DA1_Zr2	zirc	11/6/19	0.070870814	0.000199974	0.282167182	2/6/20	1.526616	0.003299	1.1424	0.00803	0.062281	0.000154
19C214_7318DA1_Zr3	zirc	11/6/19	0.013080565	4.30001E-05	0.328732447	2/6/20	0.429035	0.002283	0.386909	0.001642	0.043943	0.000115
19C215_7318DA1_Zr4	zirc	11/6/19	0.048325263	0.000139748	0.289182104	2/6/20	1.270721	0.002589	0.844586	0.002881	0.083133	0.000293
19C216_7318DA1_Zr5	zirc	11/6/19	0.027892867	7.93504E-05	0.284482687	2/6/20	0.799312	0.006152	0.473412	0.003185	0.043977	0.000094
19C217_7218DA2_Zr1	zirc	11/7/19	0.39949672	0.001051019	0.263085842	2/6/20	5.424133	0.022061	3.077822	0.014886	0.092046	0.001312
19C218_7218DA2_Zr2	zirc	11/7/19	0.047678278	0.000127495	0.267406111	2/6/20	0.570069	0.002449	0.350466	0.002492	0.038116	0.000139
19C20_7218DA2_Zr3	zirc	11/7/19	0.021907559	6.88333E-05	0.314198741	2/6/20	0.429041	0.003302	0.310623	0.00259	0.046311	0.000169
19C21_7218DA2_Zr4	zirc	11/7/19	0.071649826	0.00019421	0.271054511	2/6/20	1.083751	0.007384	0.580197	0.00348	0.034935	0.000337
19C22_7218DA2_Zr5	zirc	11/13/19	0.060697123	0.000156379	0.257638141	2/6/20	0.896033	0.003648	0.753107	0.004157	0.0416	0.000068
19C206_MS19_FCTjm_Zr3	zirc	11/5/19	0.388252187	0.000866272	0.223121046	2/6/20	2.94117	0.014064	2.018604	0.00851	0.094278	0.00011
19C219_MS19_FCTjm_Zr4	zirc	11/7/19	0.300431839	0.000781019	0.259965523	2/6/20	2.523115	0.006364	1.793719	0.006239	0.060684	0.000377
Nbblk						2/6/20	0.003366	0.000115	0.002352	0.000147	0.006965	0.000026
BB5						2/6/20	0.004956	0.002195	0.002456	0.001207	0.007106	0.000071
19C223_7718DA1_Zr1	zirc	1/13/20	0.000937759	1.83074E-05	1.95224502	2/25/20	0.950543	0.003906	0.646059	0.003189	0.035283	0.000274
19C224_7718DA1_Zr2	zirc	1/13/20	0.005763883	4.61638E-05	0.800915294	2/25/20	1.658736	0.003905	1.01768	0.002971	0.056835	0.000415
19C225_7718DA1_Zr3	zirc	1/14/20	0.002164823	1.54046E-05	0.711587968	2/25/20	2.506721	0.008004	1.619939	0.005728	0.057152	0.000423
19C226_7718DA1_Zr4	zirc	1/14/20	0.126071264	0.000423168	0.33565764	2/25/20	0.779651	0.002093	0.949065	0.004112	0.080758	0.000984
19C226a_7718DA1_Zr5	zirc	1/14/20	0.228317885	0.000759928	0.332837635	2/25/20	1.685585	0.007448	1.235001	0.004928	0.067163	0.000249
19C227_7718DA2_Zr1	zirc	1/15/20	0.151218659	0.000371168	0.245451034	2/25/20	2.051473	0.006147	1.137449	0.002897	0.08386	0.000487
19C228_7718DA2_Zr2	zirc	1/15/20	0.30323347	0.000733931	0.242034979	2/25/20	5.534519	0.011363	3.090499	0.010362	0.045228	0.00028
19C229_7718DA2_Zr3	zirc	1/15/20	0.110592249	0.00027751	0.250931006	2/25/20	1.829149	0.008975	1.077002	0.003747	0.037903	0.000091
19C229_7718DA2_Zr4	Packet lost											
19C232_7718DA2_Zr5	zirc	1/15/20	0.100960101	0.000259562	0.257093981	2/25/20	1.424134	0.003645	0.858369	0.003483	0.040877	0.000308
19C233_7418DA1_Zr1	zirc	1/15/20	0.52881291	0.001306303	0.247025576	2/25/20	12.661065	0.027799	4.46836	0.012226	0.079214	0.000095
19C234_7418DA1_Zr2	zirc	1/27/20	0.026208023	0.000333744	1.273441287	2/25/20	4.178148	0.00951	1.236247	0.003729	0.03724	0.000348
19C235_7418DA1_Zr3	zirc	1/27/20	0.089366084	0.00113651	1.271746682	2/25/20	0.967991	0.001353	0.470656	0.00268	0.035546	0.000259
19C236_7418DA1_Zr4	zirc	1/27/20	0.037976882	0.000496635	1.307728577	2/25/20	1.009747	0.001893	0.945776	0.002189	0.032312	0.000125
19C237_7418DA1_Zr5	zirc	1/28/20	0.235317667	0.000265272	0.112729364	2/25/20	10.605316	0.039773	0.84808	0.0029	0.030731	0.000243
19C238_7618DA1_Zr1	zirc	1/28/20	0.080089102	8.3012E-05	0.103649577	2/25/20	1.047099	0.007438	1.443433	0.006103	0.077147	0.000527
19C239_7618DA1_Zr2	zirc	1/28/20	0.139518219	0.000147978	0.106063869	2/25/20	2.418583	0.004862	2.85348	0.006345	0.092807	0.000382
19C240_7618DA1_Zr3	zirc	1/28/20	0.191975665	0.000198482	0.103389343	2/25/20	2.873263	0.004275	3.445296	0.011998	0.093686	0.000805
19C241_7618DA1_Zr4	zirc	1/28/20	0.259037018	0.000251269	0.097001226	2/25/20	3.773708	0.00765	4.898341	0.011411	0.102747	0.001067
19C242_7618DA1_Zr5	zirc	1/29/20	0.251179447	0.000551105	0.219406857	2/25/20	4.258363	0.018619	6.344963	0.013498	0.06773	0.000756
19C231_MS19_FCTjm_Zr25	zirc	1/15/20	0.160819721	0.000388172	0.241371151	2/25/20	1.251296	0.007283	0.586993	0.002705	0.057817	0.000191
19C243_MS19_FCTjm_Zr6	zirc	1/29/20	0.204645155	0.000460774	0.225157691	2/25/20	1.585038	0.009231	0.980412	0.003645	0.065106	0.000523
BB1						2/25/20	0.004548	0.001527	0.002421	0.000962	0.007268	0.000097
BB9						2/25/20	0.003926	0.000098	0.002067	0.000089	0.007175	0.000054
BB10						2/25/20	0.004656	0.000351	0.002901	0.000334	0.007168	0.000045

Sample Name	ng U	1s ± ng U	% 1s ± ng U	ng Th	1s ± ng Th	% 1s ± ng Th	ng Zr	1s ± ng Zr	% 1s ± ng Zr	Th/U	raw date (Ma)	1s ± date (Ma)	1s ± date %
19C207_7318DA2_Zr1	0.811214811	0.011861219	1.462155161	0.803275314	0.011437244	1.423826159	1208.697086	19.37102991	1.602637265	1.015834459	24.79833047	0.295971572	1.193514107
19C208_7318DA2_Zr2	0.652611937	0.009435747	1.44584346	0.857072898	0.012191616	1.422471243	876.2613434	15.06198192	1.718891519	1.347277759	17.33874237	0.197190414	1.137282103
19C209_7318DA2_Zr3	0.589839071	0.008614685	1.460514487	0.647755149	0.009423877	1.454851807	879.1701095	14.75532198	1.67832389	1.126605142	17.37535927	0.204578618	1.177406552
19C210_7318DA2_Zr4	0.441420614	0.006449495	1.461076941	0.578228374	0.008234512	1.42409346	646.0130142	10.50553845	1.626211581	1.343820247	17.00797642	0.195299302	1.14828065
19C211_7318DA2_Zr5	1.974693975	0.028787302	1.457810781	2.73388853	0.039115703	1.430771681	1168.893174	18.70868835	1.600547317	1.420284651	22.97966765	0.264416763	1.150655295
19C212_7318DA1_Zr1	4.625036242	0.067120716	1.45124736	3.692055104	0.053229888	1.441741433	3355.569958	53.58582676	1.596921758	0.818931216	6.733078093	0.082672608	1.227857552
19C213_7318DA1_Zr2	1.469859525	0.020958892	1.425911194	1.22294942	0.017797965	1.455331273	1425.724585	22.84828571	1.602573593	0.853546245	7.472182739	0.090007578	1.20456875
19C214_7318DA1_Zr3	0.410814295	0.005927275	1.442811193	0.413187092	0.005923692	1.43365856	852.7796389	13.66697639	1.602638685	1.03180016	4.771109158	0.057268728	1.20032316
19C215_7318DA1_Zr4	1.222948928	0.017433785	1.425553017	0.903741702	0.012915275	1.429089164	2266.4216	36.62999229	1.616203811	0.758106803	6.239547716	0.076207656	1.221365069
19C216_7318DA1_Zr5	0.76809097	0.01124506	1.464027049	0.505904108	0.007348853	1.452617824	853.7302372	13.65699112	1.599684599	0.675693806	5.828937771	0.073831495	1.266637215
19C217_7218DA2_Zr1	5.230535765	0.075016514	1.434203246	3.297404077	0.047392516	1.437267452	2710.638836	53.35182899	1.968238198	0.646726097	12.32431483	0.153316183	1.244013847
19C218_7218DA2_Zr2	0.546896629	0.007852051	1.435746814	0.374126179	0.005448736	1.456389885	695.1697731	11.19846042	1.610895763	0.70179011	13.91124564	0.171972534	1.23621233
19C20_7218DA2_Zr3	0.410820084	0.006016082	1.464408062	0.331421024	0.004870327	1.469528633	919.8856483	14.82042954	1.611116508	0.827604378	8.305227525	0.10354541	1.246749824
19C21_7218DA2_Zr4	1.042543394	0.01516992	1.455087633	0.620360097	0.008971214	1.446130048	613.3614431	10.49176993	1.710536266	0.610441578	11.17230805	0.141886022	1.269979505
19C22_7218DA2_Zr5	0.861416122	0.012355526	1.434327259	0.805691232	0.011620184	1.44226272	788.154571	12.58858408	1.597222746	0.959511167	10.69773223	0.127129201	1.188375242
19C206_MS19_FCTjm_Zr3	2.834748919	0.040781518	1.438628945	2.162096267	0.03099054	1.433356163	2831.894624	45.21195037	1.596526579	0.782446803	21.4960356	0.261182496	1.215026347
19C219_MS19_FCTjm_Zr4	2.431371716	0.034697816	1.427088099	1.921056465	0.027459355	1.429388246	1370.521376	22.59063486	1.648324152	0.810556255	19.29074678	0.233047379	1.208078574
Nbblk	9.04172E-05	9.47128E-05	104.7507776	0.001005119	9.10691E-05	9.060532399	0.176650854	0.266112681	150.6433031	11.40408645			
BB5	0.001624593	0.000950878	58.53025569	0.00111659	0.000581473	52.07583518	2.860034928	0.624222569	21.82569742	0.70508822			
19C223_7718DA1_Zr1	0.921821086	0.01326507	1.439006994	0.687574432	0.009946262	1.446572469	642.4294383	10.40655186	1.619874688	0.765186805	0.160489499	0.003674393	2.289491401
19C224_7718DA1_Zr2	1.610519882	0.023047142	1.431037411	1.083804411	0.015558305	1.435526971	1287.997656	20.78206772	1.613517511	0.690365715	0.573028605	0.008283523	1.445568792
19C225_7718DA1_Zr3	2.435162668	0.034927166	1.434284701	1.725945385	0.024824174	1.438294283	1298.783463	20.98466742	1.615717171	0.72709886	0.141307019	0.00197025	1.394304494
19C226_7718DA1_Zr4	0.755633176	0.010822497	1.432242151	1.010645682	0.014580265	1.442668268	2241.89678	40.14868037	1.790835364	1.372089053	23.47149369	0.270871283	1.154043653
19C226a_7718DA1_Zr5	1.636629818	0.023580642	1.440804885	1.315516546	0.018952371	1.440679016	1662.715004	25.92196238	1.559014162	0.824594146	21.7155511	0.268094432	1.234573469
19C227_7718DA2_Zr1	1.992446135	0.028560486	1.433438299	1.21150459	0.017374225	1.434103081	2390.490311	38.26093213	1.600547467	0.62378204	12.30341448	0.153086235	1.24425813
19C228_7718DA2_Zr2	5.379615433	0.076933615	1.430095065	3.293886803	0.047346649	1.437409709	920.3178513	14.63175525	1.589858898	0.628133319	9.13204105	0.113211803	1.239720695
19C229_7718DA2_Zr3	1.776241977	0.02564831	1.443964887	1.147054751	0.016494924	1.438024084	712.6624951	11.02367179	1.54682923	0.662485551	10.01676774	0.124816424	1.246074851
19C229_7718DA2_Zr4													
19C232_7718DA2_Zr5	1.382375697	0.019792146	1.431748672	0.913943735	0.013170548	1.4410677	794.9018231	12.82897109	1.613906362	0.678246813	11.71103193	0.144595613	1.234695743
19C233_7418DA1_Zr1	12.30999126	0.176096466	1.430516581	4.762990635	0.068338981	1.434791426	2170.409914	33.41701287	1.539663667	0.39693224	7.30190484	0.094255785	1.290838312
19C234_7418DA1_Zr2	4.060580827	0.058097661	1.430772174	1.316845057	0.018908915	1.435925554	694.697443	11.48812912	1.653688126	0.332690891	1.112838476	0.020111729	1.807246016
19C235_7418DA1_Zr3	0.9387888	0.013410915	1.428533818	0.500556134	0.007269022	1.452189208	649.3885127	10.45742945	1.610350237	0.546989865	15.67050139	0.277697159	1.772101302
19C236_7418DA1_Zr4	0.979395396	0.014001731	1.429630103	1.007138882	0.01443548	1.433315763	565.1843146	8.821663274	1.560847151	1.054934988	5.784831507	0.100427695	1.736052202
19C237_7418DA1_Zr5	10.31083021	0.148163276	1.436967474	0.902973391	0.012982442	1.437743608	525.0775404	8.53919775	1.626273663	0.089841234	4.15065547	0.056439656	1.359776942
19C238_7618DA1_Zr1	1.015719219	0.014852439	1.46225833	1.537751045	0.02217489	1.442033837	2077.160412	33.60249784	1.617713184	1.553126223	10.76132793	0.119284903	1.10845895
19C239_7618DA1_Zr2	2.349450815	0.03359665	1.429978864	3.041172254	0.043580574	1.433018928	2860.297292	44.99905229	1.573229902	1.327911261	8.429232805	0.09361553	1.110605584
19C240_7618DA1_Zr3	2.791614982	0.039883698	1.428696217	3.672178686	0.052806865	1.438025487	2910.099635	49.21741297	1.691262126	1.349468268	9.723358179	0.107678614	1.107422067
19C241_7618DA1_Zr4	3.667273719	0.052442853	1.430022882	5.22144525	0.074841812	1.43335433	3467.724558	61.99572407	1.78779263	1.460635306	9.7951109	0.107266364	1.095101072
19C242_7618DA1_Zr5	4.138587774	0.059616012	1.440491676	6.763863479	0.096907546	1.432724745	1684.777481	29.07115854	1.725519178	1.676629312	8.114226168	0.089131039	1.098453959
19C231_MS19_FCTjm_Zr25	1.214295353	0.017616909	1.450792779	0.624597044	0.00902172	1.444406466	1321.548484	20.52985645	1.553469789	0.527679209	21.87691476	0.279822994	1.279078871
19C243_MS19_FCTjm_Zr6	1.538850543	0.022325585	1.450796187	1.0440685	0.015026479	1.439223504	1584.048272	25.90107011	1.635118738	0.696028372	21.23177325	0.263552972	1.241313992
BB1	0.00186619	0.000667816	35.78496861	0.001314314	0.000459967	34.99677273	0.579566213	1.007802061	173.8890293	0.722499713			
BB9	0.001261312	7.98968E-05	6.334422194	0.000936872	5.27596E-05	5.631458874	-1.267177544	0.709085747	-55.95788454	0.761995189			
BB10	0.001971217	0.000168335	8.539657716	0.0018261	0.000163856	8.972984635	-1.406113856	0.657757744	-46.77841282	0.950351952			

Sample Name	morph comments	Ft 238U	Ft 235U	Ft 232Th	Ft 147Sm	Rs (um)	corr date (Ma)	1s ± date (Ma)	1s ± date %
19C207_7318DA2_Zr1	Euhedral grain, no inclusions or bubbles. Both tips intact	0.746	0.710	0.710	0.919	47.29	33.56	0.40	1.20
19C208_7318DA2_Zr2	Euhedral grain, no inclusions or bubbles. Both tips intact	0.697	0.655	0.655	0.902	38.91	**25.27**	0.29	1.15
19C209_7318DA2_Zr3	Euhedral grain, some scratches and small bubbles. One tip slightly flattened	0.729	0.691	0.691	0.913	44.01	24.12	0.29	1.19
19C210_7318DA2_Zr4	Euhedral grain, one bubble, no inclusions. Both tips intact	0.710	0.670	0.670	0.907	40.92	24.29	0.28	1.16
19C211_7318DA2_Zr5	Euhedral grain, some scratches and small bubbles. One tip slightly flattened	0.727	0.688	0.688	0.913	43.60	32.07	0.37	1.16
							27.9	**0.3**	
19C212_7318DA1_Zr1	Euhedral grain, some bubbles, no inclusions. Both tips intact	0.794	0.763	0.763	0.935	59.03	8.54	0.11	1.23
19C213_7318DA1_Zr2	Euhedral grain, some bubbles, no inclusions. Both tips intact, one slightly rounded	0.751	0.715	0.715	0.921	48.15	10.05	0.12	1.21
19C214_7318DA1_Zr3	Sub to Euhedral grain, oone tip intact, one flattened	0.700	0.658	0.658	0.903	39.35	6.91	0.08	1.21
19C215_7318DA1_Zr4	Euhedral grain, no inclusions or bubbles. Both tips intact, one slightly rounded	0.768	0.735	0.735	0.927	52.18	8.18	0.10	1.23
19C216_7318DA1_Zr5	Euhedral Grain, one small inclusioon, some bubbles. Both tips intact.	0.720	0.680	0.680	0.910	42.39	8.17	0.10	1.28
							8.4	**0.1**	
19C217_7218DA2_Zr1	Euhedral grain, some hazeyness at one end, few cracks/inclusions, both tips intact.	0.794	0.764	0.764	0.935	59.08	15.62	0.20	1.25
19C218_7218DA2_Zr2	Euhedral grain, one small inclusioon, some bubbles. Both tips intact.	0.703	0.661	0.661	0.904	39.75	19.99	0.25	1.25
19C20_7218DA2_Zr3	Euhedral grain, a few small bubbles, no inclusions. Both tips intact.	0.703	0.662	0.662	0.904	39.80	11.95	0.15	1.26
19C21_7218DA2_Zr4	Eu-subhedral grain, a few small bubbles and inclusions. One tip broken off.	0.688	0.645	0.645	0.899	37.73	16.38	0.21	1.28
19C22_7218DA2_Zr5	Eu-subhedral grain, no bubbles, a few small inclusions. One tip slightly fractured.	0.694	0.652	0.652	0.901	38.52	15.61	0.19	1.20
							15.9	**0.2**	
19C206_MS19_FCTjm_Zr3	nice edges, abraded, some string like inclusions	0.794	0.764	0.764	0.935	59.13	27.25	0.33	1.22
19C219_MS19_FCTjm_Zr4	slightly rounded edges, strawlike inclusions, some abrasions	0.767	0.733	0.733	0.926	51.71	25.37	0.31	1.22
Nbblk									
BB5									
19C223_7718DA1_Zr1	Euhedral grain, a few medium bubbles, some small inclusions. One tip rounded.	0.706	0.665	0.665	0.906	40.25	~~0.23~~	~~0.01~~	2.30
19C224_7718DA1_Zr2	Euhedral grain, a few medium bubbles/inclusions. Slightly squared tips.	0.741	0.704	0.704	0.917	46.26	~~0.78~~	~~0.01~~	1.45
19C225_7718DA1_Zr3	Euhedral grain, a few medium bubbles/inclusions. One tip slightly broken.	0.735	0.697	0.697	0.915	45.01	~~0.19~~	~~0.00~~	1.40
19C226_7718DA1_Zr4	Euhedral grain, no bubbles, a few small inclusions. Both tips intact.	0.775	0.742	0.742	0.929	53.82	30.62	0.36	1.16
19C226a_7718DA1_Zr5	Euhedral grain, no bubbles, a few small inclusions. One inclusion on edge of crystal Both tips intact.	0.758	0.723	0.723	0.923	49.69	28.90	0.36	1.24
							29.8	**0.4**	
19C227_7718DA2_Zr1	Euhedral grain, a few small bubbles, several small/medium inclusions. Both tips intact.	0.762	0.728	0.728	0.924	50.69	16.25	0.20	1.25
19C228_7718DA2_Zr2	Euhedral grain, no bubbles, a few small inclusions. Both tips intact.	0.722	0.683	0.683	0.911	42.78	12.76	0.16	1.25
19C229_7718DA2_Zr3	Eu-subhedral grain, a few small bubbles. One small central inclusion. Both tips intact.	0.715	0.675	0.675	0.908	41.60	14.14	0.18	1.26
19C229_7718DA2_Zr4	Euhedral grain, no bubbles, a few medium inclusions. Both tips intact.	0.760	0.726	0.726	0.924	50.28			
19C232_7718DA2_Zr5	Subhedral grain, no bubbles, no inclusions. Both tips intact.	0.717	0.677	0.677	0.909	41.96	16.48	0.21	1.24
							14.9	**0.2**	
19C233_7418DA1_Zr1	Subhedral grain, small bubbles and inclusions. Both tips intact.	0.781	0.749	0.749	0.931	55.46	9.39	0.12	1.30
19C234_7418DA1_Zr2	Euhedral grain, no bubbles, a few small inclusions. Both tips intact.	0.693	0.651	0.651	0.901	38.35	1.62	0.03	1.81
19C235_7418DA1_Zr3	Euhedral grain, no bubbles, a few medium inclusions. Both tips intact.	0.691	0.649	0.649	0.900	38.14	22.86	0.41	1.78
19C236_7418DA1_Zr4	Euhedral grain, two small inclusions, no bubbles. One tip slightly fractured.	0.675	0.631	0.631	0.895	36.03	8.70	0.15	1.74
19C237_7418DA1_Zr5	Euhedral grain, no bubbles or inclusions. Some cracking. Both tips intact.	0.683	0.639	0.639	0.897	36.96	6.10	0.08	1.36
							9.7	**0.2**	
19C238_7618DA1_Zr1	Euhedral grain, no bubbles, a few medium inclusions. One tip broken off.	0.783	0.752	0.752	0.932	56.07	13.90	0.16	1.12
19C239_7618DA1_Zr2	Euhedral grain, no bubbles, a few small inclusions. Both tips intact.	0.792	0.761	0.761	0.934	58.44	10.75	0.12	1.12
19C240_7618DA1_Zr3	Euhedral grain, several small inclsuions. One tip slightly broken	0.783	0.751	0.751	0.931	55.91	12.55	0.14	1.12
19C241_7618DA1_Zr4	Euhedral grain, some bubbles, no inclusions, both tips fractured and missing chunks.	0.812	0.785	0.785	0.941	65.32	12.17	0.13	1.10
19C242_7618DA1_Zr5	Euhedral grain, no bubbles or inclusions. Some cracking. One tip missing chunk.	0.773	0.740	0.740	0.928	53.29	10.63	0.12	1.11
							12.0	**0.1**	
19C231_MS19_FCTjm_Zr25	sharp edges, mostly clear, some small abrasions, possibly small inclusions	0.730	0.692	0.692	0.914	44.13	30.18	0.39	1.29
19C243_MS19_FCTjm_Zr6	slightly abraded, some large inclusions, one side slightly rounded	0.747	0.711	0.711	0.919	47.39	28.65	0.36	1.25
BB1									
BB9									
BB10									

Sample Name	ppm eU (Zr)	ppm eU (morph)	ppm U (morph)	d ppm U (morph)	ppm Th (morph)	d ppm Th (morph)	nmol 4He/g (morph)	d nmol 4He/g (morph)
19C207_7318DA2_Zr1	411.72	302.43	245.34	3.59	242.94	3.46	40.55	0.09
19C208_7318DA2_Zr2	485.02	459.40	351.06	5.08	461.04	6.56	43.06	0.10
19C209_7318DA2_Zr3	420.04	291.20	231.46	3.38	254.19	3.70	27.34	0.06
19C210_7318DA2_Zr4	444.72	286.06	218.73	3.20	286.51	4.08	26.30	0.06
19C211_7318DA2_Zr5	1114.24	1081.59	816.08	11.90	1129.83	16.17	134.43	0.38
19C212_7318DA1_Zr1	814.59	634.68	534.42	7.76	426.62	6.15	23.06	0.06
19C213_7318DA1_Zr2	613.37	473.07	395.70	5.64	329.23	4.79	19.08	0.05
19C214_7318DA1_Zr3	296.40	268.35	217.05	3.13	218.30	3.13	6.91	0.02
19C215_7318DA1_Zr4	315.16	271.13	231.01	3.29	170.71	2.44	9.13	0.03
19C216_7318DA1_Zr5	517.03	364.57	315.71	4.62	207.94	3.02	11.46	0.03
19C217_7218DA2_Zr1	1102.54	849.76	740.12	10.61	466.58	6.71	56.53	0.15
19C218_7218DA2_Zr2	454.44	317.91	273.88	3.93	187.36	2.73	23.88	0.06
19C20_7218DA2_Zr3	264.38	228.51	192.09	2.81	154.96	2.28	10.24	0.03
19C21_7218DA2_Zr4	964.14	664.04	582.57	8.48	346.66	5.01	40.04	0.11
19C22_7218DA2_Zr5	663.46	518.92	425.42	6.10	397.90	5.74	29.98	0.08
19C206_MS19_FCTjm_Zr3	587.44	431.16	365.62	5.26	278.87	4.00	50.08	0.11
19C219_MS19_FCTjm_Zr4	1046.78	545.87	460.38	6.57	363.75	5.20	56.89	0.15
Nbblk								
BB5								
19C223_7718DA1_Zr1	839.24	510.47	434.34	6.25	323.97	4.69	0.44	0.01
19C224_7718DA1_Zr2	720.67	518.07	447.33	6.40	301.03	4.32	1.60	0.01
19C225_7718DA1_Zr3	1088.48	845.88	725.11	10.40	513.93	7.39	0.64	0.00
19C226_7718DA1_Zr4	220.45	166.84	126.94	1.82	169.78	2.45	21.18	0.07
19C226a_7718DA1_Zr5	582.37	485.04	407.98	5.88	327.93	4.72	56.91	0.19
19C227_7718DA2_Zr1	474.05	405.25	354.58	5.08	215.60	3.09	26.91	0.07
19C228_7718DA2_Zr2	3327.51	2401.93	2099.79	30.03	1285.68	18.48	118.36	0.29
19C229_7718DA2_Zr3	1428.57	886.12	769.37	11.11	496.84	7.14	47.90	0.12
19C229_7718DA2_Zr4								
19C232_7718DA2_Zr5	999.90	687.60	595.13	8.52	393.47	5.67	43.46	0.11
19C233_7418DA1_Zr1	3079.17	2409.85	2209.00	31.60	854.71	12.26	94.89	0.23
19C234_7418DA1_Zr2	3130.49	2255.99	2096.23	29.99	679.81	9.76	13.53	0.17
19C235_7418DA1_Zr3	809.57	646.99	574.95	8.21	306.56	4.45	54.73	0.70
19C236_7418DA1_Zr4	1070.76	815.13	656.49	9.39	675.08	9.68	25.46	0.33
19C237_7418DA1_Zr5	9973.32	6271.75	6145.28	88.31	538.17	7.74	140.25	0.16
19C238_7618DA1_Zr1	329.92	227.66	167.92	2.46	254.22	3.67	13.24	0.01
19C239_7618DA1_Zr2	533.11	389.88	298.94	4.27	386.96	5.55	17.75	0.02
19C240_7618DA1_Zr3	624.96	552.79	422.26	6.03	555.45	7.99	29.04	0.03
19C241_7618DA1_Zr4	702.38	465.92	349.11	4.99	497.06	7.12	24.66	0.02
19C242_7618DA1_Zr5	1691.96	1234.64	892.04	12.85	1457.89	20.89	54.14	0.12
19C231_MS19_FCTjm_Zr25	512.53	424.03	378.30	5.49	194.59	2.81	50.10	0.12
19C243_MS19_FCTjm_Zr6	560.53	408.97	352.73	5.12	239.32	3.44	46.91	0.11
BB1								
BB9								
BB10								

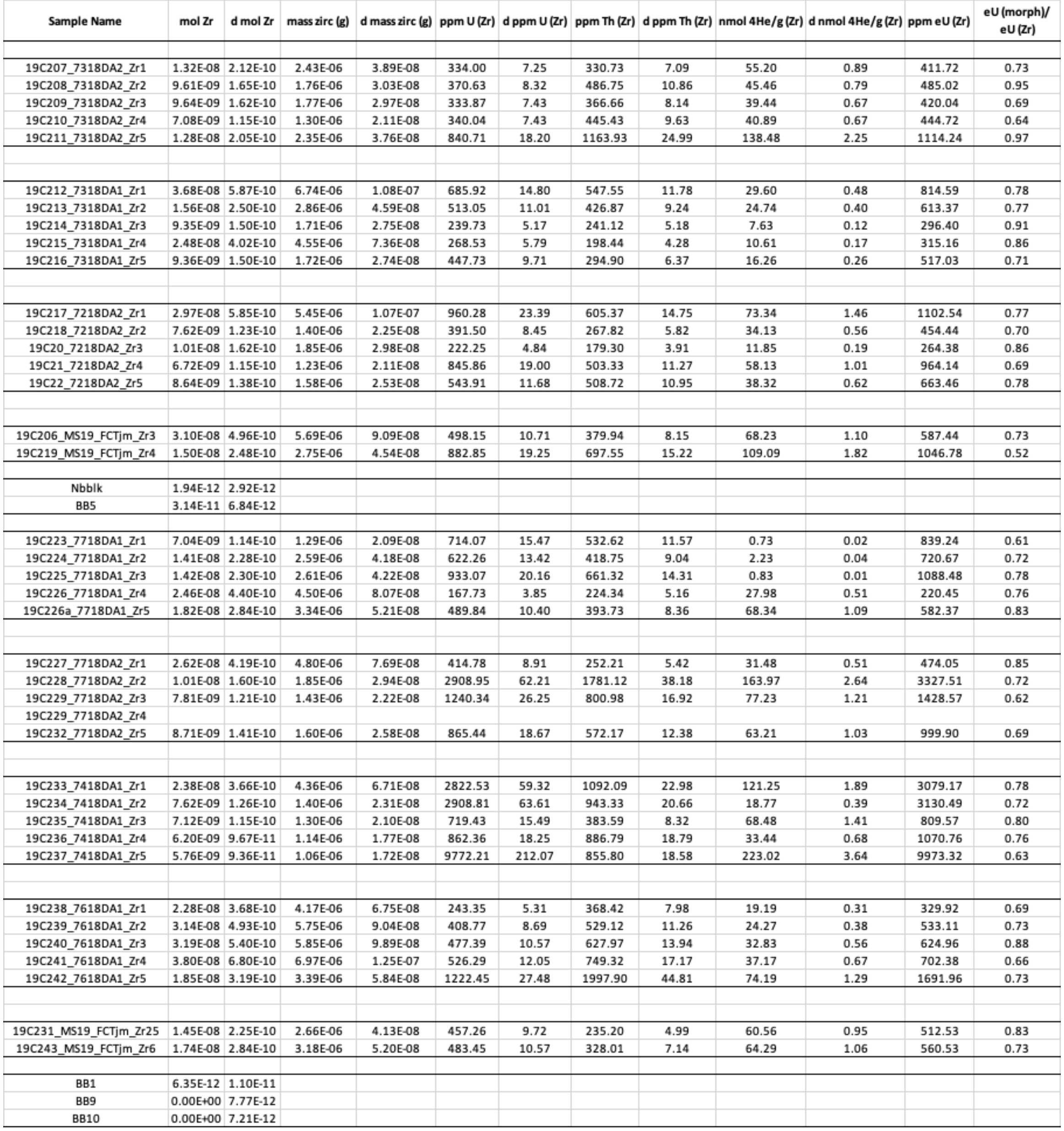

Sample Name	mol Zr	d mol Zr	mass zirc (g)	d mass zirc (g)	ppm U (Zr)	d ppm U (Zr)	ppm Th (Zr)	d ppm Th (Zr)	nmol 4He/g (Zr)	d nmol 4He/g (Zr)	ppm eU (Zr)	eU (morph)/ eU (Zr)
19C207_7318DA2_Zr1	1.32E-08	2.12E-10	2.43E-06	3.89E-08	334.00	7.25	330.73	7.09	55.20	0.89	411.72	0.73
19C208_7318DA2_Zr2	9.61E-09	1.65E-10	1.76E-06	3.03E-08	370.63	8.32	486.75	10.86	45.46	0.79	485.02	0.95
19C209_7318DA2_Zr3	9.64E-09	1.62E-10	1.77E-06	2.97E-08	333.87	7.43	366.66	8.14	39.44	0.67	420.04	0.69
19C210_7318DA2_Zr4	7.08E-09	1.15E-10	1.30E-06	2.11E-08	340.04	7.43	445.43	9.63	40.89	0.67	444.72	0.64
19C211_7318DA2_Zr5	1.28E-08	2.05E-10	2.35E-06	3.76E-08	840.71	18.20	1163.93	24.99	138.48	2.25	1114.24	0.97
19C212_7318DA1_Zr1	3.68E-08	5.87E-10	6.74E-06	1.08E-07	685.92	14.80	547.55	11.78	29.60	0.48	814.59	0.78
19C213_7318DA1_Zr2	1.56E-08	2.50E-10	2.86E-06	4.59E-08	513.05	11.01	426.87	9.24	24.74	0.40	613.37	0.77
19C214_7318DA1_Zr3	9.35E-09	1.50E-10	1.71E-06	2.75E-08	239.73	5.17	241.12	5.18	7.63	0.12	296.40	0.91
19C215_7318DA1_Zr4	2.48E-08	4.02E-10	4.55E-06	7.36E-08	268.53	5.79	198.44	4.28	10.61	0.17	315.16	0.86
19C216_7318DA1_Zr5	9.36E-09	1.50E-10	1.72E-06	2.74E-08	447.73	9.71	294.90	6.37	16.26	0.26	517.03	0.71
19C217_7218DA2_Zr1	2.97E-08	5.85E-10	5.45E-06	1.07E-07	960.28	23.39	605.37	14.75	73.34	1.46	1102.54	0.77
19C218_7218DA2_Zr2	7.62E-09	1.23E-10	1.40E-06	2.25E-08	391.50	8.45	267.82	5.82	34.13	0.56	454.44	0.70
19C20_7218DA2_Zr3	1.01E-08	1.62E-10	1.85E-06	2.98E-08	222.25	4.84	179.30	3.91	11.85	0.19	264.38	0.86
19C21_7218DA2_Zr4	6.72E-09	1.15E-10	1.23E-06	2.11E-08	845.86	19.00	503.33	11.27	58.13	1.01	964.14	0.69
19C22_7218DA2_Zr5	8.64E-09	1.38E-10	1.58E-06	2.53E-08	543.91	11.68	508.72	10.95	38.32	0.62	663.46	0.78
19C206_MS19_FCTjm_Zr3	3.10E-08	4.96E-10	5.69E-06	9.09E-08	498.15	10.71	379.94	8.15	68.23	1.10	587.44	0.73
19C219_MS19_FCTjm_Zr4	1.50E-08	2.48E-10	2.75E-06	4.54E-08	882.85	19.25	697.55	15.22	109.09	1.82	1046.78	0.52
Nbblk	1.94E-12	2.92E-12										
BB5	3.14E-11	6.84E-12										
19C223_7718DA1_Zr1	7.04E-09	1.14E-10	1.29E-06	2.09E-08	714.07	15.47	532.62	11.57	0.73	0.02	839.24	0.61
19C224_7718DA1_Zr2	1.41E-08	2.28E-10	2.59E-06	4.18E-08	622.26	13.42	418.75	9.04	2.23	0.04	720.67	0.72
19C225_7718DA1_Zr3	1.42E-08	2.30E-10	2.61E-06	4.22E-08	933.07	20.16	661.32	14.31	0.83	0.01	1088.48	0.78
19C226_7718DA1_Zr4	2.46E-08	4.40E-10	4.50E-06	8.07E-08	167.73	3.85	224.34	5.16	27.98	0.51	220.45	0.76
19C226a_7718DA1_Zr5	1.82E-08	2.84E-10	3.34E-06	5.21E-08	489.84	10.40	393.73	8.36	68.34	1.09	582.37	0.83
19C227_7718DA2_Zr1	2.62E-08	4.19E-10	4.80E-06	7.69E-08	414.78	8.91	252.21	5.42	31.48	0.51	474.05	0.85
19C228_7718DA2_Zr2	1.01E-08	1.60E-10	1.85E-06	2.94E-08	2908.95	62.21	1781.12	38.18	163.97	2.64	3327.51	0.72
19C229_7718DA2_Zr3	7.81E-09	1.21E-10	1.43E-06	2.22E-08	1240.34	26.25	800.98	16.92	77.23	1.21	1428.57	0.62
19C229_7718DA2_Zr4												
19C232_7718DA2_Zr5	8.71E-09	1.41E-10	1.60E-06	2.58E-08	865.44	18.67	572.17	12.38	63.21	1.03	999.90	0.69
19C233_7418DA1_Zr1	2.38E-08	3.66E-10	4.36E-06	6.71E-08	2822.53	59.32	1092.09	22.98	121.25	1.89	3079.17	0.78
19C234_7418DA1_Zr2	7.62E-09	1.26E-10	1.40E-06	2.31E-08	2908.81	63.61	943.33	20.66	18.77	0.39	3130.49	0.72
19C235_7418DA1_Zr3	7.12E-09	1.15E-10	1.30E-06	2.10E-08	719.43	15.49	383.59	8.32	68.48	1.41	809.57	0.80
19C236_7418DA1_Zr4	6.20E-09	9.67E-11	1.14E-06	1.77E-08	862.36	18.25	886.79	18.79	33.44	0.68	1070.76	0.76
19C237_7418DA1_Zr5	5.76E-09	9.36E-11	1.06E-06	1.72E-08	9772.21	212.07	855.80	18.58	223.02	3.64	9973.32	0.63
19C238_7618DA1_Zr1	2.28E-08	3.68E-10	4.17E-06	6.75E-08	243.35	5.31	368.42	7.98	19.19	0.31	329.92	0.69
19C239_7618DA1_Zr2	3.14E-08	4.93E-10	5.75E-06	9.04E-08	408.77	8.69	529.12	11.26	24.27	0.38	533.11	0.73
19C240_7618DA1_Zr3	3.19E-08	5.40E-10	5.85E-06	9.89E-08	477.39	10.57	627.97	13.94	32.83	0.56	624.96	0.88
19C241_7618DA1_Zr4	3.80E-08	6.80E-10	6.97E-06	1.25E-07	526.29	12.05	749.32	17.17	37.17	0.67	702.38	0.66
19C242_7618DA1_Zr5	1.85E-08	3.19E-10	3.39E-06	5.84E-08	1222.45	27.48	1997.90	44.81	74.19	1.29	1691.96	0.73
19C231_MS19_FCTjm_Zr25	1.45E-08	2.25E-10	2.66E-06	4.13E-08	457.26	9.72	235.20	4.99	60.56	0.95	512.53	0.83
19C243_MS19_FCTjm_Zr6	1.74E-08	2.84E-10	3.18E-06	5.20E-08	483.45	10.57	328.01	7.14	64.29	1.06	560.53	0.73
BB1	6.35E-12	1.10E-11										
BB9	0.00E+00	7.77E-12										
BB10	0.00E+00	7.21E-12										

APPENDIX E

HEFTY THERMAL MODELLING INPUT PARAMETERS

Analysis/Sample Name	**19C208_7318DA2_Zr2**	**19C215_7318DA1_Zr4**	**19C217_7218DA2_Zr1**	**19C226_7718DA1_Zr4**	**19C227_7718DA2_Zr1**	**19C235_7418DA1_Zr3**	**19C241_7618DA1_Zr4**
Raw date (uncorrected)	17.33874237	6.239547716	12.32431483	23.47149369	12.30341448	15.67050139	9.7951109
1s ± Error (Ma)	0.197190414	0.076207656	0.153316183	0.270871283	0.153086235	0.277697159	0.107266364
Grain Radius (um)	38.91	52.18	59.08	53.82	50.69	38.14	65.32
ppm U	351.06	231.01	740.12	126.94	354.58	574.95	349.11
ppm Th	461.04	170.71	466.58	169.78	215.60	306.56	497.06
Calibrations	Guenthner et al., 2013 (Zircon)	Guenthner et al., 2013 (Zircon)	Guenthner et al., 2013 (Zircon)	Guenthner et al., 2013 (Zircon)	Guenthner et al., 2013 (Zircon)	Guenthner et al., 2013 (Zircon)	Guenthner et al., 2013 (Zircon)
Abraded (um)	0	0	0	0	0	0	0
Mineral	Zircon	Zircon	Zircon	Zircon	Zircon	Zircon	Zircon
Stopping Distances	Ketcham et al. 2011	Ketcham et al. 2011	Ketcham et al. 2011	Ketcham et al. 2011	Ketcham et al. 2011	Ketcham et al. 2011	Ketcham et al. 2011
Alpha Calculation	Ejection	Ejection	Ejection	Ejection	Ejection	Ejection	Ejection
Age to Report	Corrected	Corrected	Corrected	Corrected	Corrected	Corrected	Corrected
Age Alpha Correction	Ketcham et al. 2011	Ketcham et al. 2011	Ketcham et al. 2011	Ketcham et al. 2011	Ketcham et al. 2011	Ketcham et al. 2011	Ketcham et al. 2011
Search Method	Monte Carlo	Monte Carlo	Monte Carlo	Monte Carlo	Monte Carlo	Monte Carlo	Monte Carlo
Subsegmentt spacing	Random	Random	Random	Random	Random	Random	Random
Ending Condition	Paths Tied	Paths Tied	Paths Tied	Paths Tied	Paths Tied	Paths Tied	Paths Tied
Number of Runs	10000	10000	10000	10000	10000	10000	10000